Draft version June 21, 2014
Preprint typeset using LaTeX style emulateapj v. 03/07/07

OPTICAL-FAINT, FAR-INFRARED-BRIGHT *HERSCHEL* SOURCES IN THE CANDELS FIELDS: ULTRA-LUMINOUS INFRARED GALAXIES AT $Z > 1$ AND THE EFFECT OF SOURCE BLENDING

Haojing Yan [1], Mauro Stefanon [1], Zhiyuan Ma [1], S. P. Willner [2], Rachel Somerville [3], Matthew L. N. Ashby [2], Romeel Davé [4], Pablo G. Pérez-González [5], Antonio Cava [6], Tommy Wiklind [7], Dale Kocevski [8], Marc Rafelski [9], Jeyhan Kartaltepe [10,12], Asantha Cooray [11]

Draft version June 21, 2014

ABSTRACT

The *Herschel* very wide-field surveys have charted hundreds of square degrees in multiple far-IR (FIR) bands. While the Sloan Digital Sky Survey (SDSS) is currently the best resource for optical counterpart identifications over such wide areas, it does not detect a large number of *Herschel* FIR sources and leaves their nature undetermined. As a test case, we studied seven "SDSS-invisible", very bright 250 μm sources ($S_{250} > 55$ mJy) in the Cosmic Assembly Near-infrared Deep Extragalactic Legacy Survey (CANDELS) fields where we have a rich multi-wavelength data set. We took a new approach to decompose the FIR sources, using the near-IR or the optical images directly for position priors. This is an improvement over the previous decomposition efforts where the priors are from mid-IR data that still suffer from the source blending problem in the first place. We found that in most cases the single *Herschel* sources are made of multiple components that are not necessarily at the same redshifts. Our decomposition succeeded in identifying and extracting their major contributors. We show that these are all ULIRGs at $z \sim 1$–2 whose high L_{IR} is mainly due to dust-obscured star formation. Most of them would not be selected as sub-mm galaxies. They all have complicated morphologies indicative of merger or violent instability, and their stellar populations are heterogeneous in terms of stellar masses, ages and formation histories. Their current ULIRG phases are of various degrees of importance in their stellar mass assembly. Our practice provides a promising starting point to develop an automatic routine to reliably study bright *Herschel* sources.

Subject headings: infrared: galaxies — submillimeter: galaxies — galaxies: starburst — methods: data analysis

1. INTRODUCTION

In its more than four years of operation, the *Herschel* Space Observatory (Pilbratt et al. 2010), the largest FIR/sub-mm space telescope ever flown, produced a wealth of data awaiting exploration. It carried two imaging spectrometers, namely, the Photodetector Array Camera and Spectrometer (PACS, Poglitsch et al. 2010) observing in 100 (or 70) and 160 μm, and the Spectral and Photometric Imaging REceiver (SPIRE, Griffin et al. 2010) observing in 250, 350 and 500 μm. Together they sampled the peak of heated dust emission from $z = 0$ to 6 and possibly beyond, and offered the best capability to date in the *direct* measurement of the total infrared (IR) luminosities for a large number of galaxies at $z > 1$. Two of the largest *Herschel* extragalactic surveys, the Herschel Astrophysical Terahertz Large Area Survey (H-ATLAS; Eales et al. 2010) and the Herschel Multi-tiered Extragalactic Survey (HerMES; Oliver et al. 2012), have mapped the FIR/sub-mm universe in unprecedented detail. H-ATLAS has surveyed ~ 570 deg^2 over six areas at a uniform depth, while HerMES has observed a total of ~ 380 deg^2 in several levels of depth and spatial coverage combinations ("L1" to "L7", from the deep-and-narrow to wide-and-shallow).

The true power of these *Herschel* data can only be achieved when they are combined with observations at other wavelengths, most importantly in optical to near-IR (NIR) as this is the traditional regime where the stellar population of galaxies is best studied. The Sloan Digital Sky Survey (SDSS; York et al. 2000) is the most natural choice when identifying optical counterparts of the FIR sources over such large areas. However, its limited depth does not allow us to take the full advantage of these already sensitive FIR data. For example, Smith et al. (2011) cross-matched the 6,876 sources in the ~ 16 deg^2 H-ATLAS Science Demonstration Phase field to the SDSS, and only 2,422 (35.2%) of them have reliable counterparts. While some of identification failures are caused by the ambiguity in assigning the counterpart due to the large *Herschel* beam sizes, most of these FIR sources that are not matched in the SDSS are genuinely faint in the optical. This probably should not be

[1] Department of Physics & Astronomy, University of Missouri, Columbia, MO 65211, USA
[2] Harvard-Smithsonian Center for Astrophysics, 60 Garden Street, Cambridge, MA 02138, USA
[3] Department of Physics and Astronomy, Rutgers University, 136 Frelinghuysen Rd., Piscataway, NJ 08854, USA
[4] University of the Western Cape, 7535 Bellville, Cape Town, South Africa
[5] Departamento de Astrofísica, Facultad de CC. Físicas, Universidad Complutense de Madrid, E-28040 Madrid, Spain
[6] Observatoire de Genève, Université de Genève, 51 Ch. des Maillettes, 1290 Versoix, Switzerland
[7] Joint ALMA Observatory, Alonso de Cordova 3107, Vitacura, Santiago, Chile
[8] Department of Physics and Astronomy, University of Kentucky, Lexington, KY 40506, USA
[9] Infrared Processing and Analysis Center, California Institute of Technology, Pasadena, CA 91125, USA
[10] National Optical Astronomy Observatory, 950 North Cherry Avenue, Tucson, AZ 85719, USA
[11] Department of Physics and Astronomy, University of California, Irvine, California 92697, USA
[12] Hubble Fellow.

surprising because FIR sources could be very dusty. Nevertheless, it is still interesting that some of the brightest *Herschel* sources, whose flux densities are a few tens of mJy, are not visible in the SDSS images at all. The nominal 5 σ limits of the SDSS is 22.3, 23.3, 23.1, 22.3, 20.8 mag in u, g, r, i, and z, respectively (York et al. 2000). Using a 2 σ limit, a conservative estimate of the FIR-to-optical flux density ratio of such SDSS-invisible FIR sources is $S_{FIR}/S_{opt} \gtrsim 10^4$.

Naturally, one would speculate that these optical-faint *Herschel* sources are Ultra-Luminous InfraRed Galaxies (ULIRGs; see e.g. Lonsdale, Farrah & Smith 2006 for a review) at high redshifts. If they are at $z \gtrsim 1$, their absence from the SDSS images can be easily explained by their large luminosity distances. If they are ULIRGs, their FIR brightness could also be understood. In this sense, the closest analogs to such objects are sub-mm galaxies (SMGs), which are usually selected at ~ 850 μm and are found to be ULIRGs at $z \sim 2$–3. On average, a typical SMG would have 850 μm flux density $S_{850} \sim 5.7$ mJy and optical brightness $R \sim 24.6$ mag (see e.g. Chapman et al. 2005). The SMGs at the faint-end of the optical brightness distribution are likely at $z \sim 4$–5 or even higher redshifts (Wang et al. 2007; Capak et al. 2008; Schinnerer et al. 2008; Coppin et al. 2009; Daddi et al. 2009; Younger et al. 2009). The most extreme example is the historical HDF850.1 (Hughes et al. 1998), which has no detectable counterpart in even the deepest optical/NIR images (Cowie et al. 2009 and the references therein) and now has been confirmed to be at $z = 5.183$ based on its CO lines (Walter et al. 2012). It has also been suggested that extremely dusty galaxies like HDF850.1 could play a major role in the star formation history in the early universe (Cowie et al. 2009). If this is true, the very wide field *Herschel* surveys should be able to reveal a large number of such objects at very high redshifts. In fact, recently a bright FIR galaxy discovered in the HerMES, which again has no detectable optical counterpart ($z > 25.9$ mag) and is only weakly visible in NIR, set a new, record-high redshift of $z = 6.337$ for ULIRG (Riechers et al. 2013), approaching the end of the cosmic H I reionization epoch.

It is thus important to investigate in detail the nature of such SDSS-invisible, bright *Herschel* sources. Obviously, the minimum requirement to move forward is to acquire optical data that are much deeper than the SDSS. In this paper, we present our study of seven such sources that happen to be covered by the Cosmic Assembly Near-infrared Deep Extragalactic Legacy Survey (CANDELS; PIs: Faber & Ferguson; Grogin et al. 2011; Koekemoer et al. 2011) and therefore have a rich multi-wavelength data set. Our main scientific goal is to understand whether these sources are indeed high-z ULIRGs and the stellar populations of their host galaxies. By targeting some of the brightest *Herschel* sources, our study will also help address one of the most severe problems at the FIR bright-end, namely, the discrepancy between the observed bright FIR source number counts and various model predictions (see e.g., Clements et al. 2010, and the references therein; Niemi et al. 2012). While the vast majority of other *Herschel* sources do not have comparable ancillary data as used in this current work, our study here will serve as an useful guide to future investigations.

The most severe technical obstacle that we need to overcome is the long-standing source confusion (i.e., blending) problem in the FIR/sub-mm regime. The beam sizes (measured as Full Width at Half Maximum; FWHM) of PACS are ~ 6–$7''$ and $\sim$ 11-14$''$ at 70/100 μm and 160 μm, respectively, depending on the scanning speeds. Similarly, the beam sizes of SPIRE are $\sim 18''$, $25''$ and $36''$ at 250, 350 and 500 μm, respectively. Therefore, source confusion can still be severe in the *Herschel* data, which causes ambiguity in assigning the correct counterparts. It also raises the possibility that the very high FIR flux densities of the seemingly single *Herschel* sources might be caused by the blending of multiple objects, each being less luminous, within a single beam. SMGs are known to suffer from exactly the same problem because of the coarse angular resolutions of the sub-mm imagers used for their discovery at single-dishes. In fact, using the accurate positions determined by the sub-mm interferometry at the Submillimeter Array (SMA; Ho et al. 2004), it has been unambiguously shown that some of the brightest SMGs indeed are made of multiple objects that may or may not be physically related (Wang et al. 2011; Barger et al. 2012). Recently, a large, high-resolution 870 μm interferometry survey of 126 SMGs with the Atacama Large Millimeter/submillimeter Array (ALMA) has shown that $> 35\%$ of the SMGs originated from single-dish observations could consist of multiple objects (Hodge et al. 2013; Karim et al. 2013).

Even with the unprecedented sensitivity of the ALMA, however, it is still impractical to pin down the locations of the large number of *Herschel* sources and to resolve their multiplicities through sub-mm interferometry. We therefore employed an alternative, less expensive, empirical approach in this work, using deep optical/NIR data to decompose a given *Herschel* source and to identify its *major* counterpart(s) in the process. This is different from the statistical "likelihood ratio" method (LR; Sutherland & Saunders 1992), which would assign a counterpart based on the probabilities of all candidates but would not apportion the flux in case of multiplicity. It is also different from the de-blending approach where mid-IR data of better resolution (albeit still being coarse) would be used as the position priors (e.g., Roseboom et al. 2010; Elbaz et al. 2010; Magnelli et al. 2013). We do not take this latter approach because it could be that a prior mid-IR source is already a blend of multiple objects that are not necessarily associated. In this paper, we show that in most cases our method can successfully extract the *major* contributors to the FIR sources, which is sufficient if we are mainly interested in the ULIRG population with the current *Herschel* very-wide-field data. While it is still in its rudimentary stage, this method has the potential of being fully automated, and could be critical in the *Herschel* fields where the "ladders" in the mid-IR are not available and can no longer be obtained due to the lack of instruments.

The paper is organized as follows. The sample and the relevant data are presented in §2, followed by an outline of our analyzing methods in §3. Due to the different data sets involved in different CANDELS fields, we present the analysis of individual objects in §4, 5 and 6, respectively. We present a discussion of our results in §7, and summarize in §8. We assume the following cosmological parameters throughout: $\Omega_M = 0.27$, $\Omega_\Lambda = 0.73$ and

$H_0 = 71$ km s^{-1} Mpc^{-1}. The quoted magnitudes are all in the AB system.

2. SAMPLE DESCRIPTION

The SDSS-invisible, bright *Herschel* sources in this work were selected based on the first data release (DR1) of the HerMES team, which only includes the SPIRE data. We used their band-merged "xID" catalogs, which were constructed by fitting the point spread function (PSF) at the source locations determined in the 250 μm images (Wang et al., in prep.). These catalogs are cut at a bright flux density level of 55 mJy for 250 and 350 μm, and 30 mJy for 500 μm.

Among these released HerMES fields, six of them have SDSS coverage, three of which have overlap with the CANDELS fields. These three fields are the "L2_GOODS-N" ($\sim$ 0.59 deg^2, 53 sources in the HerMES DR1 catalog), "L3_Groth-Strip" ($\sim$ 1.15 deg^2, 74 sources), and "L6_XMM-LSS-SWIRE" fields ($\sim$ 22.58 deg^2, 2,320 sources), which cover the CANDELS "GOODS-N", "EGS" and "UDS" fields, respectively [13]. The CANDELS *HST* data, taken by the Advanced Camera for Surveys (ACS) and/or the IR channel of the Wide Field Camera 3 (WFC3), include 5 (in GOODS-N), 13 (in EGS) and 4 (in UDS) of these sources. We examined them in the SDSS DR9 images and selected those that do not have any optical detections in any of the five bands within 6″ (approximately $\sim 3\times$ of the positional accuracy) to the reported 250 μm source centroids. This resulted in 2, 3 and 2 sources in GOODS-N, EGS and UDS, respectively, which form the sample studied by this work. Table 1 lists the photometry of these seven sources from the HerMES public catalogs, and Figure 1 shows their images in the SPIRE 250 μm and the SDSS i' bands. In addition to the HerMES three-band SPIRE data, the sources in L2_GOODS-N and L3_Groth-Strip also have the PACS 100 and 160 μm data from the DR1 of the PACS Evolutionary Probe program (PEP; Lutz et al. 2011).

The three CANDELS fields have a wide range of ancillary data, and those used in the spectral energy distribution (SED) analysis and/or morphological study are listed below:

— GOODS-N: *HST* ACS F435W (hereafter B_{435}), F606W (V_{606}), F775W (i_{775}) and F850LP (z_{850}) from the GOODS program; F098M (Y_{098}), F105W (J_{105} and F160W (H_{160}) from the CANDELS program; *Spitzer* InfraRed Array Camera (IRAC) 3.6, 4.5, 5.8, and 8.0 μm, and Multiband Imaging Photometer for Spitzer (MIPS) 24 μm from the GOODS program; MIPS 70 μm from the Far-Infrared Deep Extragalactic Legacy survey (FIDEL; Dickinson et al., in prep.); ground-based deep U-band image taken by the GOODS team at the KPNO 4m MOSAIC (Dickinson, priv. comm.).

— UDS: ACS V_{606} and F814W (I_{814}), WFC3 IR J_{105} and H_{160} from the CANDELS program; IRAC 3.6 and 4.5 μm from the *Spitzer* Extended Deep Survey (SEDS, PI. Fazio; Ashby et al. 2013); MIPS 24 μm from the *Spitzer* UDS program (SpUDS, PI. Dunlop); ground-based u^*, g', r', i', and z' data from the final data release ("T0007") of the CFHT Legacy Survey Wide component (CFHTLS-Wide); the ground-based J, H, and K_s data from the Ultra Deep Survey (UDS) component of the UKIRT Deep Sky Survey (UKIDSS).

— EGS: ACS V_{606} and I_{814} from the All-wavelength Extended Groth strip International Survey (AEGIS; Davis et al. 2007); WFC3 IR J_{105} and H_{160} from the CANDELS program; ground-based u^*, g', r', i', and z' data from the final release of the CFHTLS Deep component (CFHTLS-Deep); MIPS 24 and 70 μm from the FIDEL program; IRAC 3.6 and 4.5 μm that incorporate the data from both the SEDS program and the *Spitzer* Guaranteed Time Observing program 8 (Barmby et al. 2008).

In addition, public X-ray and high-resolution radio images and/or catalogs are also available in these fields, which improve the interpretation of our sources. The GOODS-N has the *Chandra* 2 Ms data (Alexander et al. 2003) and the VLA 1.4 GHz data (Morrison et al. 2010), the UDS field has the X-ray source catalog based on the XMM-Newton observations (Ueda et al. 2008) and the VLA 1.4 GHz source catalog (Simpson et al. 2006), and the EGS field has the Chandra 800 ks data from the AEGIS program (Nandra et al. in prep.; Laird et al. 2009) and the VLA 1.4 GHz data (Ivison et al. 2007; Willner et al. 2012).

3. OVERVIEW OF METHODS FOR ANALYSIS

As the deep optical-to-NIR data reveal, there are always multiple candidate counterparts for any 250 μm source in our sample. Our basic goal is to decompose the blended objects, to determine the major contributors to the FIR emissions, and to reveal their nature by analyzing their optical-to-far-IR SEDs. Here we briefly describe our methods.

3.1. *Source Decomposition and Flux Calibration*

We used the GALFIT package developed by Peng et al. (2002) to do the decomposition. While its wide usage by the community is mostly to study galaxy morphologies, GALFIT has a straightforward capability of fitting the PSF at multiple, fixed locations. This well suits our cases, because all the potential components are effectively point sources at the angular resolutions of the *Herschel* instruments. Although other PSF fitting softwares tailored for crowded field photometry (such as ALLSTAR of DAOPHOT, Steston 1987), could also be used in the decomposition of *Herschel* data (e.g., Rawle et al. 2012), we chose GALFIT because it produced the best results in our tests. When the source S/N is sufficient, GALFIT is capable of differentiating the offset of the input source position as small as $\sim 1/10$ of a native pixel (Peng, priv.comm.). This corresponds to $\sim 2''$ in the 250 μm band, and is comparable to the astrometric accuracy (i.e., the accuracy of their centroids) of our bright 250 μm sources.

As we are interested in constructing the FIR SEDs, we decomposed not only the 250 μm but also the PACS 160 and 100 μm images when they are available. We also extended the same decomposition to the MIPS 70 and 24 μm data, because the point-source assumption still largely holds at the MIPS resolution. On the other

[13] "GOODS-N" stands for the northern field of the Great Observatories Origins Deep Survey (Giavalisco et al. 2003), "EGS" stands for the extended Groth Strip, and "UDS"stands for the Ultra-Deep Survey component of the United Kingdom Infrared Telescope (UKIRT) Infrared Deep Sky Survey (UKIDSS).

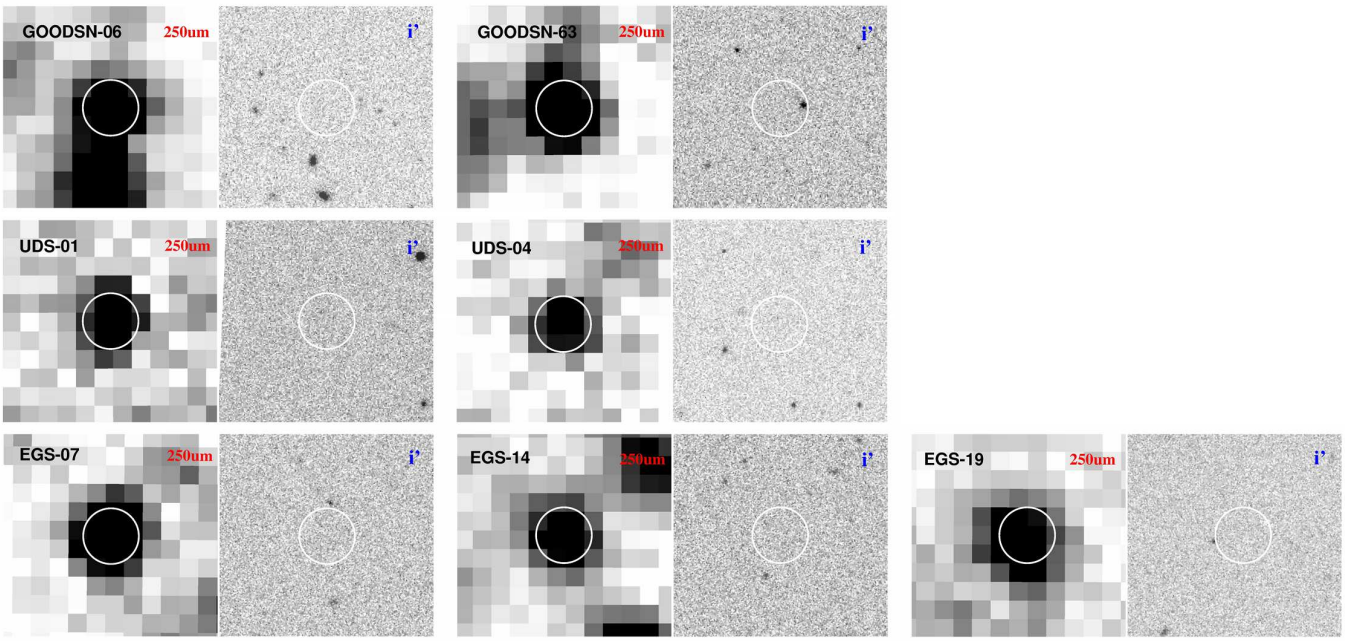

FIG. 1.— Image cutouts of the seven SDSS-undetected, bright *Herschel* sources in our sample. Two of them are in the GOODS-N field (top), two are in the UDS field (middle), and three are in the EGS field (bottom). For each source, the 250 μm image is shown in left and the SDSS i' image is shown in right. All images are $1\farcm2 \times 1\farcm2$ in size. North is up and east is to left. The white circles, which are $9''$ in radius and resemble the 250 μm beam size, center on the 250 μm source centroids as reported by the HerMES DR1 catalogs.

hand, we did not attempt to decompose the SPIRE 350 and 500 μm data, because the beam sizes of these two bands are so large that it is difficult to achieve reliable results using our current approach. We generated the 250 μm PSF by using a symmetric 2D Gaussian of $18.15''$ FWHM, which has already been proved to be a good fit to the point sources in the HerMES images (see e.g. Roseboom et al. 2010, Smith et al. 2011). For the PACS images, we adopted the *green* (for 100μm) and *red* (for 160μm) PSFs provided by the PEP team along with their DR1, which were built by stacking a set of bright, isolated and point-like sources. The MIPS 70 and 24 μm PSFs were created using the `daophot.psf` task in `IRAF`. For each field and band, a PSF was constructed from a set of 7 to 15 bright and isolated sources, which are all point sources as judged from the WFC3 H_{160} image.

For a given 250 μm source, we identified its potential components by searching for objects in the high-resolution near-IR or optical images within $r = 18''$ of the 250 μm centroid. In other words, the diameter of the searching area is twice the FWHM of the 250 μm beam. The positions of the potential optical/near-IR components were then used as the priors for GALFIT to extract the fluxes at these locations in various bands. This is different from using the 24 μm source positions as the priors, and we did not take the latter approach because, as mentioned in §1, it is not uncommon that a single 24 μm source is actually a blended product of multiple objects that are not necessarily related. In addition, using optical/near-IR position priors has the advantage of being able to directly tie the FIR source to the ultimate counterpart(s). Our first choice of the detection image was the WFC3 H_{160} image, and the second choice was the ACS I_{814} image if H_{160} is not available. The third choice was the ground-based i-band image if it is more appropriate than the *HST* images (for instance to avoid splitting one galaxy of complex morphology into several sub-components at the *HST* resolution). Regardless of the exact choice, the search always resulted in several tens of objects. Currently, it is not desirable for our routine to deal with such a large number of objects because there are still a large number of intermediate steps that require human intervention (see below). As only a fraction of these objects actually contribute to the FIR emission, in this current work we chose to use the PACS 160 and 100 μm and the MIPS 24 μm images to narrow down the input list for GALFIT. The general guideline was that only the objects that could have non-negligible 24 μm emissions should be further considered. While we could have developed some quantitative criteria for this process, we opted to simply rely on visual inspection because this was only an interim step that we are planning to replace in the near future. For this work, we were conservative in eliminating objects from the input list, and included those that are at the outskirts of the 24 μm source footprints.

The above procedure narrowed the input lists to $\lesssim 10$ objects each. Similar to the philosophy of PSF fitting in crowded stellar fields (e.g., Stetson 1987), one should seek to fit *simultaneously the exact objects* that are contributing flux, because this is when the most accurate result can be obtained. The implementation was rather difficult, however. In our case, fitting all the objects from the input list simultaneously was often not satisfactory. The symptoms were bad residual image after subtracting off the fitted objects, large errors associated with the decomposed fluxes, or in some cases, the crashing of the decomposition process. Therefore, we took two complementary approaches.

In the first approach, which we dub as the "automatically iterative" approach, all the potential components were still fitted simultaneously, however those with their derived fluxes smaller than the associated flux errors were deemed negligible and removed from the input list for the

next round. The simultaneous fit was repeated using the cleaned input list until no negligible objects were left. This procedure usually converged after 2–3 iterations. Among the surviving components, some could have fitted fluxes an order of magnitude smaller than the others. When this happened, a new fit was performed using an input list that contained only the major components. If the residual image was of the same quality (judged by χ^2 and also visual inspection) as from the previous round, these major components were deemed as the only contributors and those less important ones were ignored. Otherwise we kept the results from the previous round. Finally, a "sanity check" was carried out on the surviving objects by fitting them one at a time. Usually it was obvious that there were residuals left at the locations of the other components, indicating that more than one component contributes significantly to the source and hence the simultaneous fit was necessary. However, in some cases the fit to only one object produced a clean residual image of the same quality as the one from the simultaneous fit to multiple objects, and when this happened we flagged this source as being a degenerate case and would offer alternative interpretations.

The other approach was highly interactive, which we call the "trial-and-error" approach. This method had to be used when the automatically iterative method failed at the first step: it either crashed or resulted in unreasonable survivors with very large errors that could not be improved by removing any of the survivors (i.e., the iteration failed). In this case, we started from our best guess of the most likely counterpart, and fit for only this object in the first round. We then checked the residual map to see if there were any residuals left at the positions of any other objects in the original input list. If yes, these objects were added to the fitting list, one at a time, and the fit iterated until reaching the best result possible. The iteration stopped when adding more objects either produced only negligible contributors or started to produce unreasonable results.

We note that these two approaches can be integrated and further improved in their implementation. In particular, it is possible to not only automate the trial-and-error approach but also use it to narrow down the input list without the reference to additional data such as the MIPS 24 μm image. While it is beyond the scope of this paper to fully develop this automatic routine, we demonstrate its feasibility in APPENDIX. We also note that we did not use the radio source positions as the priors. This is because some objects that have non-negligible contributions to the FIR emissions could fall below the sensitivity of the currently available radio data.

The PSF-fitting fluxes obtained in the procedures above should be corrected for the finite PSF sizes, which could be achieved by comparing our PSF-fitting results to the curve-of-growth aperture photometry on a set of isolated point sources. In addition, the PACS images also suffer from light lost caused by the application of the high-pass filtering in the reduction process, which is not compensated in the currently released images and thus should also be corrected. To simply the process, we did the following for this work. For the PACS data, we derived the total correction factors for 100 and 160 μm bands in each field by comparing our PSF-fitting results against those in the PEP DR1 single-band catalogs. For the SPIRE data, we adopted the photometry reported in the HerMES DR1 catalog as the total flux densities and proportionated among the multiple contributors according to our decomposition results.

To obtain realistic uncertainties in the *Herschel* bands, we carried out extensive simulations. For each source, we simulated it by adding the PSFs according to the final decomposition result, put the simulated object in several hundreds of random locations on the real image, ran the decomposition at these locations, and obtained a distribution of the recovered fluxes. The dispersion of this distribution was adopted as the instrumental errors. The errors due to the confusion noise were then added in quadrature to the instrumental errors to obtain the final errors. For PACS 100 and 160 μm, we adopted the confusion noise values of 0.15 and 0.68 mJy/beam from Magnelli et al. (2013), and for the SPIRE data we inherited the values from the HerMES DR1 catalogs, which are 5.8, 6.3 and 6.8 mJy/beam based on Nguyen et al. (2010). For our objects, the confusion noise only contributes insignificantly to the total error in the PACS bands, however it dominates the total error in the SPIRE bands. For the sake of consistency, the errors in the MIPS 24 and 70 μm were obtained in the same way but without the confusion term.

As mentioned above, we did not apply the decomposition to the 350 and the 500 μm data where the resolutions are much worse and the source S/N is generally much lower than at the 250 μm. This means that generally these two bands cannot be incorporated in our analysis. However, in few cases we find that the vast majority of the 250 μm flux is from only one object (others contribute a few per cent at most), or that the major contributors are likely at the same redshift and thus we can discuss their combined properties. For such sources, we directly use the 350 and the 500 μm measurements from the HerMES DR1 catalogs in our study.

3.2. *SED Fitting*

In order to understand the objects under question, their redshifts are needed. While some have spectroscopic redshifts, most of our objects have to rely on photometric redshift (z_{ph}) estimates. To derive z_{ph}, we used the SEDs that extend from optical to the IRAC wavelengths (to 8.0 μm when possible). The inclusion of the IRAC data was important but often non-trivial. As many of our sources have input objects that are close to each other, they are usually blended in the IRAC images and thus need to be decomposed as well. For most objects, the point-source assumption does not hold anymore in IRAC. Therefore, we used the TFIT technique (Laidler et al. 2006) for this purpose, where the image templates were constructed from the H_{160} images, and then were convolved by the IRAC PSFs to fit the IRAC images.

We used the Hyperz software (Bolzonella et al. 2000) and the stellar population synthesis (SPS) models of Bruzual & Charlot (2003; hereafter BC03) to estimate z_{ph}. The latest implementation of Hyperz also includes the tool to derive other physical quantities such as the stellar mass (M^*), the age (T) etc. ("hyperz_mass", M. Bolzonella, priv. comm.) from the models. We adopted the BC03 models of solar metallicity and the initial mass function (IMF) of Chabrier (2003), and used a series of exponentially declining star formation histories (SFHs)

with τ ranging from 1 Myr to 20 Gyr. The simple stellar population (SSP) model was also included, which was treated as $\tau = 0$. The models were allowed to be reddened by dust following the Calzetti's law (Calzetti 2001), with A_V ranging from zero to 4 mag.

The above SED fitting procedure does not consider the effect of emission lines. To assess how this might impact the derived physical properties, we also used the LePhare software (Arnouts & Ilbert 2007) to analyze the same SEDs. LePhare can calculate the strengths of the common emission lines based on the star formation rate (SFR) of the underlying SPS models, which we chose to be the same sets of models used in the Hyperz analysis. The results derived by LePhare in most cases are very close to those derived using Hyperz, and thus we only include the discussion of the Hyperz results in this paper.

A key quantity in revealing the nature of our sources is the total IR luminosity, L_{IR}, traditionally calculated over restframe 8 to 1000 μm. To derive L_{IR}, we used our own software tools to fit the mid-to-far-IR SED to the starburst models of Siebenmorgen & Krügel (2007; hereafter SK07) at either the spectroscopic redshift, when available, or the adopted z_{ph} from above. We adopted their "9kpc" and "15kpc" models, which SK07 produces for the starbursts at high redshifts. When possible, we also derive the dust temperature (T_d) and mass (M_d) by using the code of Casey (2012), which fit the FIR SED to a modified blackbody spectrum combined with a power law extending from the mid-IR. As we only have limited passbands, we fixed the slope of the mid-IR power law to $\alpha = 2.0$ and the emissivity of the blackbody spectrum to $\beta = 1.5$ (Chapman et al. 2005; Pope et al. 2006; Casey et al. 2009). This approach usually does not produce a good fit at 24 μm, presumably due to the fixed α. Therefore, we ignored the 24 μm data points when deriving T_d and M_d. The code derives two different dust temperatures, one being the best-fit temperature of the graybody (T_d^{fit}) and the other being the temperature according to Wien's displacement law that corresponds to the peak of the emission as determined by the best-fit graybody (T_d^W). We adopted T_d^{fit}. Finally, we also obtained the gas mass, M_{gas}, by applying the nominal Milky Way gas-to-dust-mass ratio of 140 (e.g. Draine et al. 2007), with the caveat that this ratio could strongly depend on the metallicities (e.g., Draine et al. 2007; Galametz et al. 2011; Leroy et al. 2011).

Another important quantity is the SFR. SED fitting in the optical-to-NIR regime provides the SFR intrinsic to the SFH of the best-fit BC03 model (hereafter SFR_{fit}), which naturally takes into account the effect of dust extinction. However, there could still be star formation processes completely hidden by dust, which would not be counted by SFR_{fit} and could only be estimated through the measurement of L_{IR}. A common practice is to exercise the conversion given by Kennicutt (1998), which is $SFR_{IR} = 1.0 \times 10^{-10} L_{IR}$ after adjusting for a Chabrier IMF (see e.g., Riechers et al. 2013) [14]. This conversion assumes solar metallicity and is valid for a star-bursting galaxy that has a constant SFR over 10–100 Myr and whose dust re-radiates all of the bolometric luminosity. The total SFR would then be some combination of SFR_{fit} and SFR_{IR}. However, this should not be a straightforward sum of the two. The reason is that our measured L_{IR} includes not only the IR emission from the region completely blocked by dust (hereafter L_{IR}^{blk}) but also the contribution from the exposed region where a fraction of its light is extincted by dust and is re-radiated in the FIR (hereafter L_{IR}^{ext}), i.e., $L_{IR} = L_{IR}^{blk} + L_{IR}^{ext}$. In other words, SFR_{IR} derived by applying the Kennicutt's conversion directly to L_{IR} would have already included part of the contribution from SFR_{fit}. To deal with this problem, we calculated L_{IR}^{ext} by integrating the difference between the reddened and the de-reddened spectra from the best-fit BC03 model and assuming that this amount of light is completely re-radiated in the FIR. We then obtained $L_{IR}^{blk} = L_{IR} - L_{IR}^{ext}$, and calculated $SFR_{IR}^{blk} = 1.0 \times 10^{-10} L_{IR}^{blk}$, where SFR_{IR}^{blk} is the "net" SFR in the region completely blocked by dust.

From the derived SFR and M^*, one can calculate the specific SFR as $SSFR = SFR_{tot}/M^*$. The caveat here is that the stellar mass derived by SED fitting as mentioned above is only for the relatively exposed region and does not include the completely obscured region. Nevertheless, we can still use a related but more appropriate quantity in this context, namely the stellar mass doubling time (T_{db}), which is defined as the time interval necessary to further assemble the same amount of stellar mass of the exposed region should the galaxy keeps its SFR constant into the future. Specifically, we can obtain $T_{db}^{tot} = M^*/SFR_{tot}$ and $T_{db}^{blk} = M^*/SFR_{IR}^{blk}$. Comparing the latter quantity to the age (T) of the existing stellar population in the exposed region is particularly interesting, as this is a measure of the importance of the completely dust-blocked region in the future evolution of the galaxy.

Finally, the measurement of L_{IR} enables us to examine the well-known FIR-radio relation (see Condon 1992 for review) for the sources that have radio data. We used the conventional formalism in Helou et al. (1985), which takes the form of

$$q_{IR} = \log[(S_{IR}/3.75{\times}10^{12} W m^{-2} Hz^{-1})/(S^0_{1.4GHz}/W m^{-2} Hz^{-1})],$$

where S_{IR} is the integrated IR flux while $S^0_{1.4GHz}$ is the radio flux density at the restframe 1.4 GHz. For the k-correction in radio, we assume $S_\nu \propto \nu^{-0.8}$. The original usage of S_{IR} (the quantity "FIR" in Helou et al. 1985) is defined between the restframe 42.5 and 122.5 μm. In order to take the full advantage of the *Herschel* spectral coverage, we opted to adopt S_{IR} as in Ivison et al. (2010), where this quantity is defined from 8 to 1000 μm in the restframe. In practice, we calculated S_{IR} using the best-fit SK07 model. For reference, the mean value that Ivison et al. (2010) obtain using *Herschel* sources in the GOODS-N is $q_{IR} = 2.40 \pm 0.24$.

4. SOURCES IN THE GOODS-N

4.1. *GOODSN06 (J123634.3+621241)*

This source is in the SMG sample of Wang et al. (2004; their GOODS 850-19), however it was detected at $< 4\sigma$ level ($S_{850} = 3.26 \pm 0.85$ mJy) and was not included in the SMA observations of Barger et al. (2012).

4.1.1. *Morphologies and Potential Components*

[14] Using the conversion for a Salpeter IMF, the SFR will be a factor of 1.7 higher.

Fig. 2 shows this source in various bands from 250 μm to H_{160}. Within 18″ radius, there are 74 objects in H_{160} that have $S/N \geq 5$ (measured in the MAG_AUTO aperture). By inspecting the FIR and the 24 μm images, it is obvious that only six of these objects could possibly contribute to GOODSN06. In order of the distances between their centroids to the 250 μm position, these potential components are marked alphabetically from "A" to "F". Objects A, B and C, which are 1.″38, 2.″50, and 3.″15, away from the 250 μm position, respectively, are completely blended in the 24 μm image as one single source. This is the brightest 24 μm source within 18″ ($S_{24} = 446 \pm 5$ μJy), and also dominates the flux in 70 μm. The centroid of this single 24 μm source also coincident with the centroid of the emission in 100, 160 and 250 μm. In the 8.0 μm image, A and C are separated and both are well detected, and hence it is reasonable to assume that they both contribute to the 24 μm flux. B is still blended with A in the 8.0 μm image, and we cannot rule it out as a contributor to the 24 μm flux. Under our assumption, this means that these three objects could all be contributors to the FIR emission.

As it turns out, A and C have spectroscopic redshifts of 1.224 and 1.225, respectively (Barger et al. 2008). Their separation is 2.″64, which corresponds to 22.1 kpc at these redshifts, and is well within the scale of galaxy groups. This suggests that they could indeed be associated. The high resolution *HST* images reveal that both A and C have complicated morphologies and that B could be part of A. This is show in Fig. 3. While it is difficult to be separated photometrically, A is actually made of three sub-components, which we label as "A-1", "A-2" and "A-3" (Fig. 3, left). The ACS images show that A-1 has a compact core and a one-side, curved tail. A-2 is invisible in the ACS optical images, but it is the most prominent of the three in the WFC3 IR, and also has a compact core. A-3 is similar to A-1 in the WFC3 IR but extends to the opposite direction and is much fainter. The one-side, curved tail of A-3 is invisible in the ACS optical. The core of A-2 has nearly the same angular separation from those of A-1 and A-3, which is about 0.″38, or 3.2 kpc at $z = 1.22$. Therefore, A is likely a merging system. In fact, B could well be part of this system, as it seems to connect with the tail of A-3. C looks smooth and regular in the WFC3 images, however in the higher resolution ACS images it shows two nuclei, which is also indicative of merging process (Fig. 3, right). All this suggests that it will be reasonable to consider the A/B/C complex as a single system when treating the FIR emission.

While it is only marginally detected in 24 μm, component D seems to have non-negligible fluxes in both 70 and 100 μm. This object is invisible in B_{435} and V_{505}, and is marginally detected in i_{775}, but starts to be very prominent in z_{850} and in the WFC3 IR and the IRAC bands. Its morphology in z_{850} is rather irregular and shows two sub-components in Y_{105} and J_{125}. However in H_{160} it looks like a normal disc galaxy. While all this suggests that it could be a dusty galaxy and thus could have non-negligible FIR emission, its position is 8.″88 offset from the the 250 μm centroid, and thus is less likely a major contributor to the 250 μm flux.

Finally, E and F cannot be associated with any of the above because they have spectroscopic redshifts of 0.562 and 0.9617, respectively (Barger et al. 2008). While both of them are prominent sources in 24 μm, only E is well visible in 160 μm and thus could be a significant contributor to the FIR emission.

4.1.2. *Optical-to-near-IR SED Analysis*

The optical-to-near-IR SED analysis for objects A to D follows the procedure outlined in §3.2. The SED was constructed based on the photometry in the ACS, the WFC3 IR and the IRAC bands. The ACS and the WFC3 photometry were obtained by running the SExtractor software (Bertin & Arnouts 1996) in dual-image mode on the set of images that are registered and PSF-matched to the H_{160}-band. The H_{160} image was used as the detection image, and the colors were measured in the MAG_ISO apertures. The H_{160} MAG_AUTO magnitudes are then adopted as the reference to convert the colors to the magnitudes that go into the SED. The IRAC magnitudes are the TFIT results using the H_{160} image as the morphological template and the PSF derived from the point sources in the field.

The results are summarized in Fig. 4, which include z_{ph} and the physical properties of the underlying stellar populations such as the stellar mass (M^*), the extinction A_V, the age (T), the characteristic star forming time scale (τ), and the dust-corrected star formation rate (SFR). This figure also shows $P(z)$, which is the probability density function of z_{ph}, for all these objects. The available z_{spec} agree with our z_{ph} reasonably well. The largest discrepancy happens in C, which has $\Delta z = 0.185$, or $\Delta z/(1+z) = 0.08$. This discrepancy is explained by the secondary $P(z)$ peak at $z_{ph} \sim 1.2$. Object B, a very close neighbor to A, has $z_{ph} = 0.93$, which may seem to suggest that it is not related to A. However, its $P(z)$ is rather flat over all redshifts and does not have any distinct peak, and therefore its z_{ph} cannot be used as a strong evidence to argue for or against its relation with A. From these results and the morphologies, it is reasonable to believe that B is only a less important satellite to A. Object D has $z_{ph} = 1.34 \pm 0.04$, and is different from z_{spec} of the A/C complex by $\Delta z/(1+z) = 0.05$. This is within the accuracy of our z_{ph} technique, suggesting that D could be in the same group. Nevertheless, in the following analysis we still treat it separately.

4.1.3. *Decomposition in Mid-to-Far-IR*

The decomposition of GOODSN06 was done in the SPIRE 250 μm, the PACS 160 and 100 μm, and the MIPS 70 and 24 μm. This source has two neighbors to the south ("S1" and "S2"), which, while being outside of $r = 18''$, could still contaminate the target in the 250, 160 and 70 μm bands where the beam sizes are large. While in other cases we only fit the objects within $r = 18''$, for this source we must consider these two contaminators that are further out. We adopted their positions in H_{160}, as there is no ambiguity in their identifications, and fit them together with all the components of GOODSN06 when decomposing in these three bands. They are well separated from the target in 100 and 24 μm, and hence did not enter the decomposition process in these two bands.

For illustration, Fig. 5 shows the decomposition in 250 μm. The simultaneous fit to all the five objects within $r = 18''$ (A to E) resulted in B and C as the only

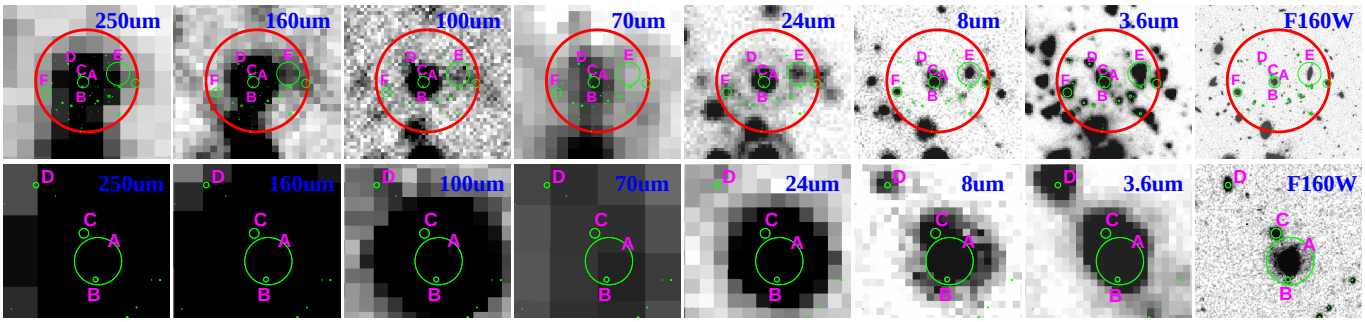

FIG. 2.— Vicinity of GOODSN06 (top) and zoomed-in view of its possible contributors (bottom) in SPIRE 250 μm, PACS 160 and 100 μm, MIPS 70 and 24 μm, IRAC 8 and 3.6 μm, and WFC3 H_{160}. North is up and east is to the left. The red circles have 36″ diameter, twice the beam FWHM at 250 μm. The objects identified in H_{160} within this radius are marked by the green circles whose sizes are proportional to their H_{160} brightnesses. The possible contributors to the 250 μm emission are labeled by the letters in purple.

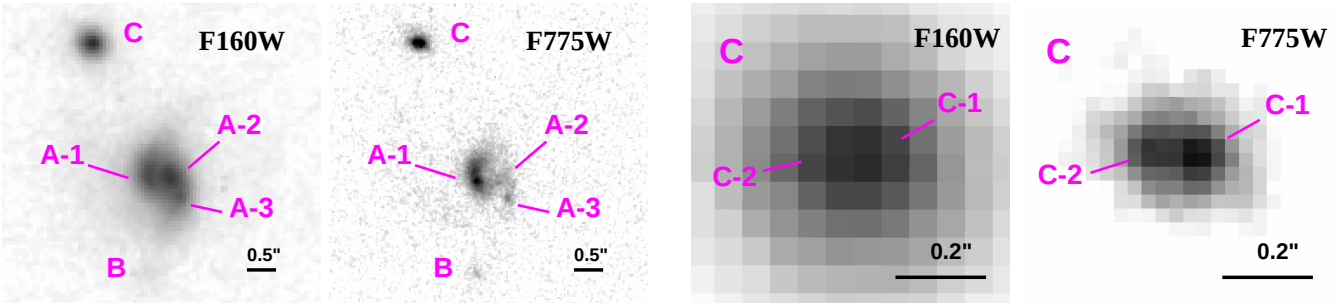

FIG. 3.— Detailed morphologies of A (left) and C (right) in H_{160} and i_{775}. The sub-components are labeled numerically. A-2 is prominent in NIR but is very weak in optical, indicating that it is obscured by dust. C shows double nuclei in the higher resolution i_{775} image.

two survivors. However, GALFIT reported very large flux errors for these two objects, and their extracted fluxes would have very low GALFIT fitting S/N (< 3 and < 0.5, respectively). Removing either of the two did not improve the result. Therefore we had to use the trial-and-error approach. Judging from the mid-IR images (§4.1.1, in particular the 24 μm image) and from the optical-to-NIR SED analysis (§4.1.2), it is reasonable to conclude that A, B and C are associated, with A being by far the most dominant. The forced fit for A only, however, showed a severe oversubtraction and yet a clear residual at the location of E. The forced fit at A and E significantly improved, however the extraction at A still had a large error. When we included the two southern neighbors (S1 and S2) and fit them together with A and E, the error of A was greatly reduced. If we left out E, the residual persistently showed up at this location, indicating that the contamination from S1 and S2 is not the reason and that the inclusion of E is necessary. The fit with A, E, S1 and S2 seems to be the best among all possibilities, and forcing the fit to additional objects would create completely non-physical results. Therefore, we adopted the A+E+S1+S2 scheme, which concludes that A contributes 82% of the total flux to GOODSN06 and E contributes the other 18%.

The automatically iterative decomposition procedure was successful in other bands. In 160 μm, it converged on A+E, and introducing S1 further reduced the errors and improved the residuals. In 100 μm, it converged on A+D+E and did not need to include the southern neighbors. In 70 μm, it converged on A+E+F, and including both S1 and S2 further improved the results. In 24 μm, it converged on A+E+F. In all these bands, A is the most dominant object as well.

The flux densities of the major component A based on the above decomposition results are summarized in Table 2. The VLA 1.4 GHz data from Morrison et al. (2010), which have the positional accuracy of 0.″02–0.″03, reveal a source with $S_{1.4GHz} = 0.201 \pm 0.010$ mJy at $RA = 12^h36^m34^s.49$, $DEC = 62^o12'41''.0$, and is right at the location of A-2. A is also a moderate X-ray source in Alexander et al. (2003), which has rest-frame 0.5–2 keV luminosity of $L_{0.5-2} = 8.1 \times 10^{41}$ erg/s (Barger et al. 2008), and hence most likely is powered by stars rather than AGN (see e.g., Georgakakis et al. 2007).

4.1.4. *Total IR Emission and Stellar Populations*

Fig. 6 shows our fit to the mid-to-far-IR SED, which results in $L_{IR} = 4.0 \times 10^{12} L_\odot$ at $z_{spec} = 1.225$. This is in the ULIRG regime. Based on the optical-to-near-IR SED fitting in §4.1.2., we integrated the difference between the reddened, best-fit model template spectrum of A and its de-reddened version (see §3.2), and obtained $L_{IR}^{ext} = 2.3 \times 10^{12} L_\odot$. The "net" IR luminosity from the region completely blocked by dust is therefore $L_{IR}^{blk} = 1.7 \times 10^{12} L_\odot$, which implies $SFR_{IR}^{blk} = 170\ M_\odot/yr$. The best-fit BC03 model for A in §4.1.2 gives $SFR_{fit} = 236\ M_\odot/yr$. Thus $SFR_{tot} = 406\ M_\odot/yr$. While the A/B/C complex is very likely an interacting system, it is interesting to notice that the ULIRG phenomenon only happens to A, and that B and C are not triggered. Furthermore, it seems that the current star formation activities all concentrate on A. The best-fit model for C is a SSP, which formally has no on-going star formation. It is plausible that A itself is an on-going merger (judging from its complex morphology) and hence

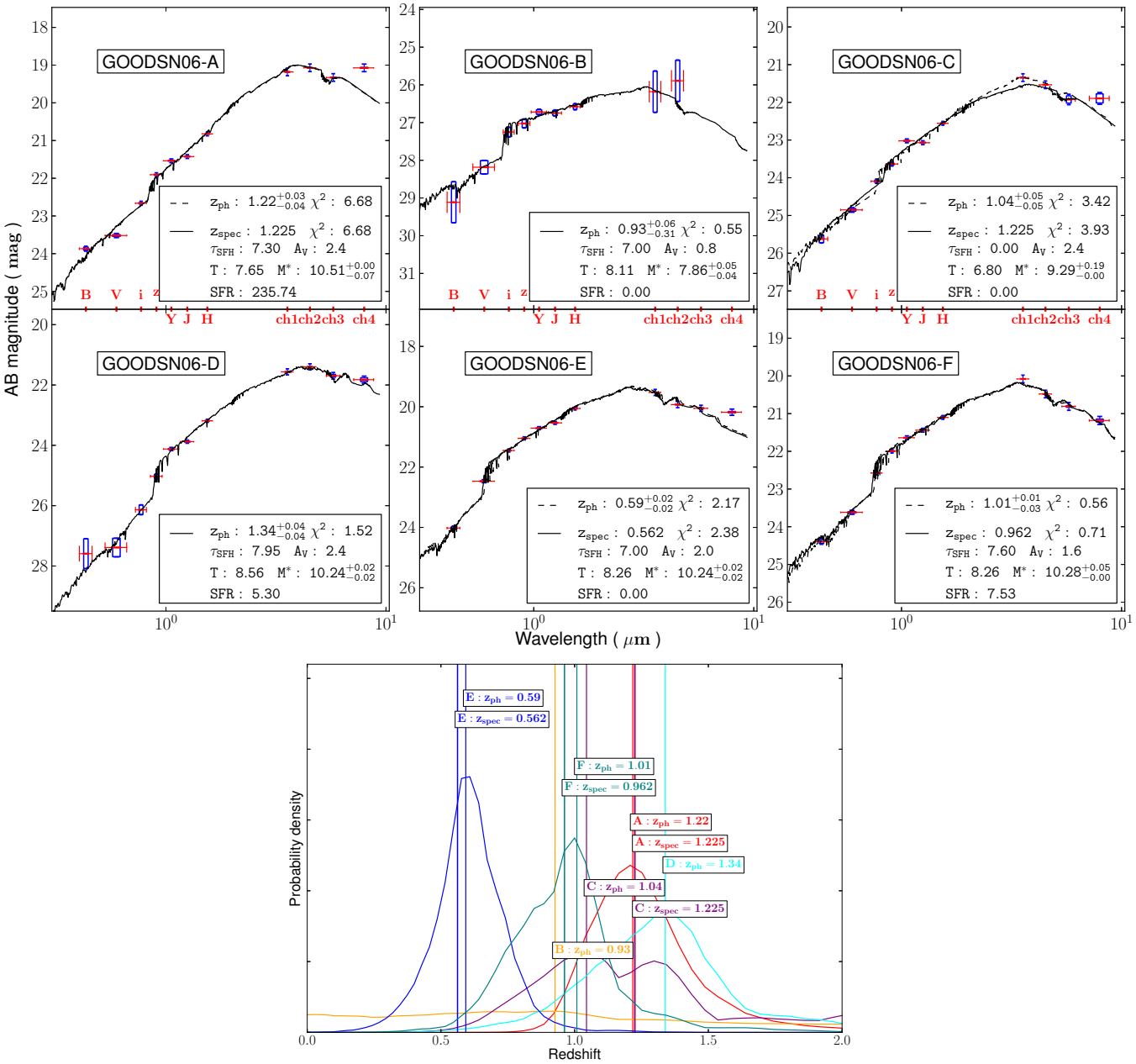

FIG. 4.— Optical-to-NIR SED analysis of the possible contributors to GOODSN06. The top panel summarizes the SED fitting results of these objects individually. The data points are shown together with the best-fit BC03 models. For the objects that have z_{spec}, the solid curves are the best-fit model at this redshift, while the dashed curves are the best-fit model when z is a free parameter. The most relevant physical properties inferred from the models are summarized in the boxed region: reduced χ^2, τ (in Gyr), A_V, T ($\log T$ in year), $M*$ ($\log M^*$ in $M_\odot$), and SFR_{fit} (in $M_\odot/yr$). The bottom panel shows the probability distribution functions of the photometric redshifts ($P(z)$) of these objects, which are distinguished by different colors. The best-fit z_{ph} and the z_{spec} (when available) values are shown in boxes, and are also marked by the vertical lines.

is undergoing an intense starburst, while its companion C and the smaller satellite B are still on the way falling to it.

The stellar mass of this system is also dominated by A, for which we obtained 3.2×10^{10} $M_\odot$ (§4.1.2). The stellar mass of C is one order of magnitude less at 1.9×10^9 $M_\odot$ and is negligible. Therefore, this implies $SSFR = 12.7$ Gyr^{-1}. Using the stellar mass doubling time scales as discussed in §3.2., we obtained $T_{db}^{tot} = 79$ Myr and $T_{db}^{blk} = 188$ Myr, respectively. Interestingly, the optical-to-near-IR SED fitting for A in §4.1.2 gives an age of $T = 45$ Myr. Its SFH has $\tau = 20$ Myr, which is comparable to this best-fit age. In other words, the SFH of the exposed region is a rather short burst, and this every young galaxy has been in star-bursting mode ever since its birth, although it is unclear whether it could be an ULIRG in the earlier time. While the star formation in the completely dust-blocked region is playing a less important role as the compared to that in the exposed region (T_{db}^{blk} is more than a factor of four longer than T), it will still be significant should the gas reservoir suffice (see below).

The fit for the dust temperature and the dust mass is shown Fig. 6. $T_d^{fit} = 48.7$ K is on the high side of the

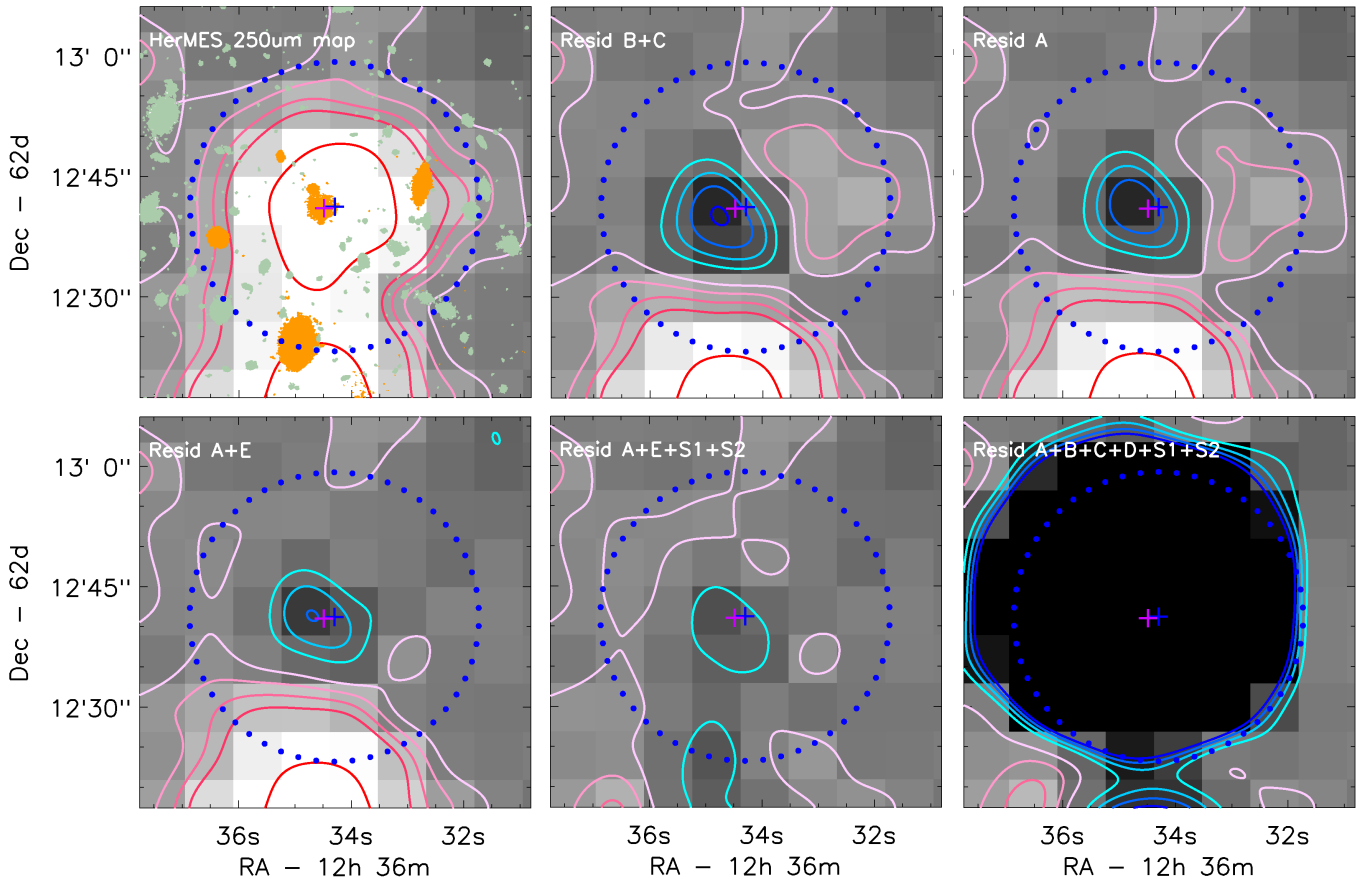

FIG. 5.— Demonstration of the decomposition in 250 μm for GOODSN06. The first panel shows the original 250 μm image, while the others show the residual maps of the different decomposition schemes where different input sources are considered (labeled on top). The "B+C" panel is for the automatically interactive fit that fails to provide a satisfactory result, while the rest are for different trial-and-error runs where the input objects are interactively decided. The best result is produced by the "A+E+S1+S2" scheme (see text). All images are displayed in positive, i.e., using white for the positive values and black for the negative values. The contours coded in "warm" and "cold" colors indicate the different positive (i.e., residuals) and negative (i.e., over-subtraction) levels, respectively: the positive level increases from light pink to dark red, and the negative level increases from light green to deep blue. The contour starts at the level of $\pm$ 0.4 mJy/pix, and increases or decreases at a step size of 0.4 mJy/pix. In the first panel that shows the original 250 μm image, the H_{160}-band objects are superposed as the gray-green segmentation maps, among which the candidate counterparts are further highlighted in orange. In all panels, the blue, dotted circle is 18″ in radius. The blue and the magenta crosses mark the 250 μm source centroid and the VLA 1.4 GHz source position, respectively.

usual dust temperatures of the SMGs, which are around $\sim$ 30–40 K (e.g., Chapman et al. 2005, 2010; Pope et al. 2006; Magnelli et al. 2010, 2012; Swinbank et al. 2013). In fact, as mentioned earlier, GOODSN06 is only a marginal SMG and has $S_{850} = 3.26 \pm 0.85$ mJy. This is a demonstration that the *Herschel* bands are less biased against ULIRGs of high dust temperature. From the best-fit SK07 model, one would predict $S_{850} = 2.29$ mJy, in agreement with the actual measurement to 1.14 σ. The dust mass we obtained is $M_d = 3.7 \times 10^8 M_\odot$. If assuming the nominal gas-to-dust ratio of $\sim$ 140, the gas reservoir is $5.2 \times 10^{10} M_\odot$, sufficient for the whole system to continue for another $\sim$ 130 Myr or the dust-blocked region for $\sim$ 300 Myr.

Finally, we examine the FIR-radio relation using the formalisms summarized in §3.2, for which we obtained $q_I R = 2.44$, which is in good agreement with the mean value of 2.40 ± 0.24 of Ivison et al. (2010).

4.2. *GOODSN63 (GOODSN-J123730.9+621259)*

This source has a multi-wavelength dataset nearly as rich as GOODSN06 does except that it lacks 70 μm image. While being a single source in 250 μm, it breaks up into two sources (but still blended) in 160 and 100 μm. According to the PEP DR1 catalog, these two PACS components have $S_{160} = 22.8 \pm 1.4$ and 9.5 ± 1.2 mJy, and $S_{100} = 4.9 \pm 0.4$ and 3.6 ± 0.4 mJy, respectively. This source is a previously discovered SMG (Wang et al. 2004, their GOODS 850-6), whose position has been precisely determined by the SMA observations to be $RA = 12^h37^m30.80^s$, $DEC = 62^o12'59.00''$ (J2000), and has $S_{850} = 14.9 \pm 0.9$ mJy (Barger et al. 2012).

4.2.1. *Morphologies and Potential Components*

Fig. 7 shows the images of GOODSN63. Within 18″ radius, there are 63 objects in H_{160} with $S/N \geq 5$. The inspection shows that only four of them could be significant contributors in the FIR. These four objects, marked alphabetically as "A" to D", are 1.″68, 3.″40, 6.″86, and 10.″27 away from the 250 μm position, respectively. In 24 μm, A and B are blended as a single source, while C and D are blended as another. These are the two brightest 24 μm sources within $r = 18''$, and their positions are consistent with the two local maxima in 160 and 100 μm. The brightest object in H_{160} (marked by the largest green circle in Fig. 7) has spectroscopic redshift of $z = 0.5121$

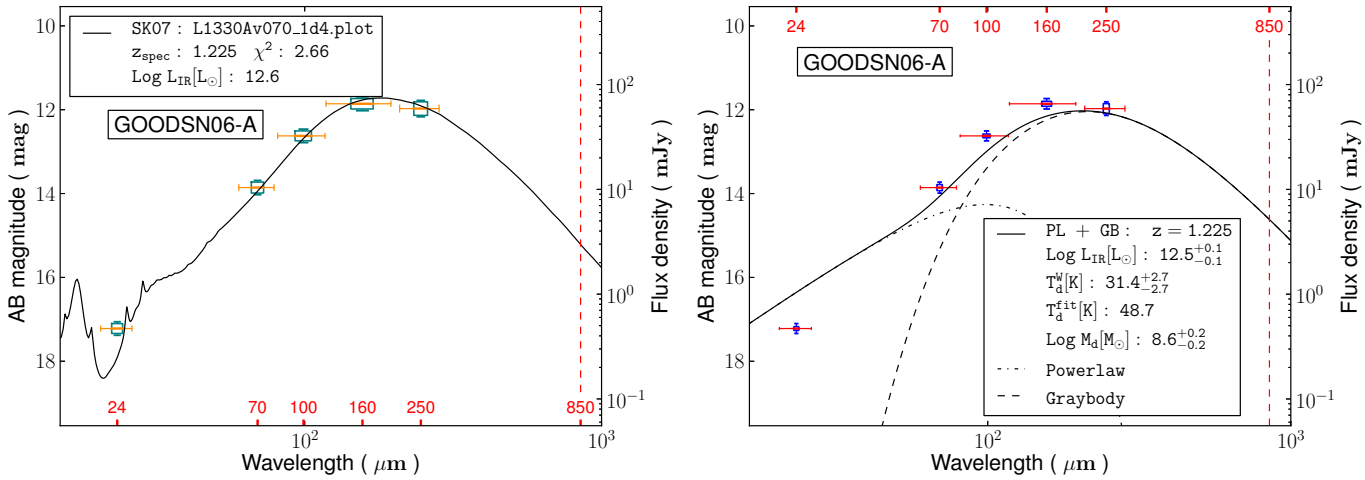

FIG. 6.— Mid-to-FIR SED fitting of GOODSN06-A at $z_{spec} = 1.225$. The relevant parameters derived from the fits are summarized in the boxed regions. The left panel shows the fit to the SK07 models to derive L_{IR}, where the green boxes are the data points and the superposed curve is the best-fit model. The right panel shows the fit to derive the dust temperature and the dust mass, where the analytic models are made of a power law and a graybody (see §3.2). The data points are shown in blue. The best-fit model is shown as the black, solid curve, while its power-law and graybody components are shown as the dot-dashed and the dashed curves, respectively. In both panels, the most relevant best-fit parameters are summarized in the boxes. The red vertical dashed lines are at 850 μm, which is the wavelength where SMGs are selected.

(Barger et al. 2008) and is not visible in 24 μm at all, and hence it is not likely to have any significant FIR emission.

Objects A and B show complex morphologies. The WFC3 IR images reveal that A consists of two subcomponents, A-1 and A-2, which are only 0.″30 apart (Fig. 8, left). A-2 is completely invisible in all the ACS bands. In the IR images, B shows a dominant core that is irregular in shape, and also has irregular, satellite components to its north-western side. In the ACS images, its core is less distinct, and the satellite components are invisible. All this suggests that both A and B are likely very dusty systems, and that both could be going through violent merging process. While the small separation between them (1.″80) suggests that they could be an interacting pair, our SED analysis below shows that they actually are not associated.

Objects C and D are 3.″42 apart. They have spectroscopic redshifts of 0.9370 and 1.3585, respectively (Barger et al. 2008), and therefore are not associated. The morphologies of these two objects are shown in Fig. 8 (right) in details. While it is a rather smooth disc galaxy in the restframe optical, C shows knotty structures and dust lanes in restframe UV, suggestive of active star formation. On the other hand, D appears as a smooth spheroid in restframe UV to optical. All this suggests that C is the major contributor to the 24μm flux, which is consistent with the 24 μm morphology as the 24 μm centroid is closer to the position of C than to D.

4.2.2. *Optical-to-near-IR SED Analysis*

Fig. 9 summarizes the results of the optical-to-near-IR SED analysis for the four potential components. The SEDs used here are based on the same photometry as in §4.1.2 except for A, where it is augmented by the U-band image.

The fitting of C gives $z_{ph} = 0.93$, in excellent agreement with its $z_{spec} = 0.937$. D has $z_{ph} = 1.22$ as opposed to $z_{spec} = 1.359$, nevertheless they are still in reasonable agreement ($\Delta_z/(1+z) = 0.06$). A and B do not have spectroscopic redshifts. B is not detected in the U-band image, and would be selected as an LBG at $z \approx 3$. In fact, the fit to its SED, either with or without including the U-band constraint, gives $z_{ph} = 3.04$.

A deserves some more detailed discussion. The single-component fit as used for other objects fails to explain the SED of A. We have also tested a different set of SFHs where the SFR increases with time (Papovich et al. 2011), however A still cannot be fitted by a single component. Briefly, the strong IRAC fluxes and the large break between WFC3 IR and IRAC tend to assign a high redshift of $z_{ph} \gtrsim 3$ to the object, which would then give an implausibly high stellar mass of $> 10^{12} M_\odot$. On the other hand, the optical fluxes (especially the detection in the U-band) are only consistent with significantly lower redshifts. Therefore, we attempted to fit this object with two components. We took a two-step approach. We first fit the blue part of the SED up to H_{160}, using the whole set of BC03 models as usual. We obtained the best-fit at $z_{ph} = 2.28$. The best-fit model is of moderate stellar mass ($7.8 \times 10^9 M_\odot$) and age (1.0 Gyr), and has a very extended SFH ($\tau = 13$ Gyr) with the current $SFR_{fit} = 11.2\ M_\odot/yr$. This best-fit template, which extends to the IRAC wavelengths, was then subtracted from the original SED to produce the SED for the red part. This red part remains very strong in the IRAC bands, as the blue component only contributes a small amount at these wavelengths. It has nearly zero flux from U to J_{125}, but still has non-zero residual flux in H_{160}. We then fitted this red SED, from H_{160} to 8.0 μm, at the fixed redshift of 2.28 from the blue component. We also relaxed the constraint on the dust extinction and allowed A_V to vary from 0 to 10 mag. We indeed found a reasonable best-fit model, which is a highly extincted ($A_V = 6.8$ mag), high stellar mass ($4.7 \times 10^{11} M_\odot$), old (age 2.0 Gyr) burst ($\tau = 10$ Myr). The result of this two-step fit is summarized again in Fig. 9 with more details. While this is probably not the unique solution, it offers a plausible explanation to the SED of A. In addi-

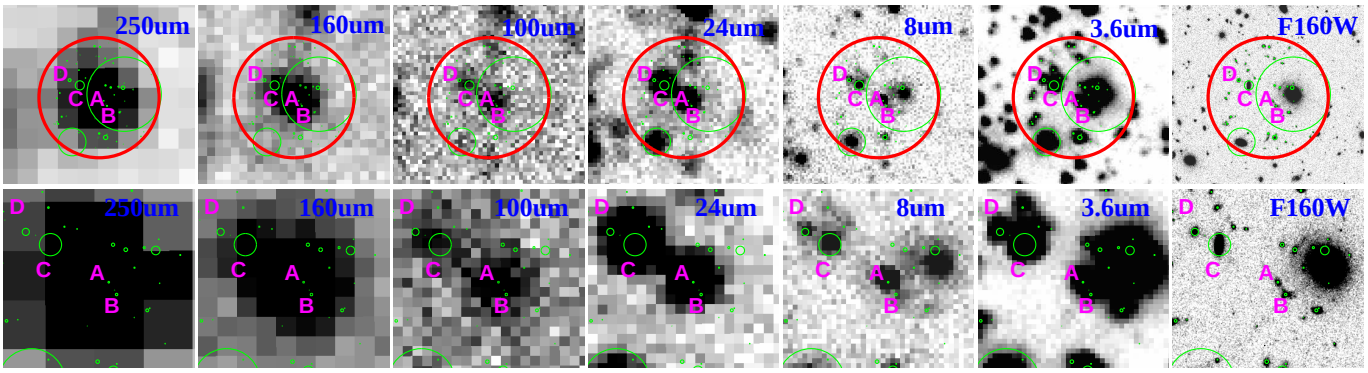

FIG. 7.— FIR to near-IR images of GOODSN63. The organization and the legends are the same as in Fig. 2. This source does not have MIPS 70 μm data. The possible contributors to the 250 m emission are labeled by the letters in purple.

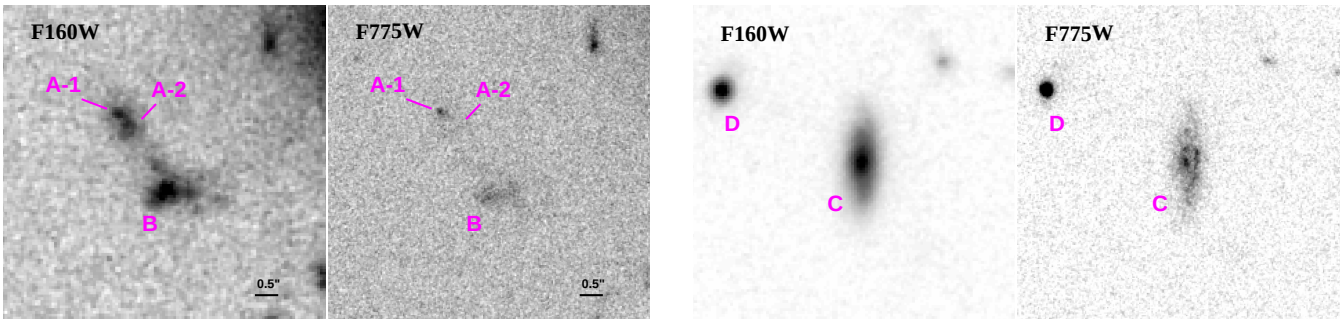

FIG. 8.— NIR and optical morphologies of the possible contributors to GOODSN63, shown in H_{160} and i_{775}. The left panel is for A and B, and the right panel is for C and D. A clearly breaks up into two sub-components in H_{160}, labeled as "A-1" and "A-2", the latter of which is only barely visible in optical.

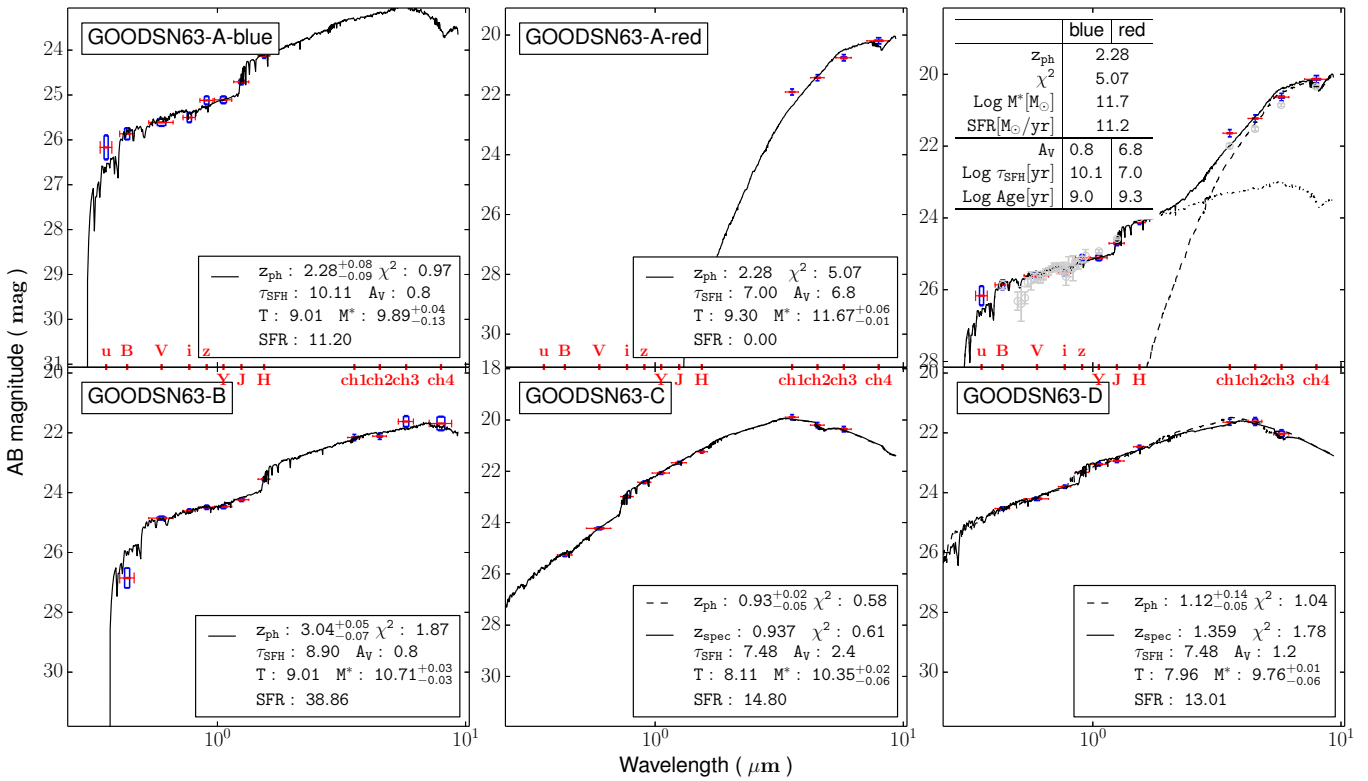

FIG. 9.— Optical-to-NIR SED analysis of the possible contributors to GOODSN63. Legends are the same as in Fig. 4. The three panels on the top are all for object A: from left to right, these are the fit to its blue sub-component, its red sub-component, and the sum of the two. The grey data points in the upper-right panel are from the Rainbow database. Note that the "blue" and the "red" refer to the SED sub-components but not the morphological sub-components A-1 and A-2. See text for details.

tion, we also examined if the red part could be explained by a power-law AGN in the form of $f_\nu \propto \nu^{-\alpha}$. The commonly adopted slope is $\alpha = 1.0$–1.3 in the restframe near-IR (i.e., the IRAC bands in the observer's frame for this object), and changes to a flatter value of $\alpha = 0.7$–0.8 when extending into the restframe optical regime (see e.g., Elvis et al. 1994; Richards et al. 2006; Assef et al. 2010). Such power-laws, however, cannot provide any reasonable fit to the data. We found that the IRAC data points, with or without the extension to the MIPS 24 μm, could only be explained by a very steep slope of $\alpha = 1.8$–1.9. Adopting this slope in the restframe optical and ignoring the possible flattening of the SED, we would get still get $H_{160} \sim 23.6$ mag, which is much higher with the requirement of $H_{160} = 28.8$ mag based on the SED of the red part. In fact, this is also significantly brighter than the observed total of H_{160}=24.12 mag. While we cannot definitely rule out the possibility that there might be an embedded AGN in GOODSN63-A, there is no compelling evidence that such an AGN component exists. Based on our analysis, we believe that the optical-to-near-IR emission of GOODSN63-A is dominated by stellar populations.

Interestingly, Barger et al. (2012) derive $z_{ph} = 2.7$ for GOODSN63 based on the radio-to-sub-mm flux ratio. To further check on the redshift of this GOODSN63-A, we used the "Rainbow" database in the GOODS-N, which incorporates the 24 narrow-band images (0.50–0.95 μm) from the Survey of High-z Absorption Red and Dead Sources program (SHARDS; Pérez-González et al. 2013) and the GOODS & CANDELS ACS/WFC/IRAC data as used above (see the grey data points in the upper right panel of Fig. 9). This database gives $z_{ph} = 2.4$ for this object, which agrees with $z_{ph} = 2.28$ quite well considering the different photometry in these two approaches. We adopt $z_{ph} = 2.28$ for the analysis below.

4.2.3. *Decomposition in Mid-to-Far-IR*

The automatically iterative decomposition of GOODSN63 was successful in all bands from 250 μm to 24 μm. In 24 μm, B has zero flux. We have tried to decompose by subtracting A first, and find that the residual image has no flux left at the position of B, consistent with the simultaneous fit. This probably is not surprising, because B, while being brighter than A from V_{606} to H_{160}, steadily becomes much fainter than A when moving to the redder and redder IRAC channels ($> 1.5\times$ fainter in 8.0 μm). The simultaneous fit in other bands also gives zero flux for B. Similar to B, D also has zero flux in 100, 160 and 250 μm. Therefore, the two distinct sources in the 100 and 160 μm described at the beginning of §4.2 should corresponds to A and C, respectively.

The automatically iterative decomposition shows that C also has zero flux in 250 μm, leaving A as the sole object responsible for the emission in this band. The decomposition in this band is shown in Fig. 10. The decomposition settled on A with a very reasonable error estimate, and left no detectable fluxes at the positions of any other sources. We also tried the trial-and-error approach by adding C and/or D (although D probably should not be involved in the first place given its zero fluxes in 100 and 160 μm), which produced equally acceptable results. However, our decomposition rule is that the automatically iterative approach always takes the precedence as long as the results are reasonable, and therefore we adopted A as the only contributor to the 250 μm emission. This decision is also supported by the fact that the flux ratio of A to C gradually increases with the wavelengths, increasing from 0.77:1 at 24 μm to 3.47:1 at 160 μm, consistent with the picture that A is much more dominant in the FIR. This also raises the point that one should not blindly take the brightest 24 μm source within the *Herschel* beam as the counterpart.

The above results mean that it is possible to include the data in 350 and 500 μm for further analysis, as there should not be any other neighbors that could contaminate the light from A in these two bands. The final mid-to-far-IR flux densities of GOODSN63-A that we adopt are summarized in Table 2.

4.2.4. *Total IR Emission and Stellar Populations*

The A-only decomposition result above is supported by the SMA observation of this source (see §4.2; Barger et al. 2012), which reveals a single source whose position is on A-1. This is also supported by the VLA 1.4 GHz data, where there is a source with $S_{1.4GHz} = 0.123$ mJy coinciding with A. The radio position is at $RA = 12^h37^m30^s.78$, $DEC = 62^o12'58''.7$, which is right in between A-1 and A-2 (Morrison et al. 2010). There is no X-ray detection of GOODSN63 in the 2Ms *Chandra* data (Alexander et al. 2003), which have the limit of 2.5×10^{-17} $erg/s/cm^2$ in the most sensitive 0.5–2 keV band. At $z = 2.28$, this corresponds to an upper limit of 1.0×10^{42} erg/s in the restframe 1.6–6.6 keV, which is at the border line of AGN. Therefore, we believe that the FIR emission of GOODSN63 is most likely powered by stars.

We derived L_{IR} using the mid-to-far-IR SED from 24 to 500 μm, fixing the redshift at $z_{ph} = 2.28$. The result is summarized in the left panel of Fig. 11. The best-fit SK07 model is heavily dust-extincted, with $A_V = 12.0$ mag. We obtained $L_{IR} = 7.9 \times 10^{12} L_\odot$, and therefore this object is an ULIRG. The contribution from the dust re-processed light in the exposed region only amounts to $L_{IR}^{ext} = 8.7 \times 10^{10} L_\odot$, and thus $L_{IR}^{blk} = 7.8 \times 10^{12} L_\odot$ and $SFR_{IR}^{blk} = 781 M_\odot/yr$. In contrast, as described in §4.2.2, it has $SFR_{fit} = 11.2 M_\odot/yr$, which is contributed solely by the blue component of A. The stellar mass of this system is dominated by the red subcomponent of A, which is $4.7 \times 10^{11} M_\odot$. Therefore, we get $SSFR = 1.69 Gyr^{-1}$ (or $T_{db}^{tot} = 593$ Myr), and $T_{db}^{blk} = 602$ Myr. The latter doubling time is vastly different from that inferred for GOODSN06, and is much longer than the typical lifetime of 10–100 Myr of an ULIRG. Nevertheless, it is still much shorter $T = 2.0$ Gyr of the exposed stellar population. The dust temperature and the dust mass of this system, $T_d = 39.4$ K and $M_d = 3.6 \times 10^9 M_\odot$ are typical of SMGs. The best-fit SK07 model predicts $S_{850} = 9.81$ mJy, consistent with the actual observation. The dust mass implies the gas mass of $M_{gas} = 5.6 \times 10^{11} M_\odot$, sufficient to fuel the ULIRG for the next ~ 700 Myr.

The red subcomponent of A is a short burst ($\tau = 10$ Myr) that is 2 Gyr old (§4.2.2), which implies that the majority of the existing stellar mass of this system was formed in an intense star-bursting phase at $z > 5$,

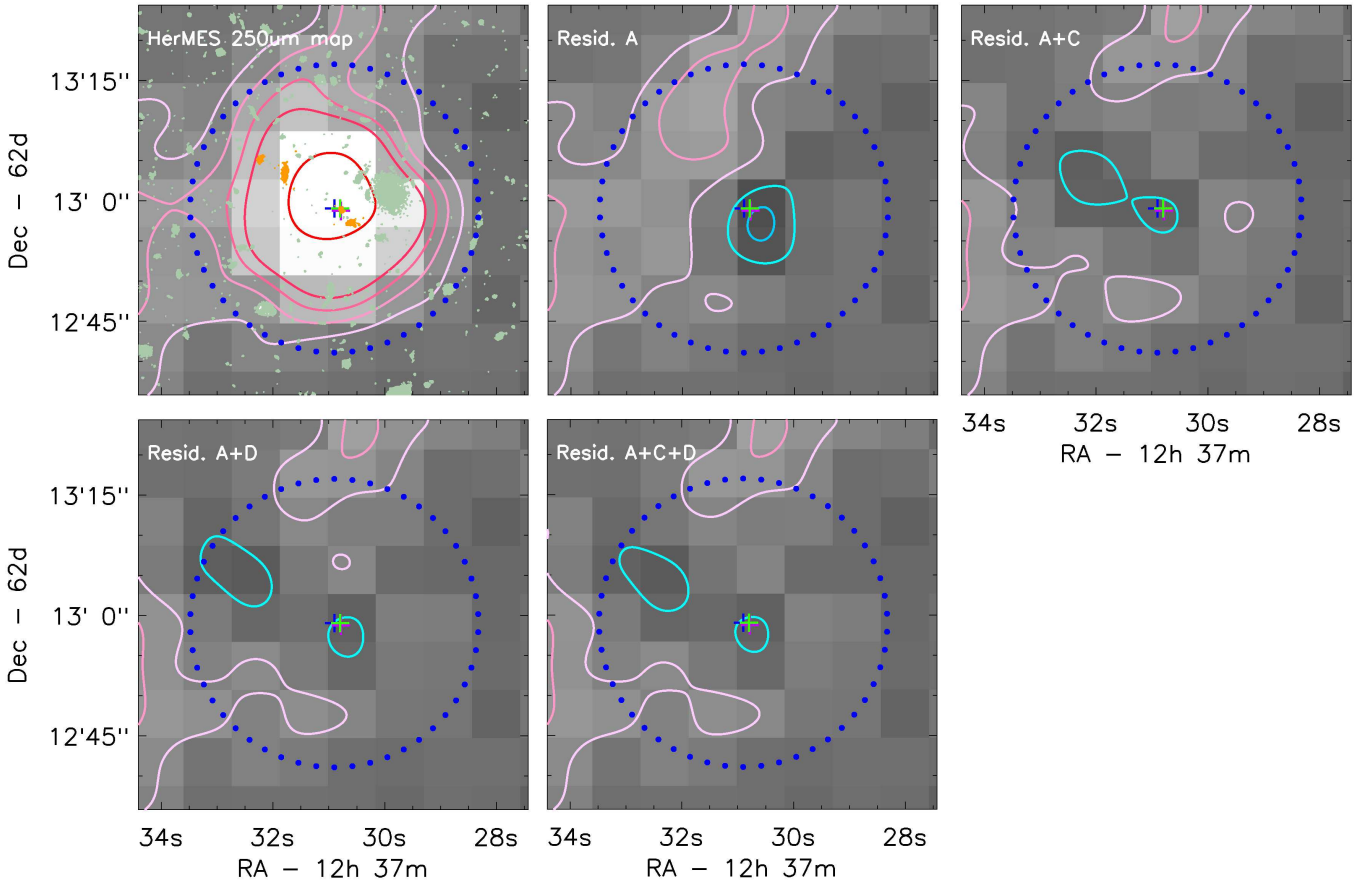

FIG. 10.— Demonstration of the decomposition in 250 μm for GOODSN63. The first panel shows the original 250 μm image, while the others show the residual maps of the different decomposition schemes where different input sources are considered (labeled on top). Legends are the same as in Fig. 5. In the addition to the blue and the magenta crosses, the bright green cross indicates the position of the SMA detection. The "A" panel is for the automatically iterative decomposition, which results in A as the only survivor and does not leave obvious residuals at the locations of other possible contributors. While the trial-and-error fits with the addition of C and/or D would produce equally acceptable results (other panels), the reasonable result from the automatically iterative approach always takes the precedence per our decomposition rule and hence A is deemed to be the sole contributor to 250 μm emission.

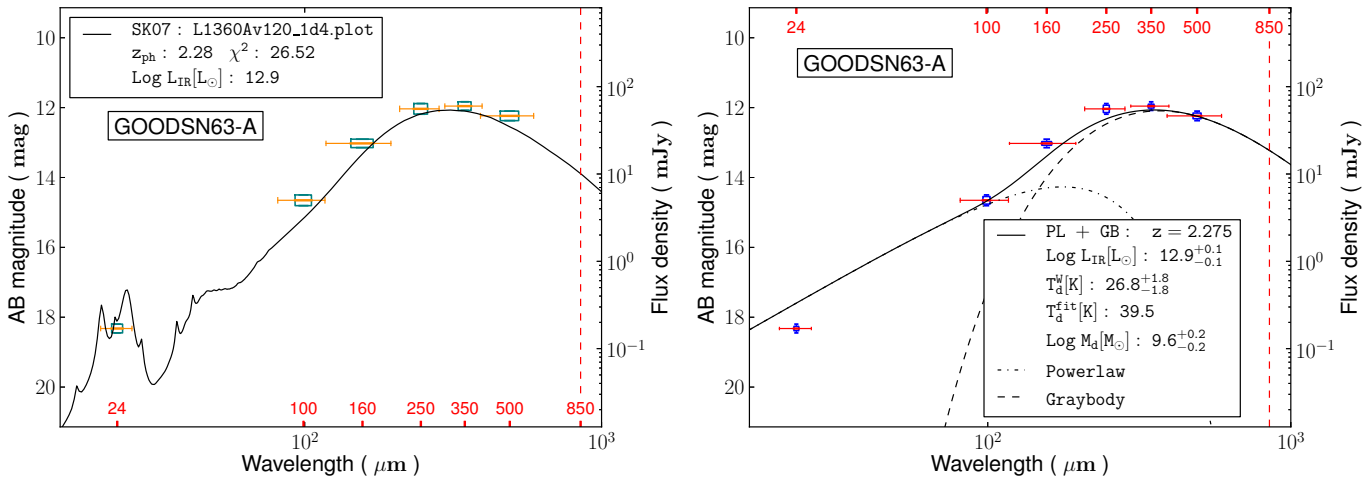

FIG. 11.— Mid-to-FIR SED fitting for GOODSN63-A at z_{ph} = 2.28. The SED incorporates the SPIRE 350 and 500 μm photometry directly from the HerMES catalog because A is the sole contributor at 250 μm and longer wavelengths and hence no decomposition in these two bands are necessary. The left panel shows the fit to the SK07 models, and the right panel shows the fit using the "power-law + graybody" models. Legends are the same as in Fig. 6.

and that the current ULIRG phase is an episode unrelated to the main build-up process of the existing system.

We also examined the FIR-radio relation for this system, and obtained $q_{IR} = 2.29$. This is lower but still consistent with the mean value of 2.40 ± 0.24 of Ivison et al. (2010).

5. SOURCES IN THE UDS

The two sources in the UDS have much shallower SPIRE data than those in the GOODS-N, because they are in a HerMES "L6" field. Unfortunately the PACS data are not yet released.

5.1. *UDS01 (UDS-J021806.0-051247)*

This source does not have data in the ACS, and we relied on the WFC3 IR data for their morphologies. The optical data from the CFHTLS-Wide were used in their optical-to-NIR SED analysis.

5.1.1. *Morphologies and Potential Components*

Fig. 12 shows the images of UDS01. Within 18″ radius, of the 250 μm position, there are 35 objects in H_{160} with $S/N \geq 5$. By comparing the 250 μm and the 24 μm images, we found that only nine of these objects could be significant contributors to the FIR flux. These objects are labeled from "A" to "H" according to their proximity to the 250 μm centroid, which lies in between B and C. B has spectroscopic redshift of $z = 1.042$ (Bradshaw et al. 2013; McLure et al. 2013).

At 24 μm, these nine sources are already severely blended. Nevertheless, we can still roughly distinguish two major sets based on their positions. The morphological details of these two sets in H_{160}, hereafter the "southern" and the "northern" sets, are shown in Fig. 13. The southern set includes A and B, which are 3.″9 apart, and are 2.″2 and 2.″5 from the 250 μm centroid, respectively. A is a small, compact object. B is by far the more dominant of the two in both IRAC and MIPS bands. In H_{160}, it shows a dominant core and an extended, irregular halo that is suggestive of a post-merger. The "northern" set includes C, D, E, F, and G. The dominant member in this set, as seen from IRAC to MIPS, is D, while C is the next in line. These two objects are 2.″8 and 3.″4 from the 250 μm centroid, respectively, and they are 2.″5 apart from each other. C has a spheroidal-like core, while D is more extended and has an irregular halo suggestive of a post-merger similar to B. E seems to be the companion of C, while G could be associated with D. F, on the other hand, already diminishes to invisible in 8 μm, and therefore is likely negligible at the longer wavelengths. Finally, I and H, which are small and compact and only 1.″6 apart in H_{160}, form a distinct, but the least important set.

5.1.2. *Optical-to-near-IR SED Analysis*

While the high-resolution WFC3 data have discerned the multiple objects in this region as discussed above, we cannot keep the same set of objects for the optical-to-NIR SED analysis due to the lack of the high-resolution ACS data in the optical. As the substitution, the CFHTLS-Wide data were used for the SED analysis. In principle, we could run TFIT on those data using the WFC3 data as the templates, however this was not practical because we discovered that the astrometric solution of the CFHTLS-Wide data is not entirely consistent with that of the CANDELS WFC3 data. As fixing this problem would be beyond the scope of this paper, our approach was to carry out independent photometry on the CFHTLS-Wide data alone and then to match with the WFC3 detections for the SED construction. For this purpose, we used SExtractor in dual-image mode and the i-band image as the detection image. C and E cannot be separated in these images, and thus we take them as one single source and will refer to it as C/E hereafter. E is > 3 mag fainter than C in J_{125} and H_{160}, and hence is negligible for the analysis of the stellar population. D and G are taken as one single source as well for the same reason, and G is > 5 mag fainter than D in the WFC3 and hence likely negligible. We refer to them as D/G hereafter. I is not visible in the CFHTLS data, and thus has to be excluded from this analysis. The colors of these objects were measured in the MAG_ISO apertures, and the i-band MAG_AUTO magnitudes were used as the reference to convert the colors to the magnitudes for the SED construction. In the near-IR, we used the CANDELS WFC3 J_{125} and H_{160}, and these magnitudes are obtained in the same way as in §4. In the longer wavelengths, we used the IRAC 3.6 and 4.5 μm data from the SEDS program. The objects are severely blended in the IRAC images, and hence we had to deblend by using TFIT to obtain reliable photometry of the individual objects. As in §4, the H_{160} image was used as the template for TFIT.

The photometric redshift results are summarized in Fig. 14. A is excluded because this faint object is not well detected in the CFHTLS-Wide data. Formally it has $z_{ph} = 3.5$, however this is not trustworthy because of the large photometric errors. As shown in the decomposition below, this object is irrelevant. B has $z_{ph} = 1.05$, which agrees very well with its $z_{spec} = 1.042$. C/E and D/G have $z_{ph} = 0.98$ and 1.09, respectively, and in terms of $\Delta z/(1+z)$ they agree to z_{spec} of B to 0.02 and 0.03, respectively, well within the accuracy of z_{ph} that can be achieved. The peaks of their $P(z)$ distributions overlap significantly. All this means that these three objects are very likely at the same redshifts and associated. C/E and D/G are separated by 2.″52, and B is 5.″25 away from them. At $z = 1.042$, these corresponds to 20.5 and 42.7 kpc, respectively, and are within the scale of galaxy groups.

The object of the highest stellar mass is D/G, which has $8.3 \times 10^{10} M_{\odot}$. It has a prolonged SFH with $\tau = 0.5$ Gyr, and its best-fit age is $T = 1.0$ Gyr. It has $SFR_{fit} = 39.0 M_{\odot}/yr$. All this suggests that the stellar mass assembly in D/G is a slow, gradual process. In contrast, B is best explained by a young SSP with an age of 130 Myr, and the inferred stellar mass is $4.6 \times 10^{10} M_{\odot}$. This indicates that it built up its stellar mass through a sudden onset of intense star formation. Similarly, C/E is best fit by a young stellar population with an age of 180 Myr and a short episode of SFH that has $\tau = 50$ Myr. However, its stellar mass is almost one magnitude lower at $5.4 \times 10^{9} M_{\odot}$.

5.1.3. *Decomposition in Mid-to-Far-IR*

We used the position priors in H_{160} for the decomposition. Not surprisingly, the automatically iterative fit in 24 μm converged on only B and D, the latter of which is by far the most dominant object in 24 μm. In 250 μm,

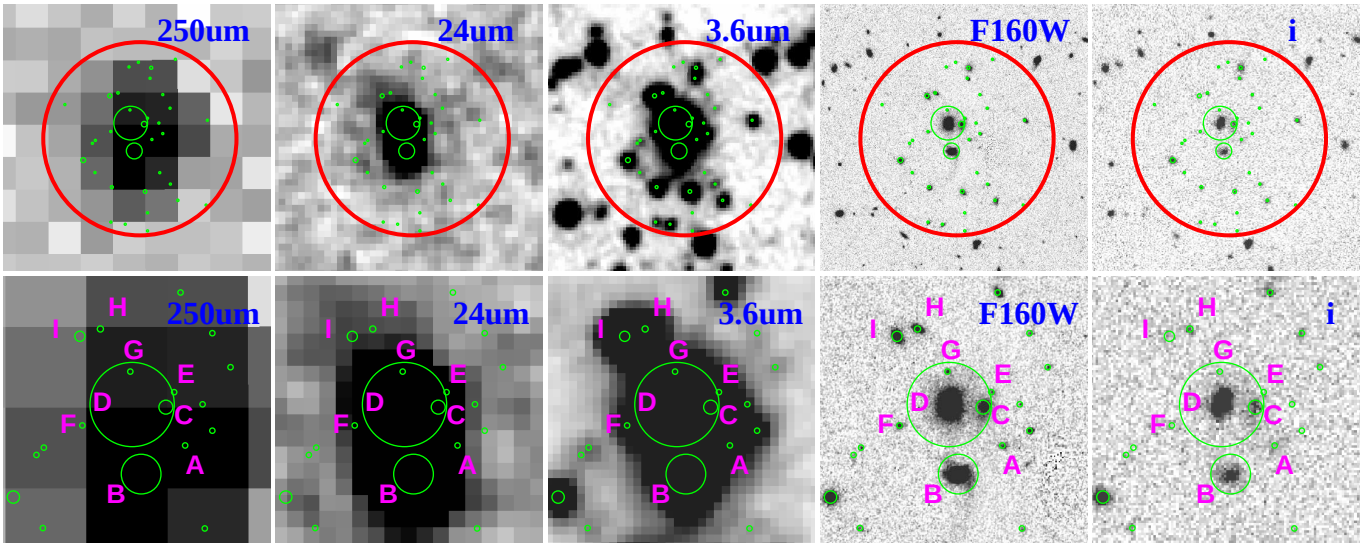

FIG. 12.— FIR to optical images of UDS01. The organization and the legends are the same as in Fig. 2. This source lacks 160, 100 and 70 μm data. The i-band image is from the CFHTLS-Wide program.

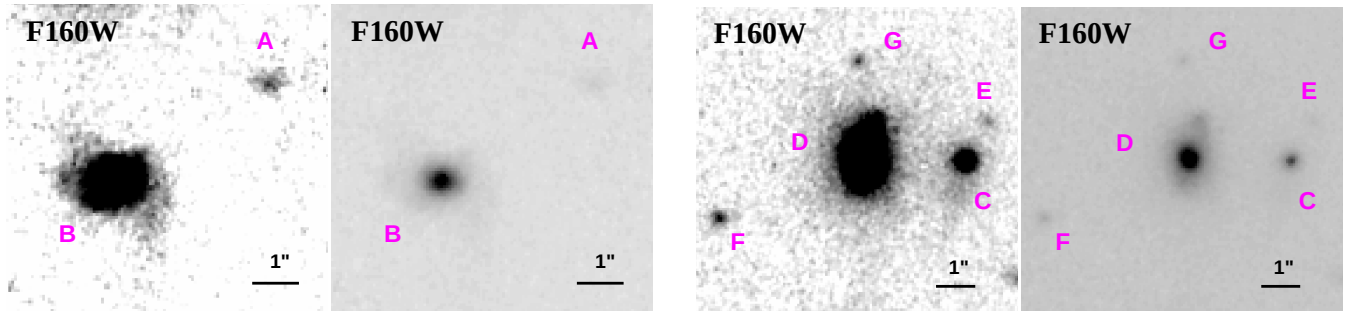

FIG. 13.— NIR morphologies of the possible contributors to UDS-01, shown in H_{160} with two contrast levels to reveal different features. The left panel is for the "southern" group that includes A and B, while the right panel is for the "northern" group that includes objects from C to F.

however, it settled on B and C with the resulted flux ratio of 55.5%:44.5%, and rejected D because of its negligible flux.

Although in the case of GOODSN63 we have learned that the strongest 24 μm source is not necessarily the major contributor to the FIR emission, it seems unusual that a FIR source would have no 24 μm counterpart. We thus checked for degeneracy using the trail-and-error method. This confirmed that indeed only B, C and D could be relevant. The results are summarized in Fig. 15. The forced fit with B and D left slightly larger residual than the automatically iterative result ("B+C"), however it is not unacceptable. Fitting with only C or D, on the other hand, left obvious residual at the location of B, clearly indicating that a reasonable solution must include B. Forcing the fit to include B, C and D produced the same result as the B+C case. Therefore, our decomposition slightly favors B and C as the contributors to the FIR emission, however we cannot definitely rule out the possibility that it actually is B and D that are responsible.

One would hope that the radio data from the 100 mJy VLA 1.5 GHz survey (Simpson et al. 2006) could break this degeneracy. Their catalog contains only one strong radio source in the area occupied by UDS01, with $S_{1.5GHz} = 0.185 \pm 0.030$ mJy. The radio position is $RA = 2^h18^m06^s.16$, $DEC = -5°12'45''.61$ (J2000), which is right on D (only offset by $0''.68$). While this VLA survey used the B and C configurations and thus have worse angular resolution than that of Morrison et al.'s data in the GOODS-N, its positional accuracy is still good to sub-arcsec level for the high S/N radio sources such as this one. For this reason, D seems to be a more plausible FIR contributor than C. However, it is puzzling that B, which is the strongest in 250 μm among all, does not have a radio counterpart in the catalog.

The flux densities of B and D, based on the decomposition results using the B+D case, are summarized in Table 2. The flux densities of B in the B+C case only differ by $< 6\%$.

5.1.4. *Total IR Emission and Stellar Populations*

None of the above components are in the SXDS X-ray catalog of Ueda et al. (2008), which has the sensitivity limit of 6×10^{-16} $erg/s/cm^2$ in its most sensitive 0.5–2 keV band. At $z \sim 1$, this corresponds to an upper limit of $\sim 3.2 \times 10^{42}$ erg/s in restframe 1–4 keV. While this cannot rule out the possibility of an AGN contamination, there is no strong evidence suggesting that there could be an AGN. Therefore, we take it that the FIR emission of UDS01 is all due to star formation.

Regardless of the exact counterparts, it is clear that the FIR emission is due to the interacting system that

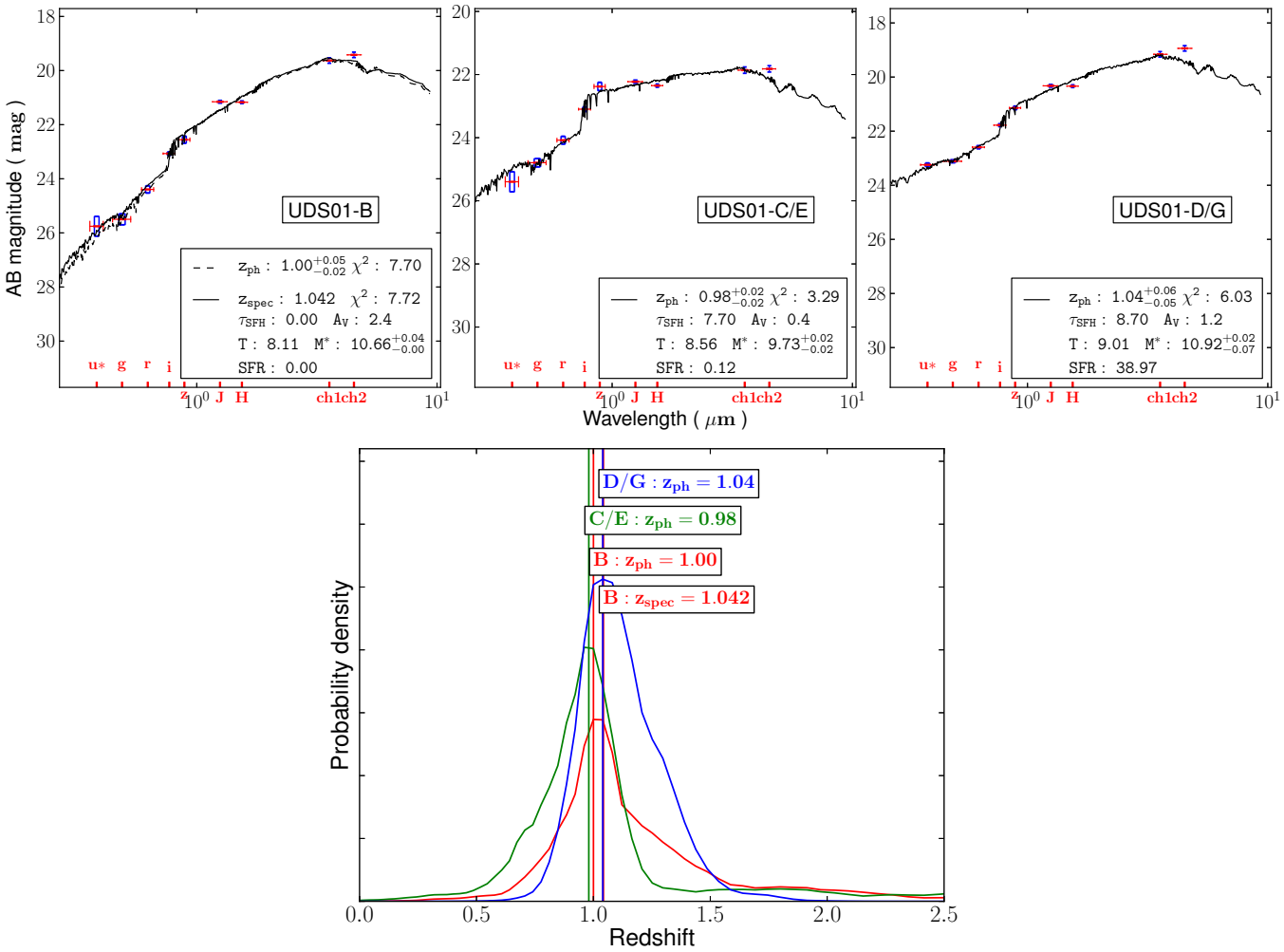

FIG. 14.— Optical-to-NIR SED analysis of the possible contributors to UDS01. Legends are the same as in Fig. 4. A is excluded here because it is not well detected in CFHTLS-Wide data. It is highly plausible C/E and D/G are at the same redshift as B, which has $z_{spec} = 1.042$.

includes B, C and D. To estimate L_{IR}, we adopted $z_{spec} = 1.042$ of B as their common redshift, and fit the decomposed 250 μm and 24 μm fluxes to the SK07 models. As we only had two data points, we did not apply scaling to the templates but simply read off the luminosities of the best-fit templates (Fig. 16). In the case of B+C, we obtained $L_{IR} = 1 \times 10^{12} L_\odot$ for B, and did not estimate for C because it only has one data point (250 μm). In the case of B+D, the best-fit template is the same for both objects, and is the same as in the previous case. This is shown in the upper panel in Fig. 16. It thus seems robust that B is an ULIRG with $L_{IR} = 1 \times 10^{12} L_\odot$. We calculated $L_{IR}^{ext} = 5.2 \times 10^{11} L_\odot$ and $L_{IR}^{blk} = 4.8 \times 10^{11} L_\odot$, which implies $SFR_{IR}^{blk} = 48\ M_\odot/yr$. The SED fitting in §5.1.2 shows that its exposed stellar population is an SSP and thus $SFR_{fit} = 0$. Therefore, we get $SFR_{tot} = 48\ M_\odot/yr$. In addition, D could also be an ULIRG of the same $L_{IR} = 1 \times 10^{12} L_\odot$. It has $L_{IR}^{ext} = 3.8 \times 10^{11} L_\odot$ and $L_{IR}^{blk} = 6.2 \times 10^{11} L_\odot$, which implies $SFR_{IR}^{blk} = 62\ M_\odot/yr$. Its exposed region has $SFR_{fit} = 39\ M_\odot/yr$, and thus the whole system of D has $SFR_{tot} = 101\ M_\odot/yr$.

As all the possible counterparts could be at the same redshift, we also considered the case where they were combined. In this case, we used the reported 350 and 500 μm flux densities for UDS01 as a whole without doing decomposition. The fit, as shown in the lower panel of Fig. 16, gives $L_{IR} = 2.0 \times 10^{12} L_\odot$, exactly the value if we were to combine the luminosities obtained in the case of B+D for the two objects individually.

The stellar mass of B obtained in §5.1.2 is $4.6 \times 10^{10} M_\odot$, and therefore it has $SSFR = 1.0$ Gyr^{-1}, $T_{db}^{tot} = T_{db}^{blk} = 1.0$ Gyr. This is a factor of 7.7 longer than the age (129 Myr) of the stellar population in the exposed region and is also much longer than the typical lifetime of an ULIRG. The stellar mass of D is $8.3 \times 10^{10} M_\odot$, and therefore in the B+D case it has $SSFR_{IR} = 1.2$ Gyr^{-1}, $T_{db}^{tot} = 822$ Myr and $T_{db}^{blk} = 1.3$ Gyr. The latter is comparable to $T = 1.0$ Gyr of the stellar population in the exposed region, however is much longer than the typical lifetime of an ULIRG. We also derived $T_d^{fit} = 39.2$ K and $M_d = 5.0 \times 10^8 M_\odot$ for the whole, combined system. The latter implies the total gas mass of $M_{gas} = 7.0 \times 10^{10} M_\odot$, which would be sufficient to fuel B to double its mass but would fall short for D. Overall speaking, the ULIRG phase of this whole system will only play a minor role in assembling its stellar mass.

We can check on the FIR-radio relation for D, assuming

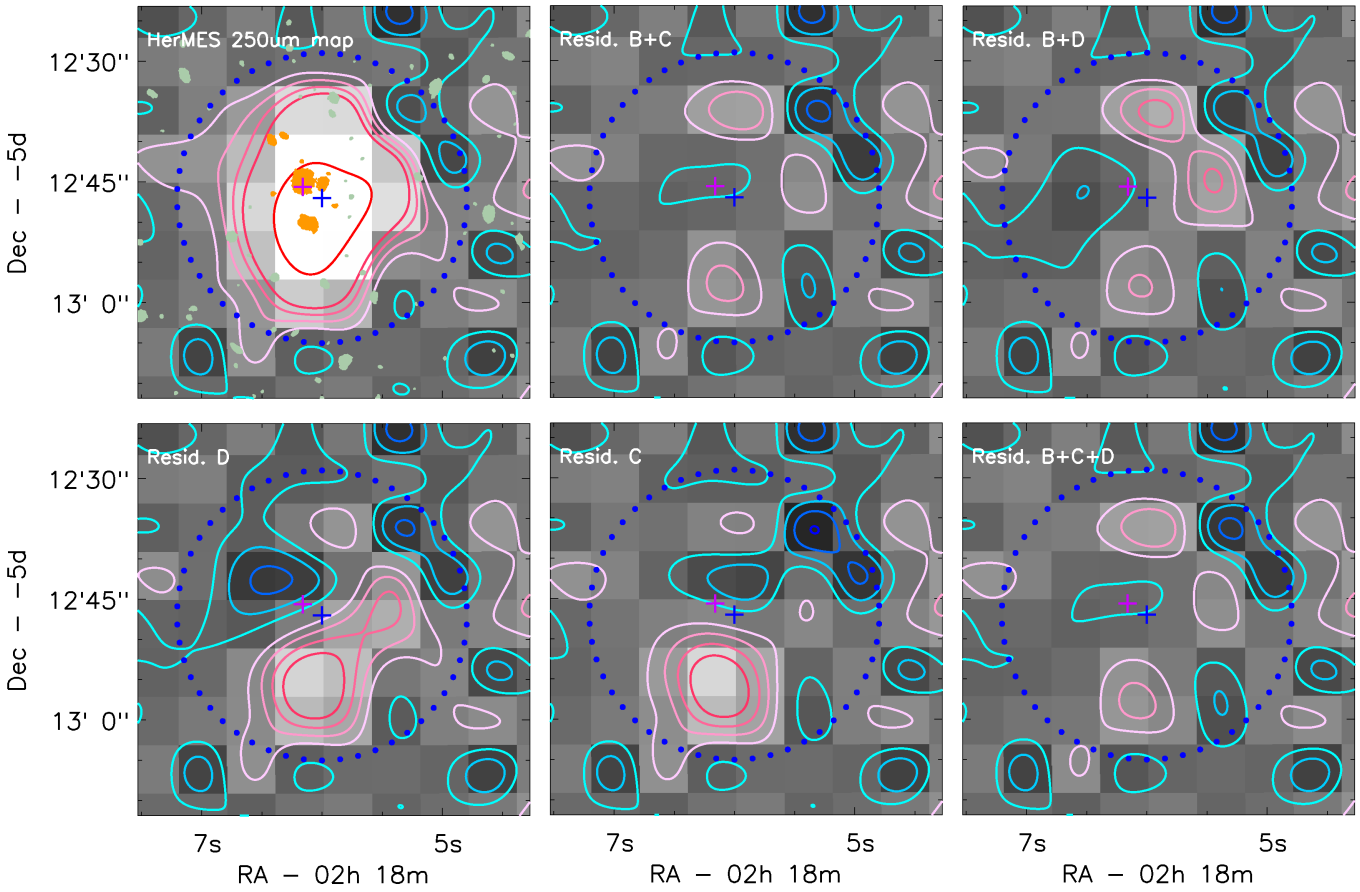

FIG. 15.— Demonstration of the decomposition in 250 μm for UDS01. The first panel shows the original 250 μm image, while the others show the residual maps of the different decomposition schemes where different input sources are considered (labeled on top). Legends are the same as in Fig. 5. This is a degenerate case. While automatically iterative fit settles on `B+C`, the trial-and-error run using `B+D` still produces satisfactory results. However, the fit without the inclusion of `B` are not acceptable.

that the real solution is the `B+D` case. We obtained $q_{IR} = 2.00$, significantly lower than the mean of 2.40 ± 0.24. There is no radio source in the catalog of Simpson et al. (2006) that corresponds to `B`. We can place an upper limit of 0.1 mJy at 1.5 GHz, which is the flux density limit of this catalog. This would then result in $q_{IR} < 1.91$ for `B`.

5.2. *UDS04 (UDS-J021731.1-050711)*

This source does not have WFC3 IR data because it is outside of the CANDELS WFC3 footprint. Therefore, we used UKIRT $JHKs$ data for the SED analysis in the near-IR. Fortunately, it has CANDELS ACS data for morphological information.

5.2.1. *Morphologies and Potential Components*

Fig. 17 shows the image of UDS04. the UKIDSS H, and the ACS I_{814}. We searched for its potential components in the I_{814} image, and found 50 objects within $18''$ to the 250 μm position that have $S/N > 5$ in I_{814} and $S/N > 3$ in V_{606}. The extra detection criterion in V_{606} is to reject any cosmic-ray and image defect residuals.

From Fig. 17, it is obvious that UDS04 corresponds to only two possible sources in 24 μm. The more dominant one, which coincides better with the UDS04 centroid, is actually made of eight tightly packed objects detected in I_{814}. The detail of this region is shown in the bottom-left panel of Fig. 17, and it is clear that these eight objects are actually the result of a very disturbed system being resolved. From its morphology alone, it is consistent with being a disc system undergoing a violent disk instability (VDI; e.g., Dekel et al. 2009). We designate this system as object `A`. As it turns out, it has spectroscopic redshift of $z = 1.267$ (Simpson et al. 2006; Akiyama et al., in prep.). The other 24 μm source is much further away from the 250 μm centroid, and is made of three I_{814} objects. The I_{814}-band image shows that they are actually a normal spiral galaxy and two bright knots on its arms. We designate this spiral as `B`. This source does not have spectroscopic redshift.

5.2.2. *Optical-to-near-IR SED Analysis*

For the optical part of the SED, we only used the CFHTLS-Wide u^*griz data as in §5.1 but did not include the ACS V_{606} and I_{814} data because the ACS images break `A` and `B` into subcomponents and are not straightforward to obtain the total light. On the other hand, `A` and `B` are detected as single objects in the CFHTLS-Wide images, which is more appropriate in this context. As both objects lack WFC3 IR data, the UKIDSS data were used for the near-IR part of the SED. We carried out the photometry on the UKIDSS DR8 images, using K_s-band as the detection band. Following the case in optical, we used `MAG_ISO` for colors and then used the K_s-band `MAG_AUTO` magnitude for normalization. In the longer wavelengths, we used the same IRAC data as in §5.1.

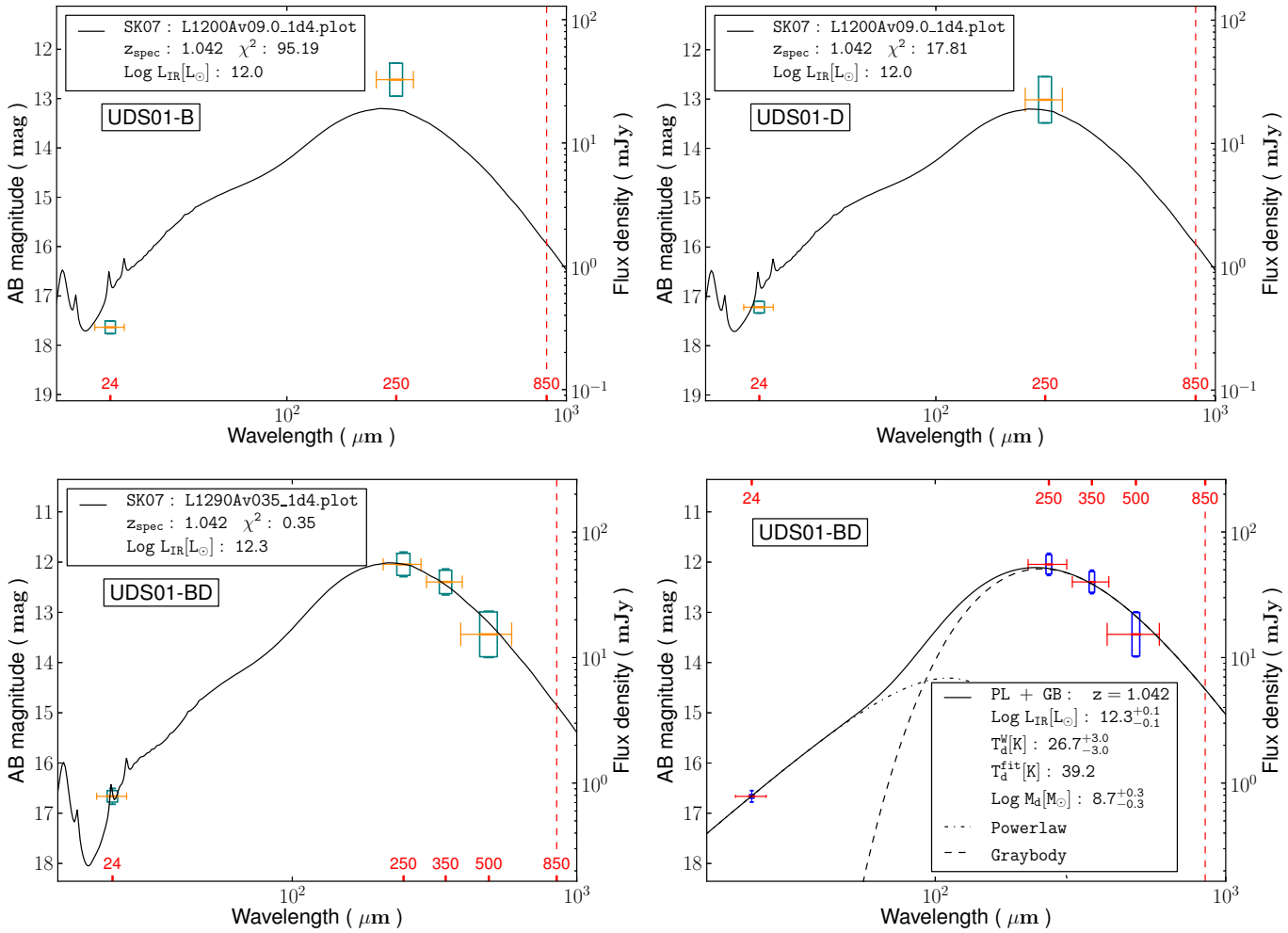

FIG. 16.— Mid-to-FIR SED fitting for UDS01 at $z = 1.042$. Legends are the same as in Fig. 6. The two figures on the top show the fits to the SK07 models in the case where B and D are the counterparts. No scaling is applied because there are only two data points available (see text). In the degenerate case where B and C are the counterparts, the result for B is exactly the same as shown here, however it is impossible to solve for C as it has only one data point available (lacking 24 μm). The two figures on the bottom row show the fitting results when this system is treated as a whole such that the 350 and 500 μm data can also be used without doing decomposition: the one to the left is the fit to the SK07 models, while the one to the right is the fit to the power-law + graybody models.

The SED fitting results are summarized in Fig. 18. For A, we derived $z_{ph} = 1.32$, which is in good agreement with its $z_{spec} = 1.267$ ($\Delta z/(1+z) = 0.02$). Fixing the redshift at its z_{spec}, the stellar mass thus derived is $1.0 \times 10^{11} M_\odot$. The best-fit stellar population has $\tau = 79.4$ Myr and the age of $T = 182$ Myr. It also gives $SFR_{fit} = 208 M_\odot/yr$. Therefore, the whole life of this young galaxy up to this point has been in an intense star-bursting phase.

For B we get $z_{ph} = 0.68$. Thus B cannot be associated with A.

5.2.3. *Decomposition in Mid-to-Far-IR*

While aperture photometry would be sufficient in 24 μm, we still performed the same PSF fitting technique to derive the fluxes for A and B. As both objects are resolved into multiple components in the ACS data, we used their centroids as measured in the CFHTLS-Wide data to avoid any ambiguity. The automatically iterative decomposition in 250 μm shows that the contribution from B is negligible and that A should be the only source responsible for the FIR emission. Thus we adopted the results from the HerMES DR1 catalog for the three SPIRE bands. Table 2 lists these results.

5.2.4. *Total IR Emission and Stellar Populations*

UDS04 is not detected in the SXDS X-ray data (Ueda et al. 2008). At $z = 1.267$, the sensitivity limit of this catalog corresponds to an upper limit of 5.8×10^{42} erg/s in restframe 1.1–4.5 keV. Based on the same argument as in §5.1.4, we take it that the FIR emission of UDS04, which is all from A, is all due to star formation. The mid-to-far-IR SED fitting results are summarized in Fig. 19. Similar to the case in GOODSN63 where there is only one contributor to the FIR emission, we incorporated the SPIRE 350 and 500 μm photometry taken directly from the HerMES DR1 catalog. Using the SK07 templates, we obtained $L_{IR} = 5.0 \times 10^{12} L_\odot$ and thus it is an ULIRG. From the result in §5.2.2, we also obtained $L_{IR}^{ext} = 2.55 \times 10^{12} L_\odot$. Therefore, $L_{IR}^{blk} = 2.55 \times 10^{12} L_\odot$ and $SFR_{IR}^{blk} = 255\ M_\odot/yr$. It has $SFR_{fit} = 208\ M_\odot/yr$, and thus $SFR_{tot} = 463\ M_\odot/yr$. As derived in §5.2.2, the exposed region has the stellar mass of $1.0 \times 10^{11} M_\odot$, which leads to $SSFR = 4.6 Gyr^{-1}$, $T_{db}^{tot} = 216$ Myr and $T_{db}^{blk} = 392$ Myr. The exposed region has the best-fit age

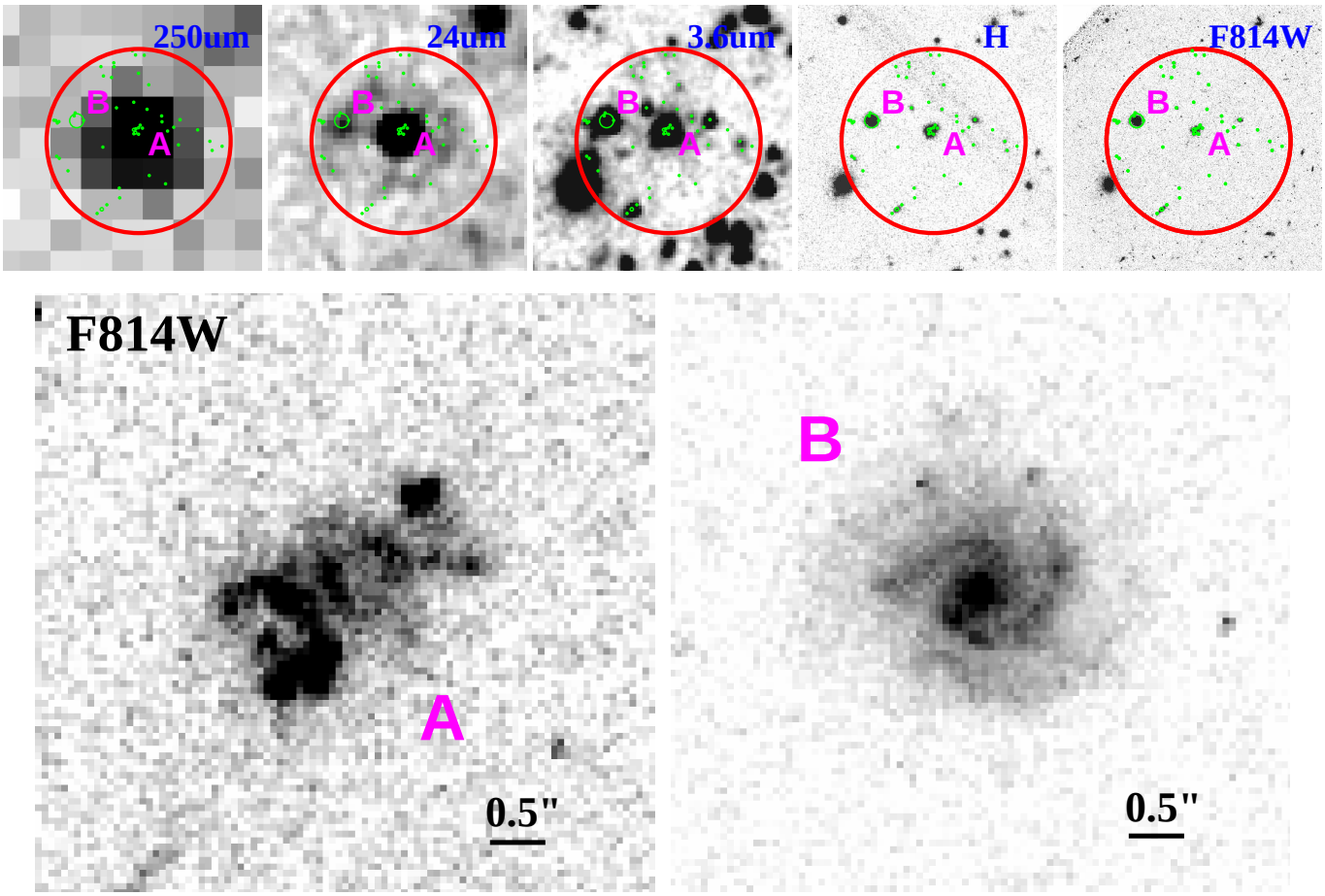

FIG. 17.— FIR to optical images of UDS04 are shown in the top row. The legends are the same as in Fig. 2. As there are only two potential contributors (A and B) to the FIR emission, no zoomed-in view of their vicinity is shown. This source lacks 160, 100 and 70 μm data. The H-band image is from UKIDSS. The morphological details of A and B as revealed by the ACS I_{814} image are shown in the bottom panel.

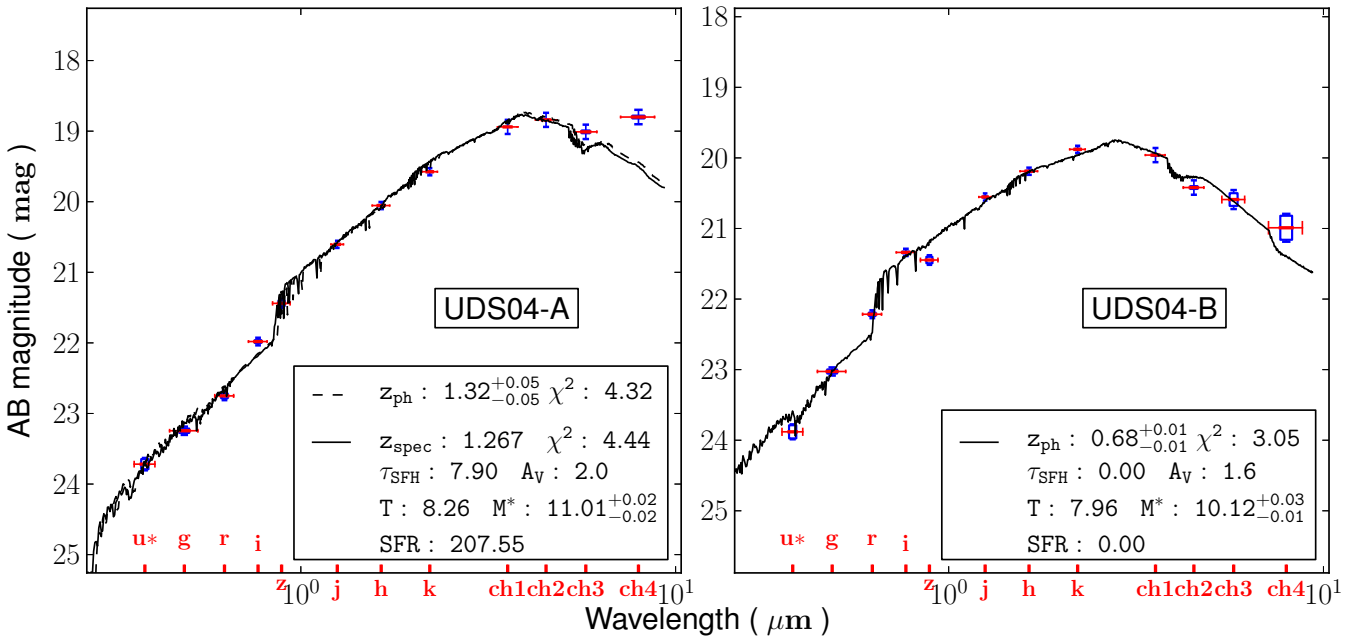

FIG. 18.— Optical-to-NIR SED analysis of the possible contributors to UDS04. Legends are the same as in Fig. 4. B is unlikely to be at the same redshift as A.

$T = 182$ Myr and the declining time scale $\tau = 79$ Myr. In this sense, UDS04-A is similar to GOODSN06-A: this young system is in a star-bursting phase ever since its birth, and while the star formation in the exposed region is quickly winding down, it is still sustained in the dust-blocked region. As shown in the right panel of Fig. 19, we derived $T_d^{fit} = 38.2$ K and $M_d = 1.0 \times 10^9 M_\odot$. The latter implies $M_{gas} = 1.4 \times 10^{11} M_\odot$, which would be sufficient to fuel the dust-blocked region for the next 550 Myr to more than double the stellar mass.

A is detected in the 100 μJy 1.5 GHz data (Simpson et al. 2006), whose radio location is at $RA = 2^h17^m31^s.17$, $DEC = -5°07'09''.35$ (J2000) and is only $0''.26$ away from the centroid of A. It has $S_{1.5GHz} = 1.055 \pm 0.013$ mJy and is the strongest radio source in our sample. We derived $q_{IR} = 1.74$, which is much lower than 2.40 ± 0.24.

6. SOURCES IN THE EGS

As mentioned in §2, the EGS field has both the HerMES SPIRE and PEP PACS data. For the latter, we use the PEP DR1 "blind" (i.e., constructed without using the positions priors from the MIPS 24 μm data) 100 μm and 160 μm catalogs. When this work started, the CANDELS WFC3 observations in this field was not yet finished, and none of the sources in this field had WFC3 data. Therefore, we relied on the ACS V_{606} and I_{814} images from the AEGIS program to study their morphologies. To define the possible components, on the other hand, we used the CFHTLS-Deep u^*griz images. We made this choice because the CFHTLS-Deep data are significantly deeper than the AEGIS ACS images. The CANDELS WFC3 data have just become available, and they are incorporated in the SED analysis. The possible contributors to the FIR sources remain unchanged.

6.1. *EGS07 (EGS-J141900.3+524948)*

6.1.1. *Morphologies and Potential Components*

Fig. 20 shows the images of EGS07. Within $18''$ of the 250 μm source centroid, there are 55 objects detected in the CFHTLS Deep data that have $S/N \geq 5$ in the i-band (measured in the MAG_ISO aperture). Our inspection identified 8 objects as the potential contributors to the 250 μm flux, which we label as object "1" to "8" in increasing order of the distance to the 250 μm source centroid. To emphasize the choice of the ground-based images for the counterpart identification, the labeling scheme here is numerical instead of alphabetical. In 24 μm image, these objects are all blended together as one single source and cannot be separated. This is also true in the 100 and 160 μm images.

The central source, 1, has spectroscopic redshift of $z = 1.497$ from the DEEP2 galaxy redshift survey (Newman et al. 2013). In the ACS images, this source shows a very disturbed morphology that is indicative of strong interaction. This suggests that it could be the dominant contributor. Running SExtractor on the I_{814} image, this source is broken into five components extending over $\sim 4.0''$, for which we label as 1-a to 1-e (see Fig. 21). The component 1-e is compact and consistent with being point-like, and the other are all diffuse and irregular in shape. While they cannot be separated by SExtractor on the CFHTLS Deep images, most of these components are still visually discernible in these images with the exception that 1-e is swamped by 1-a due to the coarser spatial resolution and thus cannot be separated. As the CFHTLS data are deeper than the ACS images, 1-b is better detected (so is 2). The centroids of the 250 and 160 μm images are between 1-a, 1-d and 1-e, while the 100 μm centroid is $\sim 2''.5$ to the north.

Other objects do not have obvious features. 4, 5 and 8 are compact and point-like, while 2, 3, 6, and 7 are extended.

6.1.2. *Optical-to-near-IR SED Analysis*

The optical-to-near-IR SED were constructed using the CFHTLS-Deep u^*griz and the CANDELS WFC3 J_{125} and H_{160} data, following the same procedures as in §5.1.2. The AEGIS ACS data were not used for this purpose because they are not as deep as the CFHTLS data. Unfortunately, the TFIT procedure using the WFC3 H_{160} does not produce satisfactory results in IRAC (with bad residual maps) due to some unknown reasons, and therefore we had to exclude the IRAC data in this analysis.

The results are summarized in Fig. 22. Object 1 has $z_{ph} = 1.46$, which agrees with its $z_{spec} = 1.497$ very well ($\Delta z/(1+z) = 0.01$). Object 6 has $z_{ph} = 1.48$, and from the $P(z)$ distribution it seems very likely that it is at the same redshift as 1. They are $3''.4$ apart, corresponding to 28.9 kpc, and hence could be in the same group. Their physical properties are rather different, however. 1 has a high stellar mass of $6.9 \times 10^{10} M_\odot$, a moderate age of 724 Myr, and an extended SFH with $\tau = 7$ Gyr (i.e., almost constantly star forming as compared to its age). The inferred current SFR is 137 $M_\odot/yr$. 6, on the other hand, is significantly less massive ($M^* = 8.3 \times 10^9 M_\odot$) and much younger ($T = 182$ Myr), and has assembled most of its current stellar mass through a short, modest episode of star formation ($\tau = 60$ Myr) that leaves the current SFR of $\sim 10 M_\odot/yr$.

Another possible group consists of objects 2, 4, 5, and 8, which have $z_{ph} = 1.01 \pm 0.07$. In terms of stellar mass, this group is not significant, as the most massive one, 5, has only $M^* = 3.2 \times 10^9 M_\odot$.

Object 3 and 7 have $z_{ph} = 1.23$ and 1.89, respectively, and thus are unlikely associated with either of the two possible groups.

6.1.3. *Decomposition in Mid-to-Far-IR*

In 24 μm, the automatically iterative fit settled on objects 1, 2 and 3. These three objects account for $\sim 61\%$, 32% and 6% of the total flux, respectively. For 70 μm, it converged on only 1, although this leaves visible residual. In 100 μm, 1 was still the dominant component and account for $\sim 67\%$ of the total flux, however the secondary components changed to 4 and 6, which are responsible for 15% and 17% of the total flux, respectively. In 160 μm, the automatically iterative fit failed, and we had to use the trial-and-error method. The only sensible results were obtained when the fit used 1 and 4 or just 1, and we adopted the former case because 4 seems to be non-negligible in 100 μm, although this reason is not overwhelming. The flux density of 1 would increase by $\sim 10\%$ if we were to choose otherwise. Similarly, we had to use the trial-and-error approach to fit 250 μm, and the only sensible results were obtained when using 1 and 4 or just 1, and we again adopted the former case. If we were

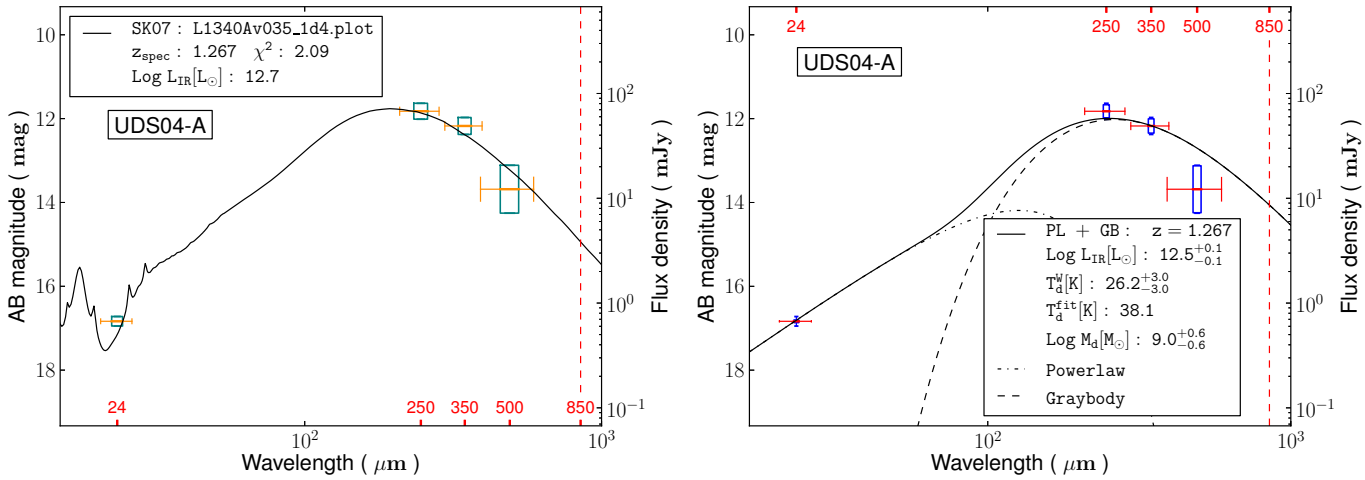

FIG. 19.— Mid-to-FIR SED fitting for UDS04-A at $z_{spec} = 1.267$. The SED incorporates the SPIRE 350 and 500 μm photometry directly from the HerMES catalog because A is the sole contributor at 250 μm and longer wavelengths and hence no decomposition in these two bands are necessary. The left panel shows the fit to the SK07 models, and the right panel shows the fit using the power-law + graybody models. Legends are the same as in Fig. 6.

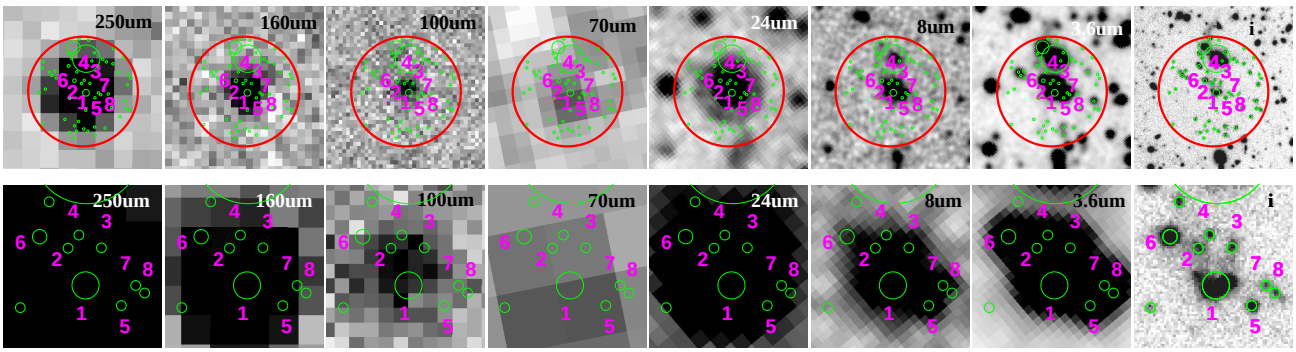

FIG. 20.— FIR to optical images of EGS07. The legends and the organization of the panels are the same as in Fig. 2. The i-band image is from CFHTLS-Deep.

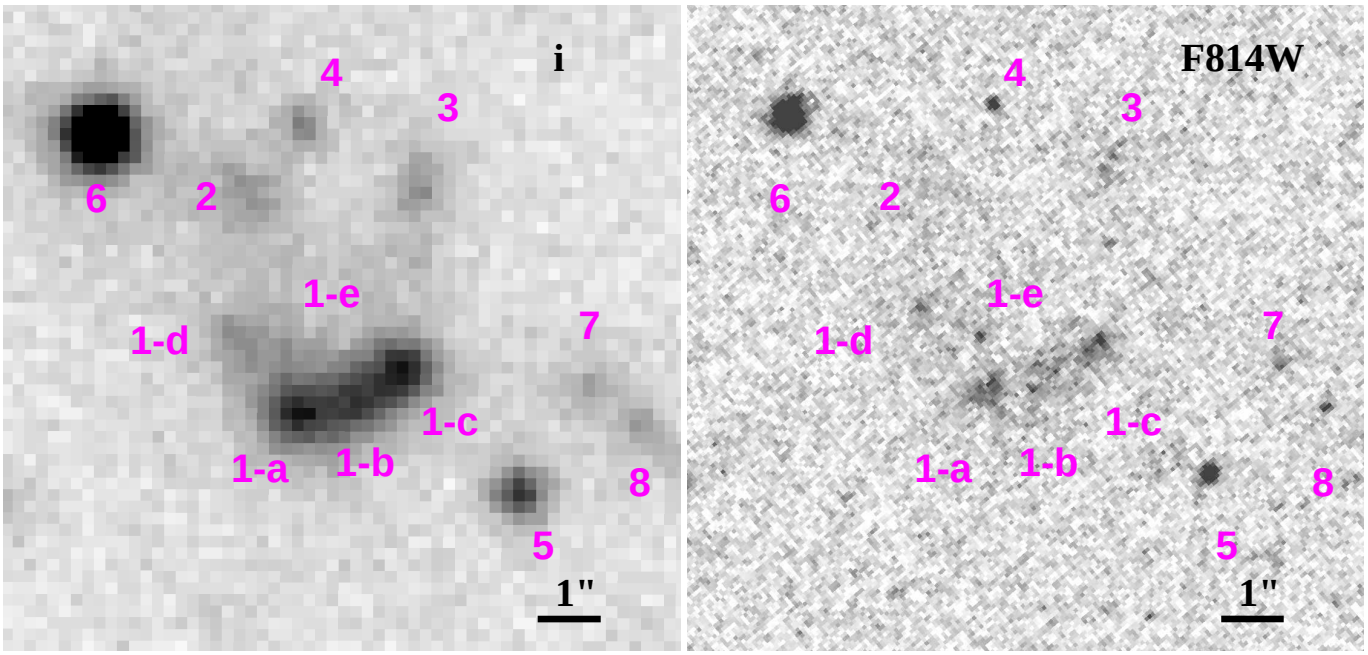

FIG. 21.— Morphological details of the potential contributors to EGS07. The left panel is the i-band image from the CFHTLS-Deep program, while the right panel is the I_{814}-band image from the AEGIS ACS program. The CFHTLS images are deeper that the ACS images, but the latter show more morphological details.

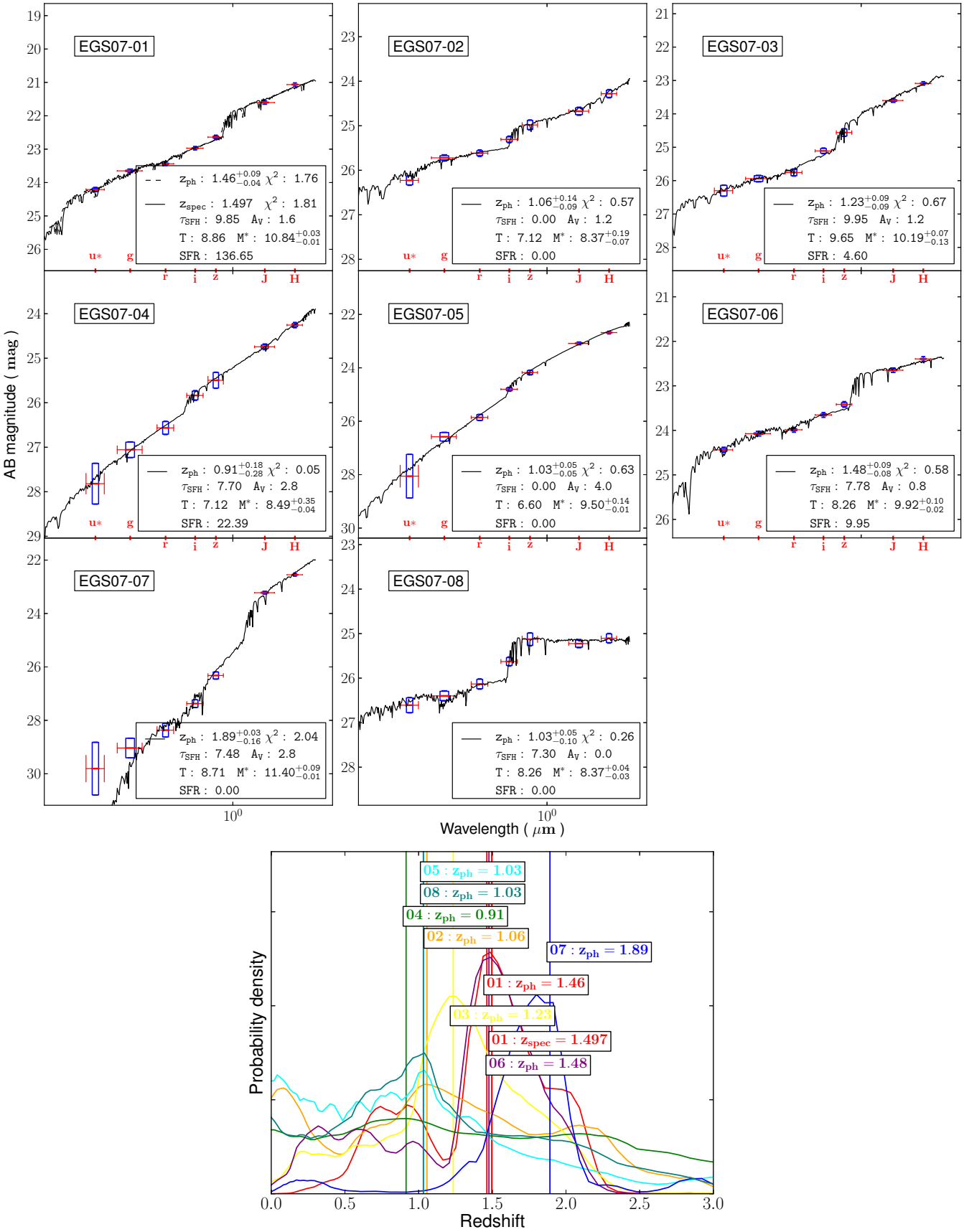

FIG. 22.— Optical-to-NIR SED analysis of the possible contributors to EGS07. Legends are the same as in Fig. 4. Objects 1 and 6 are likely at the same redshift. Another possible group consists of 2, 4, 5, and 8 at $z_{ph} = 1.01$.

to chose otherwise, the flux density of 1 would increase by 24%. The decomposition in 250 μm in demonstrated in Fig. 23. Regardless of the exact counterparts in each band, it is obvious that 1 is the dominant contributor to the mid-to-far-IR emission. The flux densities of this object are summarized in Table 2.

6.1.4. *Total IR Emission and Stellar Populations*

Fig. 24 summarizes the analysis of the FIR emission of EGS07-1. As it turns out, the SK07 models can provide a good fit from 70 μm to 250 μm, but the 24 μm data point cannot be satisfactorily explained (left panel of Fig. 24). Nevertheless, the derived $L_{IR} = 4.0 \times 10^{12} L_{\odot}$ agrees reasonably well with $L_{IR} = 5.0 \times 10^{12} L_{\odot}$ inferred from the analytic fit (right panel), and hence it seems robust that this object is an ULIRG.

Object 1 has an X-ray counterpart in the 800 Ks AEGIS Chandra data (Nandra et al. in prep.; Laird et al. 2009) [15], with the full-band fluxes in 0.5–10 keV of $7.05^{+1.55}_{-1.37} \times 10^{-16}$ $erg/s/cm^2$. At $z = 1.497$, this implies a total X-ray luminosity in restframe 1.2–25 keV of 1.0×10^{43} erg/s, which is in the AGN regime. Thus the FIR emission of 1 might have an AGN contribution, which might be the reason that the 24 μm data point is not well fitted. Its X-ray position has a very good accuracy of $0\farcs56$, and is consistent with the sub-component 1-e. Among all the sub-components of 1, 1-e is unique in its point-like morphology and its absence from the V_{606}-band. This raises a possibility that 1-e might not be part of 1 but actually be a background quasar, which could be at $z \sim 5$ given its being a dropout from V_{606}. If true, its X-ray luminosity would be 4.9×10^{44} erg/s. However, the FIR emission of EGS07 would not be from 1-e alone, otherwise the SPIRE flux densities would peak at 500 μm instead of between 250 and 350 μm. Estimating the IR luminosity for 1-e only is hardly possible in this case, as 1-e is so close to other subcomponents that it cannot be decomposed in the FIR. Therefore, while it is clear that 1 has an AGN and that the AGN could contribute significantly to the FIR emission, the nature of object 1 remains inconclusive at this point. Taking L_{IR} at its face value, one would infer an upper limit of $SFR_{IR} = 400 M_{\odot}/yr$. We refrain from discussing the SFR of this system in the usual way.

Finally, we investigate the FIR-radio relation for this source. The catalog of Ivison et al. (2010) include a strong radio source at the position of 1-e, which has $S_{1.4GHz} = 0.316$ mJy. We obtained $q_{IR} = 2.02$, which is significantly lower than 2.40 ± 0.24.

6.2. *EGS14 (EGS-J142025.9+525935)*

6.2.1. *Morphologies and Potential Components*

Fig. 25 shows the images of EGS14. Within $18''$ of the 250 μm source centroid, there are 58 objects detected in i that have $S/N \geq 5$. Based on inspection, we identified 10 objects as potential contributors to the 250 μm flux, which we label as "1" to "10". In this area, only two sources are discernible in the 24 μm image, which seem to be dominated by 5 and 9, respectively. While it is difficult see from the 100 and 160 μm images, the PEP DR1 catalog identifies two sources in this area as well, and their positions are also consistent with 5 and 9, respectively. All this suggests that 5 and 9 are the major contributors to the 250 μm flux.

The ACS images reveal that both 5 and 9 have interesting morphologies (Fig. 26). They are $4\farcs39$ and $5\farcs67$ from the 250 μm centroid, respectively, and are on the opposite sides ($10\farcs0$ apart). 5 is a very disturbed, curvy and knotty system whose shape resembles a scorpion. 9 is also highly irregular, having a bright central core and at least two satellite features around it. Among other objects, 1, 4 and 8 are compact, and the rest are extended. 2 and 10 seem to be disc systems with dust lanes, 3 and 6 are amorphous, and 7 actually consists of one central core and two smaller objects on each side.

6.2.2. *Optical-to-near-IR SED Analysis*

None of these ten objects have spectroscopic redshifts, and we derived their z_{ph} in the usual way. The results are summarized in Fig. 27. The optical-to-near-IR SED are different from those in §6.1.2 in that we are able to incorporate the SEDS IRAC 3.6 and 4.5 μm data, as the TFIT procedure produces good results comparable to those in §4 and 5. Object 6 has to be excluded, as it is only significantly detected in r and i. This leaves nine objects in total. The fits to objects 1, 3 and 7 are poor, but these three sources are likely irrelevant to the FIR emission (see below in §6.2.3.). Most of these objects are likely at $z \approx 1$. In particular, objects 5 and 9 have their z_{ph} agrees extremely well, at 1.11 and 1.12, respectively. 2, 4 and 8 all have $\Delta z/(1+z) \leq 0.05$ with respect to 5 and 9, and the peaks of their $P(z)$ distributions coincide well with each other. This suggests that EGS14 could be in a rich group environment. Objects 5 and 9 are by far the most dominant members of this possible group. However, their stellar populations are distinctly different. 5 has a very high stellar mass of $3.0 \times 10^{11} M_{\odot}$ and an old age of 5.5 Gyr, comparable to the age of the universe at this redshift. It has a prolonged SFH with $\tau = 4.0$ Gyr, which is comparable to its age, and a modest on-going $SFR = 45.5 M_{\odot}/yr$. If 5 indeed is a merging system as its morphology suggests, its subcomponents must have been persistently and gradually assembling their stellar masses right after the Big Bang, at a nearly constant rate of $\sim 50 M_{\odot}/yr$ (combining over all its subcomponents). Using the conversion from SFR to UV luminosity as in Madau et al. (1998), one can see that the progenitor of this entire system would be quite readily visible by $z \approx 10$, with a total magnitude of $H_{AB} \approx 25.2$ if there were not much dust at such an early stage. 9, on the other hand, has a much lower stellar mass of $5.0 \times 10^{10} M_{\odot}$ and a young age of 129 Myr. Its SFH is an intense, short burst with $\tau = 40$ Myr, which still leaves an on-going $SFR = 72 M_{\odot}/yr$.

6.2.3. *Decomposition in Mid-to-Far-IR*

The decomposition is carried out for the nine objects using their centroids determined from the CFHTLS-Deep i-band.

The automatically iterative fit succeeded in the 24 μm and 250 μm, the latter of which is shown in Fig. 28 for demonstration. For the 24 μm, the fit converged on 2, 5,

[15] Object 5 also has an X-ray counterpart that has the full-band 0.5–10 keV fluxes of $12.78^{+1.95}_{-1.79} \times 10^{-16}$ $erg/s/cm^2$. However we do not discuss it further as it does not seem to be a significant contributor to the FIR flux.

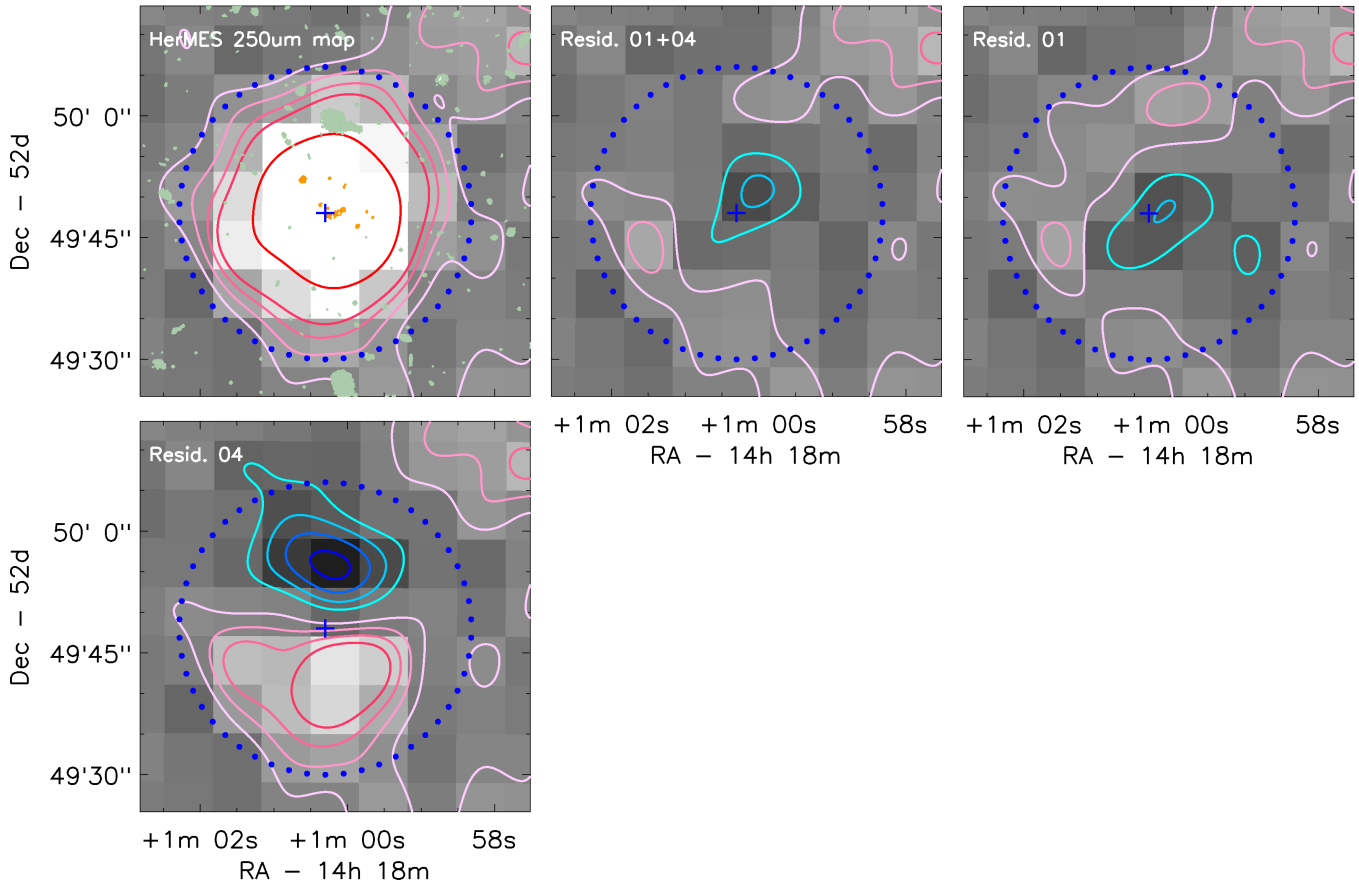

FIG. 23.— Demonstration of the decomposition in 250 μm for EGS07. The first panel shows the original 250 μm image, while the others show the residual maps of the different decomposition schemes where different input sources are considered (labeled on top). Legends are the same as in Fig. 5. The "1+4" case is adopted as the final solution. See text for details.

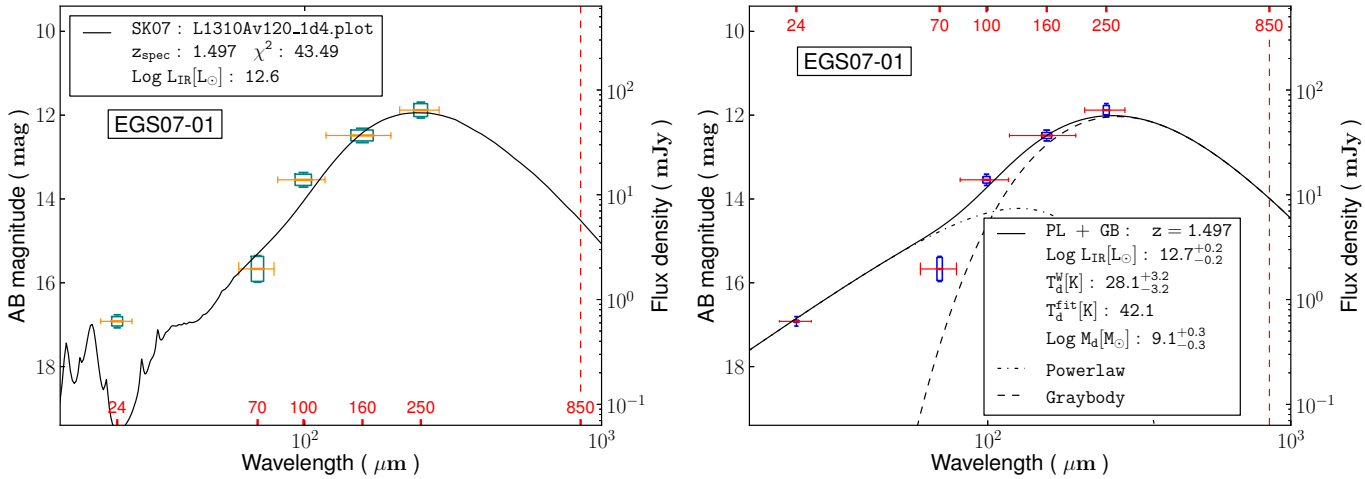

FIG. 24.— Mid-to-FIR SED analysis for EGS07. Legends are the same as Fig. 6. The 24 μm data point cannot be well explained by the best-fit SK07 models (left panel). Nevertheless, the derived L_{IR} is in good agreement with the result from the fit to the powerlaw + graybody models (right panel).

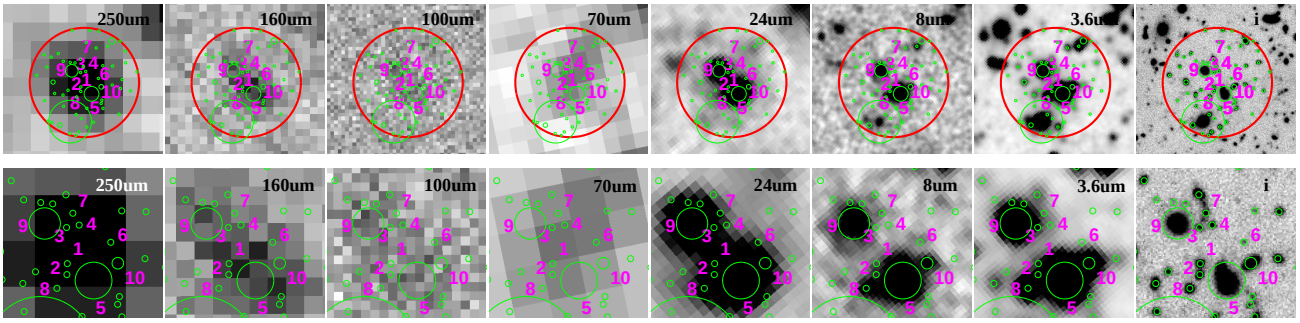

FIG. 25.— FIR to optical images of EGS14. The legends and the organization of the panels are the same as in Fig. 2. The *i*-band image is from CFHTLS-Deep.

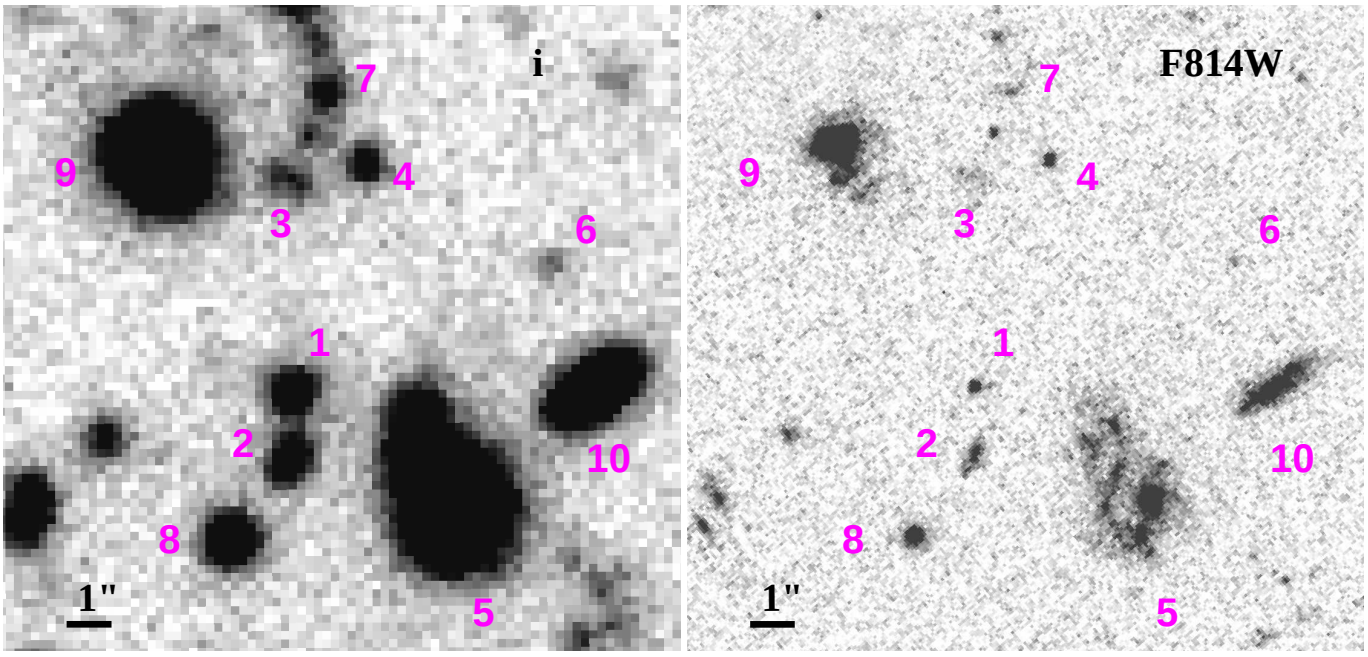

FIG. 26.— Morphological details of the potential contributors to EGS14 in *i*-band from CFHTLS-Deep (left) and in I_{814}-band from the AEGIS ACS (right).

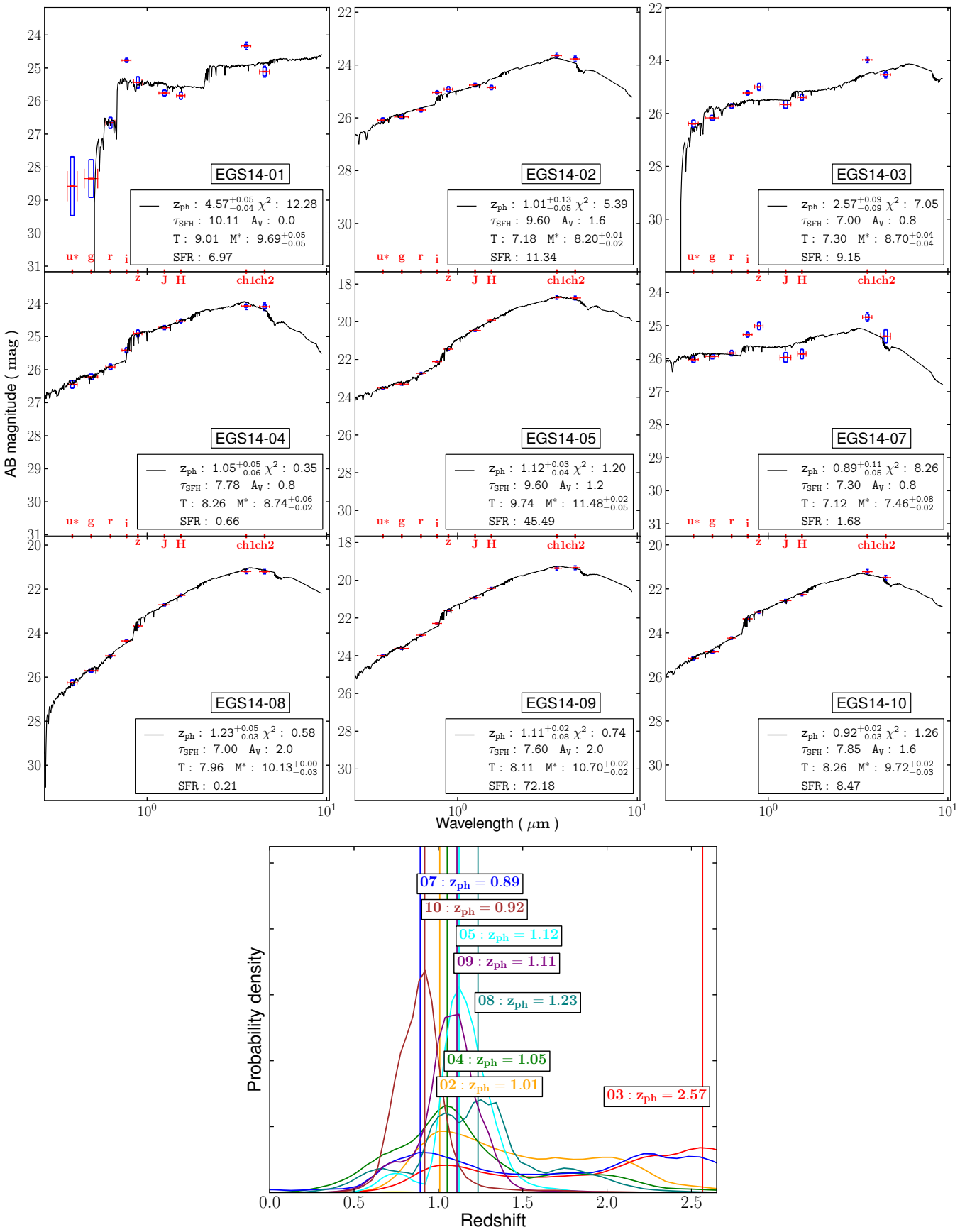

FIG. 27.— Optical-to-NIR SED fitting results for EGS14. Legends are the same as in Fig. 4. The two most massive objects, 5 and 9, are likely at the same redshift (z_{ph} = 1.11–1.12) and associated, at objects 2, 4 and 8 could also belong to this group.

9, and 10. Objects 5 and 9 almost equally split $\sim 82\%$ of the total light in this area. For the 250 μm, the fit converged on 5, 7, 8, 9, and 10. However 7, 8 and 10 were formally rejected because they all had negligible fluxes, and hence the output only included 5 and 9. Fitting only 5 or only 9 results in obvious residuals at the position of the other object, and hence is not acceptable.

Unfortunately, the decomposition in 70 μm using either the automatically iterative method or the trail-and-error method could not converge on any object, apparently because of the low S/N of the data. Therefore we had to skip this band. The decomposition in both 100 and 160 μm also failed due to the low S/N of the data. Nevertheless, the PEP DR1 catalog includes two sources whose position coincide with 5 and 9. As the decomposition of both the 24 μm and the 250 μm images shows that 5 and 9 are by far the most dominant objects in both bands, we adopted the PEP catalog values for these two objects in 100 and 160 μm and assumed that all other objects are negligible in these two bands. Table 2 summarizes these results for the major components 5 and 9.

6.2.4. *Total IR Emission and Stellar Populations*

The FIR emission of EGS14 should be mostly from 5 and 9. Based on their z_{ph} estimates, we adopted $z_{ph} = 1.12$ as their common redshift. Based on the AEGIS X-ray catalog, there is no X-ray source detected in the EGS14 region. The limit of this catalog in the most sensitive 0.5–2 keV band is $\sim 3\times10^{-17}\ erg/s/cm^2$, which corresponds to an upper limit of $2.1 \times 10^{41}\ erg/s$ in the restframe 1–4 keV at $z = 1.12$. Therefore, we believe that its FIR emission is most likely due to star formation. Fitting their mid-to-far-IR SED separately to the SK07 models, we got $L_{IR} = 1.3 \times 10^{12}$ and $1.0 \times 10^{12} L_\odot$ for 5 and 9, respectively, and therefore they are both ULIRG. This is shown in the left panels of Fig. 29. From the results in §6.2.2., we also got $L_I R^{ext} = 4.7 \times 10^{11} L_\odot$ for 5, which then implies $L_I R^{blk} = 8.3 \times 10^{11} L_\odot$ and $SFR_I R^{blk} = 83\ M_\odot/yr$ for this object. It has $SFR_{fit} = 46\ M_\odot/yr$, and hence we get $SFR_{tot} = 129\ M_\odot/yr$. For 9, we got $L_{IR}^{blk} = 1.2 \times 10^{12} L_\odot$, which is even slightly larger than L_{IR}. In this case, we take it that the observed IR emission can be fully explained by the extinction in the exposed region.

From the analytic fits, we got $T_d^{fit} = 36.9$ and $37.2\ K$, and $M_d = 4.0 \times 10^8$ and $3.2 \times 10^8 M_\odot$ for 5 and 9, respectively. All this suggests that the dust properties of these two ULIRGs are very similar. However, as discussed in §6.2.2, the stellar populations in the exposed regions of these two objects are vastly different in their stellar masses, ages and SFHs: 5 has $M^* = 3.0 \times 10^{11} M_\odot$, $T = 5.5$ Gyr and $\tau = 4.0$ Gyr, while 9 has $M^* = 5.0 \times 10^{10} M_\odot$, $T = 129$ Myr and $\tau = 129$ Myr. Therefore, these imply $SSFR = 0.4$ and $1.4\ \mathrm{Gyr}^{-1}$ for 5 and 9, respectively. For 5, one can also get $T_{db}^{tot} = 2.3$ Gyr and $T_{db}^{blk} = 3.6$ Gyr. For 9, $T_{db}^{tot} = 694$ Myr, and T_{db}^{blk} is not applicable. The inferred total gas masses for these two objects from the above dust masses are $5.6 \times 10^{10} M_\odot$ and $4.4 \times 10^{10} M_\odot$, respectively. Therefore, the gas reservoir for 5 would only allow it to add $< 20\%$ to its existing stellar mass even if it could turn all the available gas into stars. On the other hand, the situation for 9 is somewhat different in that its current ULIRG phase would be able to add $\sim 88\%$ to its existing stellar mass if it could turn all the gas into stars, however this would require a much longer time than the typical lifetime of an ULIRG. Considering that its on-going star formation is all in the exposed region and has a sharp declining SFH, this is not likely to happen.

Finally we investigate the FIR-radio correlation for EGS14. The catalog of Ivison et al. (2010) does not include any strong radio source in the area of EGS-14. However, from the radio map (Ivison, priv. comm.) we detect two moderate sources at the exact locations of 5 and 9, which have $S_{1.4GHz} = 0.043 \pm 0.012$ and 0.071 ± 0.013 mJy, respectively. From these we obtained $q_{IR} = 2.63$ and 2.34, respectively, which are consistent with the mean of 2.40 ± 0.24 in Ivison et al. (2010).

6.3. *EGS19 (EGS-J141943.4+525857)*

This source is different from the previous two in that it is outside of the CANDELS WFC3 area. At its 250 μm source location, the PEP catalog reports three sources. From north to south, their flux densities are 6.4 ± 1.2, 9.9 ± 1.2 and 6.0 ± 1.2 mJy in 100 μm, respectively, and 19.7 ± 3.3, 22.0 ± 3.4 and 17.1 ± 2.9 mJy, respectively.

6.3.1. *Morphologies*

Within $r = 18''$, there are 46 objects detected in the CFHTLS-Deep data that have $S/N \geq 5$ in the i-band measured in the MAG_ISO aperture. Among these objects, more than 20 of them could be possible contributors, most of which segregate into groups. The subcomponents within each group are so close to each other that using them directly for the decomposition would crash the process. Therefore, we took a slightly different approach in analyzing this source. To emphasize this difference, we use yet another different labeling scheme in referring to the possible counterparts. From the 24 μm image, we identified four possible contributors, which are labeled from $\mathbb{A}$ to $\mathbb{D}$. Each of these 24 μm sources could be made of several components as revealed by the CFHTLS Deep images, for which we label numerically as shown in Fig. 31 to 33.

Component $\mathbb{A}$ is made of six subcomponents. In the higher resolution ACS images, $\mathbb{A}-1$ seems like a dusty disk system viewed edge-on. $\mathbb{A}-2$, which is only $1\farcs56$ away from $\mathbb{A}-1$, is a small but resolved galaxy whose major axis is almost perpendicular to $\mathbb{A}-1$. $\mathbb{A}-3$ consists of two irregular objects separated by $0\farcs69$, which seem to be embedded in a somewhat extended halo. $\mathbb{A}-4$ is an irregular object with a small core. $\mathbb{A}-5$ consists of two objects separated by $0\farcs67$, one resolved and the other unresolved. $\mathbb{A}-6$ is irregular and does not have a well defined core.

Component $\mathbb{B}$ consists of four possible subcomponents. As revealed by the ACS images, $\mathbb{B}-1$, which is closest to the 24 μm source centroid, is made of three irregular objects [16] that stretch over $\sim 1''$. While currently we do not have any additional data to determine if these three objects are at the same redshift, we assume that they are associated and take them as one single object. $\mathbb{B}-2$ and $\mathbb{B}-3$ are two small, compact objects that are $2\farcs3$ and $4\farcs7$ away from $\mathbb{B}-1$, respectively. $\mathbb{B}-4$ is a regular

[16] The additional, compact "object" to the south-west is actually due to bad pixels.

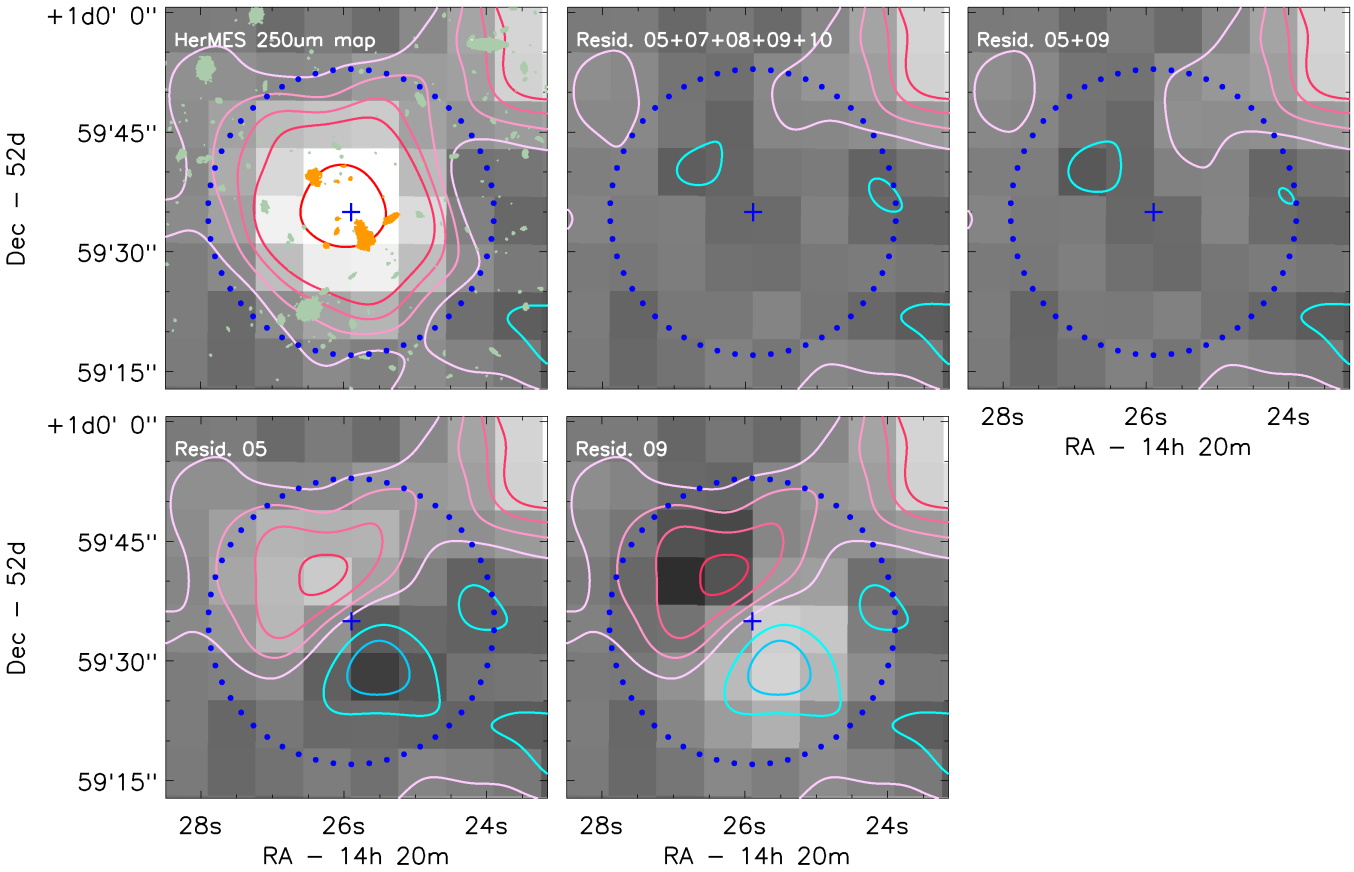

FIG. 28.— Demonstration of the decomposition of EGS14 in 250 μm. The first panel shows the original 250 μm image, while the others show the residual maps of the different decomposition schemes where different input sources are considered (labeled on top). Legends are the same as in Fig. 5. The "5+9" case is the adopted final solution.

spheroidal. While it is the brightest in optical among all, it is far away from the 24 μm source center ($\sim 4''$) and likely only contributes a minimal amount to the 24 μm flux.

Component $\mathbb{C}$ consists of two objects. $\mathbb{C}-1$ seems to be a regular elliptical in the CFHTLS images, however the ACS images reveal that it is most likely a merger. It has spectroscopic redshift of 1.180 from the Deep3 program. $\mathbb{C}-2$ is $1\farcs9$ away, and is a point source.

Component $\mathbb{D}$, which is $6\farcs1$ away from $\mathbb{C}-1$, is blended with $\mathbb{C}$ in 24 μm. The CFHTLS images show that it is made of two subcomponents separated by $\sim 0\farcs5$. The surface brightness of $\mathbb{D}$ is quite low, and it is not detected in the AEGIS images.

6.3.2. *Optical SED Analysis and Redshifts*

To proceed with our analysis, the first step is to determine if the subcomponents in each of the four 24 μm clumps could be at the same redshifts. As EGS-19 does not have WFC3 images to be used as the morphological templates, we refrained from doing TFIT of the IRAC image. Therefore, we only rely on the optical images from the CFHTLS Deep program to carry out the SED analysis. The photometry of the CFHTLS-Deep data was done in the same way as described in the previous sections.

The SED fitting results are summarized in Fig. 34 for $\mathbb{A}$ and in Fig. 35 for $\mathbb{B}$, $\mathbb{C}$ and $\mathbb{D}$. From the best-fit models and the $P(z)$ distributions, we concluded that $\mathbb{A}-1$, 2 and 4 could be at the same redshift and associated. Taking the average, we adopted $z_{ph} = 1.06 \pm 0.07$ as their common redshift. For the decomposition purpose below, we took the geometric center of these three objects as the common center of the system, and denoted this new "object" as $\mathtt{A}'$. Our assumption is that $\mathtt{A}'$ is the part from the $\mathbb{A}$ clump that have significant FIR contribution, and that all other components in this clump can be ignored. Similarly, $\mathbb{B}-1$, 2 and 3 could be at the same redshift of $z_{ph} = 2.72 \pm 0.07$ and associated, and the new "object" at their geometric center is denoted as $\mathtt{B}'$. The situation for $\mathbb{C}-1$ and 2 is somewhat uncertain because their z_{ph} differ significantly. However, since the $P(z)$ distribution for $\mathbb{C}-2$ has a wide, flat peak that contains the sharp $P(z)$ peak of $\mathbb{C}-1$, it is reasonable to assume that they are actually associated. Therefore we adopt the best-fit $z_{ph} = 1.08$ for $\mathbb{C}-1$ as the common redshift for this system, which is denoted as $\mathtt{C}'$ and assigned the position at the geometric center. This also suggests that $\mathtt{C}'$ could be with the same group as $\mathtt{A}'$, however it is not appropriate to combine the two for the decomposition as their separation is too large. Finally, we note that the single object $\mathbb{D}$ might be within the same group as $\mathtt{B}'$, however this is highly uncertain due to the lack of prominent peaks in its $P(z)$ distribution.

6.3.3. *Decomposition in Mid-to-Far-IR*

The decomposition was done at the locations of $\mathtt{A}'$, $\mathtt{B}'$, $\mathtt{C}'$, and $\mathbb{D}$. At 24 μm, the automatically iterative de-

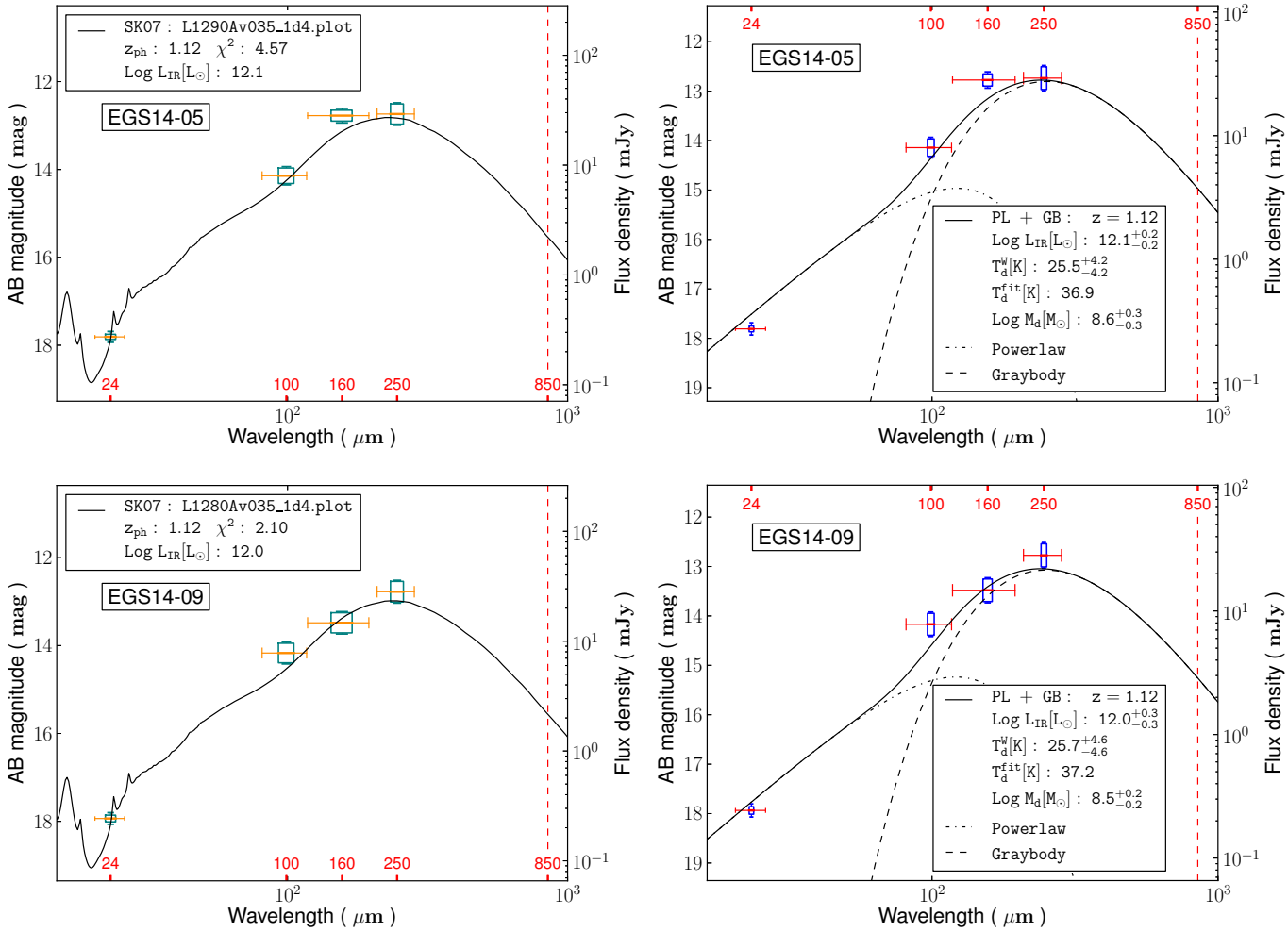

FIG. 29.— Mid-to-FIR SED analysis for EGS14-5 (top) and 9 (bottom). Legends are the same as in Fig. 6. The panels to the left are the results from the fit to the SK07 models, while the panels to the right are the results from the fit to the powerlaw + graybody models.

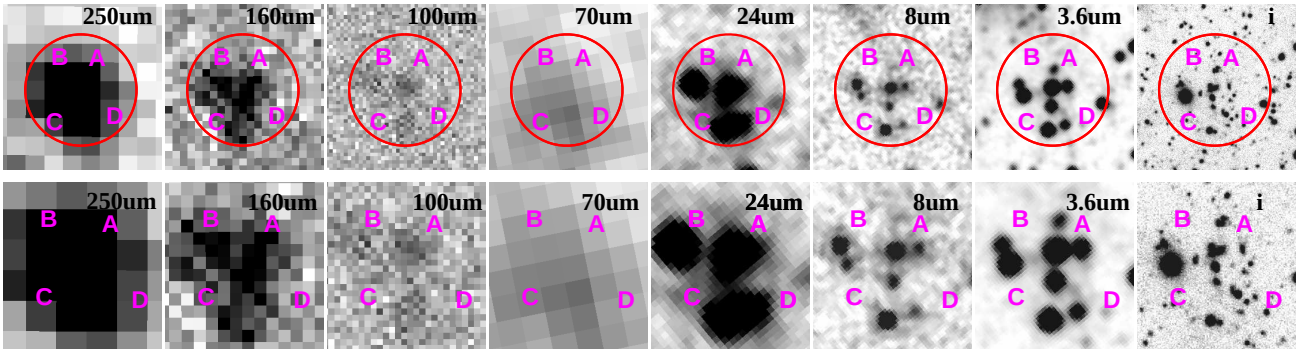

FIG. 30.— FIR to optical images of EGS19. The legends and the organization of the panels are the same as in Fig. 2. The i-band image is from CFHTLS-Deep.

composition converged at all four positions, albeit with significant residuals, which indicate that the other components that we ignored are non-negligible in this band. The decomposition failed in 70 μm due to the low S/N of the data, therefore we had to ignore this band. The automatic decomposition failed in 100 and 160 μm, presumably due to the insufficient S/N in these bands. The trail-and-error fit at 100 μm resulted in A′ and C′ as the contributors, however in 160 μm it could only settle on A′ and D. In both cases notable residuals and/or over subtractions could be seen at the positions of the other objects that did not get fitted. Forcing the fit with other combinations of objects either resulted in worse residuals or crashed the program. Nevertheless, the results for A′ were repeatable, and therefore we believed that the decomposition was successful for A′ in these two bands. In 250 μm, the automatically iterative decomposition was successful for all the four "objects", which is show in Fig.

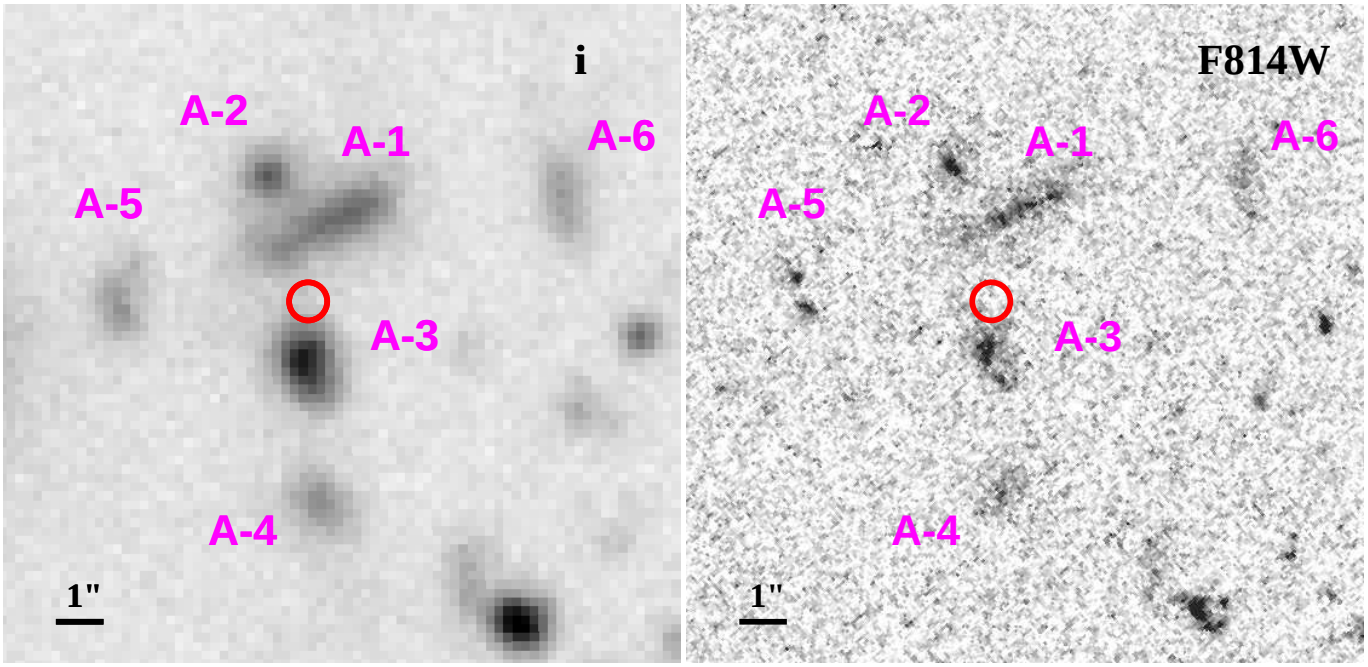

FIG. 31.— Morphological details of EGS-19, $\mathbb{A}$ component in the CFHTLS-Deep i-band (left) and the AEGIS I_{814}-band (right). The red circle is $0.4''$ in radius and indicates the position of $\mathtt{A}'$, which is the geometric center of $\mathbb{A}-1$, 2 and 4 (see §6.3.2).

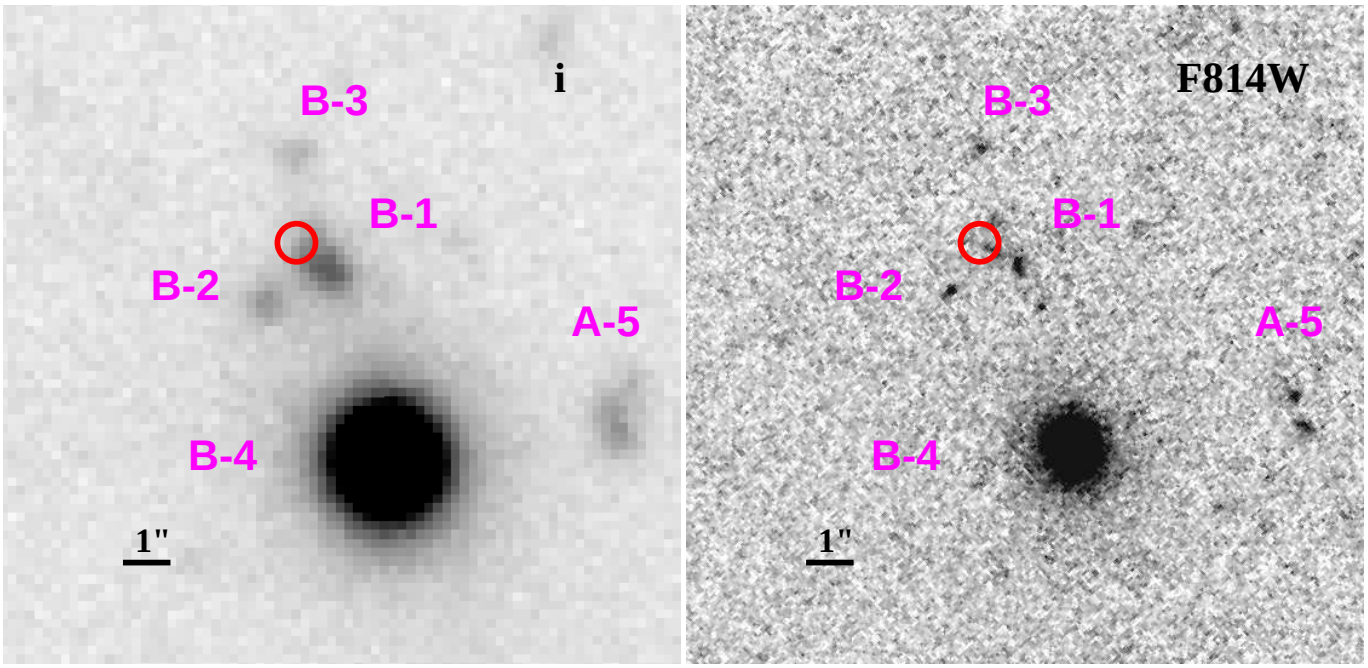

FIG. 32.— Similar to Fig. 31, but for the $\mathbb{B}$ component of EGS19. The red circle indicates the position of $\mathtt{B}'$, which is the geometric center of $\mathbb{B}-1$, 2 and 3 (see §6.3.2).

36. $\mathtt{A}'$ takes $\sim 51\%$ of the total flux and hence is the major contributor. Therefore our further discussion will only include $\mathtt{A}'$. Table 2 summarizes the flux densities of this major component.

6.3.4. *Total IR Emission and Stellar Populations*

The only X-ray source within the EGS19 area is right on $\mathbb{C}-1$ (positional offset of only $0\farcs3$). It has full-band 0.5–10 keV flux of $1.46^{+0.24}_{-0.22}\times10^{-16}erg/s/cm^2$, which corresponds to a total X-ray luminosity in restframe 1.1–21.8 keV of $1.16\times10^{43}erg/s$, implying that $\mathbb{C}-1$ most likely has an AGN. The lack of X-ray detections at $\mathtt{A}'$ suggests that the FIR emission of this object is most likely of stellar origin, as the sensitivity limit would imply an upper limit of 1.8×10^{41} erg/s in restframe 1–4 keV at $z=1.06$.

Fig. 37 summarizes the analysis of the mid-to-far-IR SED of $\mathtt{A}'$. The SK07 models provided a good fit, reassuring that our decomposition results for $\mathtt{A}'$ is reasonable. We obtained $L_{IR}=1.0\times10^{12}M_\odot$, which means that $\mathtt{A}'$ is an ULIRG. The analytic fit resulted

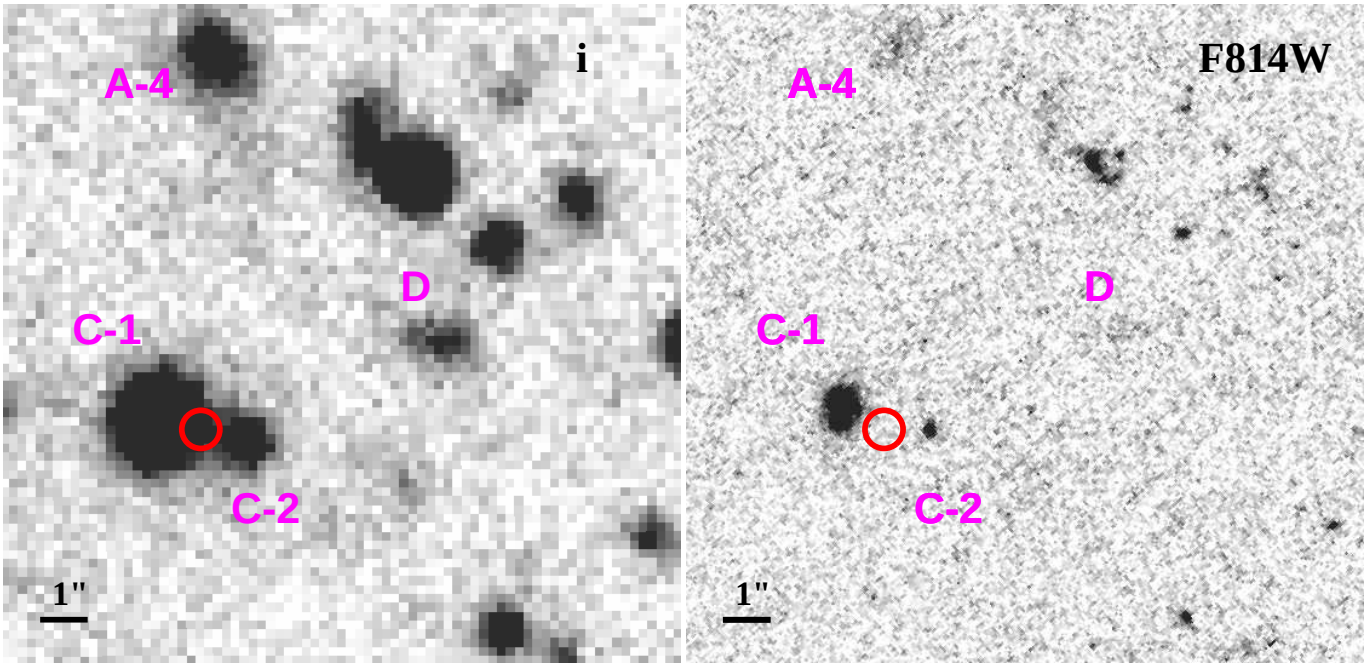

FIG. 33.— Similar to Fig. 31, but for the $\mathbb{C}$ and $\mathbb{D}$ components of EGS19. The red circle indicates the position of $\mathtt{C}'$, which is the geometric center of $\mathbb{C}-1$ and 2 (see §6.3.2).

in $T_d^{fit} = 34.0$ K and $M_d = 4.0 \times 10^8 M_\odot$. This implies $M_{gas} = 5.6 \times 10^{10} M_\odot$.

The dominant members of $\mathtt{A}'$ are $\mathbb{A}-1$ and $\mathbb{A}-4$, which have extremely similar stellar populations. They both have moderate stellar masses (4.1 and $2.9\times10^{10} M_\odot$, respectively), old ages (2.0 and 1.7 Gyr, respectively), and moderately prolonged SFH ($\tau = 0.7$ and 0.4 Gyr, respectively). Combining $\mathbb{A}-1$ and $\mathbb{A}-4$, we got $L_{IR}^{ext} = 8.1\times10^{10} L_\odot$, $L_{IR}^{blk} = 9.2\times10^{11} L_\odot$, and $SFR_{IR}^{blk} = 92\ M_\odot/yr$. Their combined $SFR_{fit} = 8\ M_\odot/yr$, and thus $SFR_{tot} = 100\ M_\odot/yr$. Using their stellar masses, we can get $SSFR = 1.4$ Gyr^{-1}, $T_{db}^{tot} = 700$ Myr and $T_{db}^{blk} = 760$ Myr. The total amount of gas inferred above could fuel this ULIRG for the next 560 Myr or its dust-blocked region for the next 608 Myr to add a further $\sim 80\%$ of its existing stellar masses.

There are two radio sources in this region (Ivison et al. 2010). One of them coincides with $\mathbb{A}-1$, and has $S_{1.4GHz} = 0.107 \pm 0.012$ mJy. The other one is on top of $\mathbb{B}-1$, and has $S_{1.4GHz} = 0.119 \pm 0.012$ mJy. Here we only discuss the FIR-radio relation for the former. We obtained $q_{IR} = 2.27$, which is lower but still consistent with the mean of 2.40 ± 0.24 in Ivison et al. (2010).

7. DISCUSSION

Strictly speaking, our sample of SDSS-invisible, bright *Herschel* sources is not flux-limited and could suffer from various types of incompleteness. Nonetheless, our study can serve as a guide to future investigations of similar objects at larger, more complete scales.

7.1. *Decomposition of Bright Herschel Sources*

Our decomposition approach provides a promising solution to maximize the returns of the large volume of precious *Herschel* data. Our technique is based on the position priors from optical or near-IR images, and this is different from those using the position priors from the MIPS 24 μm images, which suffer from the blending problem themselves. While it probably cannot decompose *all* the contributors to a given *Herschel* source, our method is capable of at least identifying its major components and extracting their fluxes. This method should work even when only using medium-deep optical images for position priors. For example, in the case of UDS01, our results would largely remain the same should we use the priors from the CFHTLS-Wide data instead of the CANDELS WFC3 IR data, because the input list would essentially be the same.

Two interesting conclusions can be drawn from our decomposition. First, as GOODSN63 shows, the brightest 24 μm source in the *Herschel* beam could have no contribution in the FIR, and therefore the use of 24 μm data should be exercised with caution and not to limit to only the brightest 24 μm sources for position priors. Second, a bright *Herschel* source usually is the collective result of multiple contributors. While the seven sources investigated here all have $S_{250} > 55$ mJy and hence are $\sim 9.5\times$ above the nominal confusion limit of 5.8 mJy/beam in HerMES at the SPIRE 250 μm (Nguyen et al. 2010), it is not guaranteed that they do not suffer from the blending problem. In fact, only two (GOODS63 and UDS04) out these seven sources can be safely treated as having only one contributor. In two other cases (UDS01 and EGS14) the source is made of two major, distinct components that are likely at the same redshifts and associated. In the other three cases (GOODSN06, EGS07 and EGS19), while there is always a primary component contributing most of the FIR flux, the other contributors, which are not physically associated with the primary component, are still non-negligible.

Both conclusions above actually echo the results of earlier studies of SMGs using the SMA (Younger et al. 2009; Wang et al. 2011; Barger et al. 2012) and the more recent ones using the ALMA (Hodge et al. 2013; Karim

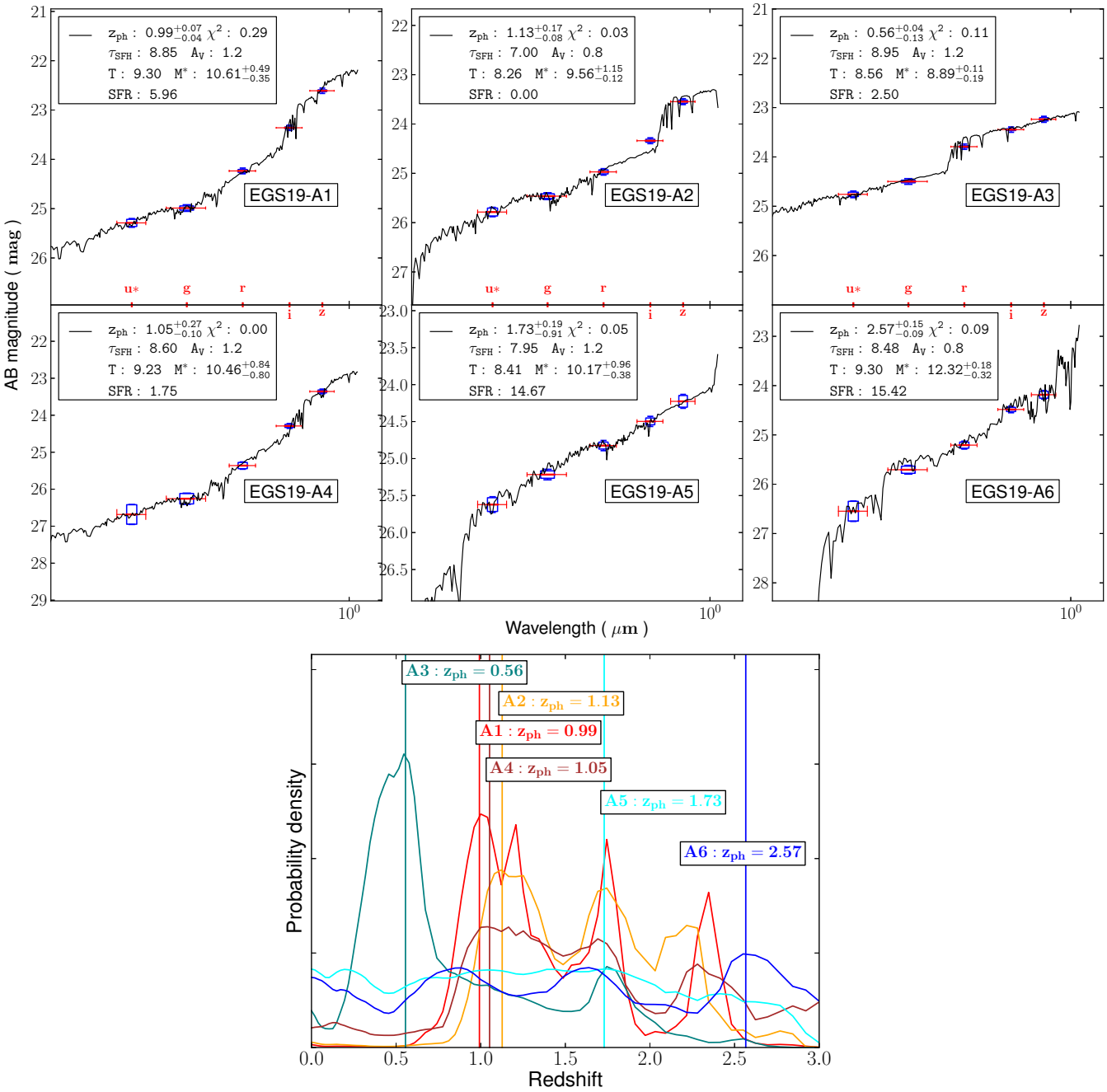

FIG. 34.— Optical SED fitting for the subcomponents of EGS19-𝔸 clump. Legends are the same as in Fig. 4. 𝔸 − 1, 2 and 4 could be at the same redshift of $z_{ph} = 1.06$ and associated.

et al. 2013). Our second point, namely, that in most cases bright *Herschel* sources are made of distinct components, will impact the interpretation of the FIR source counts and the construction of the FIR luminosity functions, especially at the bright end. This is now expected from the theoretical side. Niemi et al. (2012) suggest that source blending could be an important cause of the inconsistency between their semi-analytic model predictions and the actual observations of the bright *Herschel* source number counts. Recently, using cosmological numerical simulation, Hayward et al. (2013) predict that spatially and physically unassociated galaxies contribute significantly to the SMG population. Therefore, bright *Herschel* sources and their multiplicities warrant further investigations. As compared to addressing this problem through using sub-mm interferometry with the SMA or the ALMA, our approach offers a much less expensive alternative, albeit at the price that we are only able to reliably extract the major component(s) of a given *Herschel* source. However, as neither the SMA nor the ALMA is a survey machine, our method has its value in that in principle it can deal with a large number of sources. In addition, it is applicable in the *Herschel* fields where there are no MIPS 24 μm data as "ladders" but medium-deep optical imaging data are available or can be acquired. While in this work we still used the 24 μm image to narrow down the input list for the fit, it is possible to get rid of this intermediate step once we automate the

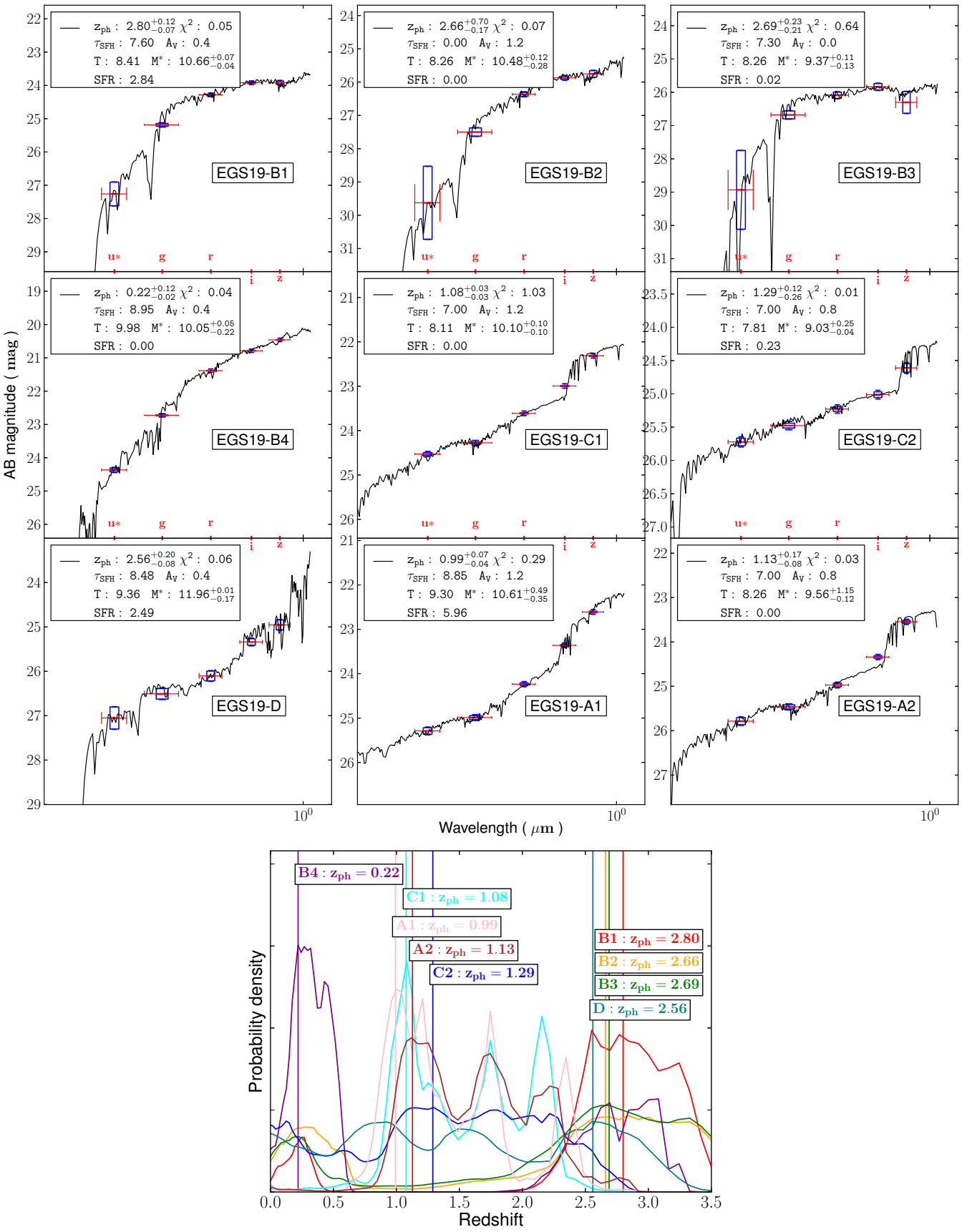

FIG. 35.— Similar to Fig. 34, but for the EGS19-$\mathbb{B}$, $\mathbb{C}$ and $\mathbb{D}$ clumps. Legends are the same as in Fig. 4. Based on their $P(z)$ distribution, $\mathbb{B}-1$, 2 and 3 could be at the same redshift of $z_{ph} = 2.72$. Similarly, $\mathbb{C}-1$ and 2 could also be at the same redshift of $z_{ph} = 1.08$, and might even be within the same $\mathbb{A}$ group. $\mathbb{D}$ could be within the same $\mathbb{B}$ group.

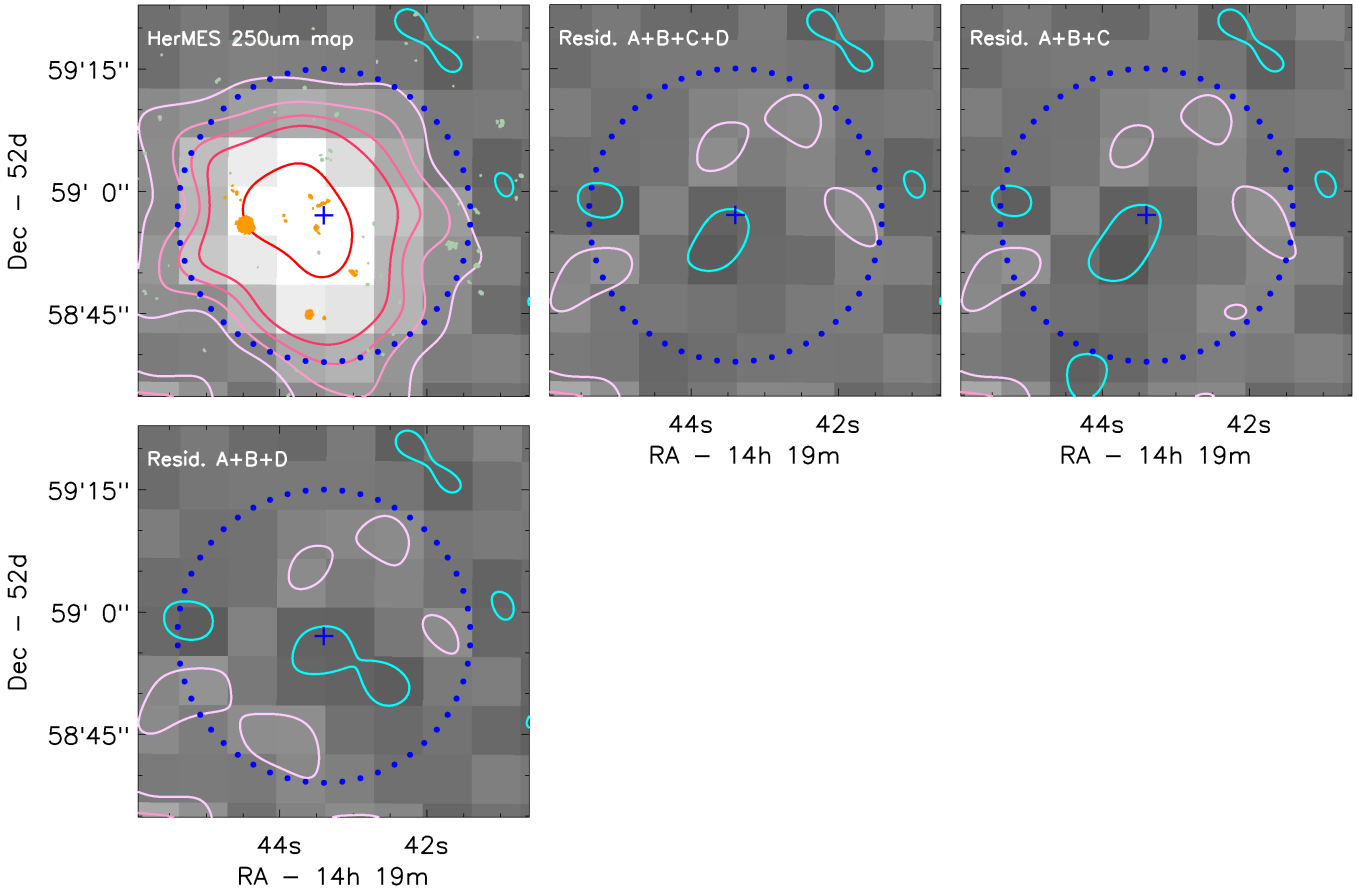

FIG. 36.— Demonstration of the decomposition of EGS19 in 250 μm. The first panel shows the original 250 μm image, while the others show the residual maps of the different decomposition schemes where different input sources are considered (labeled on top). Legends are the same as in Fig. 5. While the automatically iterative fit converges on A′+B′+C′+D, there are degenerate cases. However, A′ is always the dominant contributor and its extracted flux is essentially the same in all these cases.

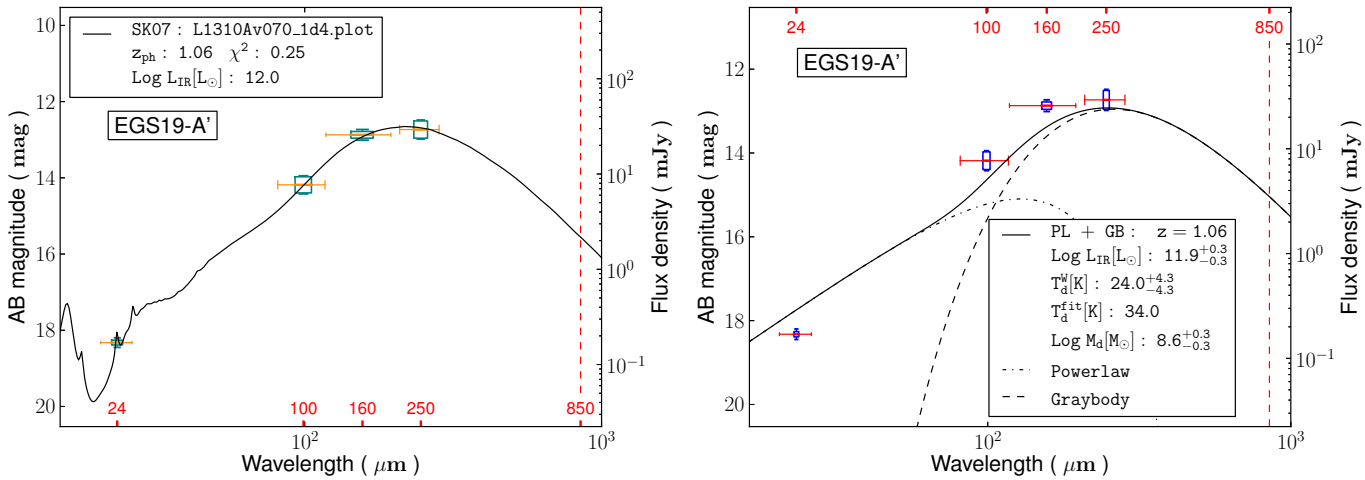

FIG. 37.— Mid-to-FIR SED analysis for EGS19-A′ at z_{ph} = 1.06. The left panel shows the fit to the SK07 models, and the right panel the fit using the power-law + graybody models. Legends are the same as in Fig. 6.

current trial-and-error approach (Ma, Stefanon & Yan, in prep.). The APPENDIX further demonstrates this point. Of course, relying on optical images for priors does have its disadvantage in that a major contributor to the FIR source, if extremely dusty, could still be missing from a medium-deep optical survey. In this case, the residual image after the decomposition will be able to reveal such a source. In fact, in our trial-and-error approach for a number of sources, the iteration was driven by the residual left at the locations of the suspected contributors.

7.2. *ULIRG Diagnostics*

Our decomposition directly identified the optical-to-near-IR counterparts of the major components of the FIR sources. This allows us to investigate the nature of the FIR emission and the underlying stellar populations. We have found the following.

First of all, the major contributors to our FIR sources are all ULIRGs at $z > 1$. Although this is not surprising given their high FIR flux densities (suggesting high IR luminosities) and faintness in optical (suggesting being at high redshifts), our analysis provides solid evidence that this is indeed the case. While one of these sources (EGS07) could have an embedded AGN, all others are mainly powered by intense star formation heavily obscured by dust.

The exquisite morphological details in the restframe optical from the *HST* data show that these ULIRG all have complicated structures indicating either merger or local violent instability. This is generally consistent with the result of Kartaltepe et al. (2012), who find that the majority of the PACS-selected ULIRGs at $z \sim 2$ in the GOODS-South field are mergers and irregular galaxies. While a quantitative morphological modeling is beyond the scope of this work, most of the counterparts to the ULIRG in our sample are not likely to be explained by a single disc galaxy. This is in contrast to the recent study of Targett et al. (2013), who find that SMGs, being ULIRGs at $z \approx 2$, are mostly disc galaxies. This contrast probably should not yet be viewed as a contradiction for two reasons. First, our objects are mostly at $z \approx 1$. Second, based on the predicted S_{850} (see Table 3) of our objects, most of them probably are not SMGs based on the conventional SMG selection criterion ($S_{850} \gtrsim 3$–5 mJy; see also Khan et al. 2009). Nonetheless, one of our object, GOODSN63-A, is an SMG at $z_{ph} = 2.28$ and apparently cannot be a disc galaxy. Clearly, the morphologies of high-z ULIRGs merit further investigation.

The assertion that our sources are all ULIRGs is based on total IR luminosities derived from the direct measurements in the FIR bands that have been properly treated for the effect of blending. They are more reliable than the extrapolation from the mid-IR (e.g., using only the MIPS 24 μm in the pre-*Herschel* era). The multiple *Herschel* FIR bands sample the peak of dust emission, and thus are more sensitive in selecting ULIRGs than using a single sub-mm band. In fact, we find that only two ULIRGs in our sample (GOODSN63-A and EGS07-1) would satisfy the nominal SMG selection criterion of $S_{850} > 5$ mJy. The *Herschel* bands are also sensitive to a wide temperature range, and are not biased against ULIRG of high temperatures as the traditional SMG selection at 850 μm is (e.g., Chapman et al. 2010; Casey et al. 2012). Indeed, our sample includes one ULIRG whose dust temperature is higher than those of normal SMGs (GOODSN06-A with $T_d^{fit} = 48.7$ K). As shown in Fig. 38 (left panel), our small sample already shows a trend that dust temperature increases with respect to increasing IR luminosity, and this is consistent with the results in the recent literature (e.g., Symeonidis et al. 2013; Swinbank et al. 2013; Magnelli et al. 2014). A much larger sample in the future, constructed following the decomposition process described in this work, will be able to enhance this trend (particularly at the bright-end) and determine whether the wide dispersion currently seen is intrinsic or is due to the contamination to the FIR fluxes by blending.

We have also investigated the FIR-radio relation of our sources. We find that some of our sources follow the relation very well and yet some deviate from it significantly. Fig. 38 (right panel) compares the q_{IR} values from our sample, which have the mean of 2.22 ± 0.28, to the mean of 2.40 ± 0.24 of Ivison et al. (2010). It seems that our values are systematically lower than theirs, however our sample is too small for us to make any assertion. Nevertheless, we argue that using our method of decomposition will result in the most reliable measurement of S_{IR} and hence reduce the random measurement error in the dispersion, and that future studies using larger sample will be able to test the FIR-radio relation for $z > 1$ ULIRG in better details.

It is interesting to relate our ULIRGs to the so-called "main sequence of star formation" on the SFR (or SSFR) vs. stellar mass plane (e.g., Noeske et al. 2007; Elbaz et al. 2007; Daddi et al. 2007; Elbaz et al. 2011; Wuyts et al. 2011; Rodighiero et al. 2011; Leitner 2012). This is shown in Fig. 39 in terms of SFR (left) and SSFR (right). In the left panel, the solid line represents the main sequence of Elbaz et al. (2007) at $z \approx 1$ and the dashed line 4× above it follows Rodighiero et al. (2011) to indicate the boundary above which starbursts locate ($\sim 2\ \sigma$ above the main sequence). In the right panel, the solid line is from the empirical fit to the main sequence as a function of redshifts based on Leitner (2012), and is fixed at the median redshift ($z = 1.2$) of our sample. Somewhat surprisingly, some of our objects are quite close or below this boundary and would be difficult to qualify as starbursts in this convention. As it turns out, the existing stellar populations of these objects tend to have an old age ($T > 1$ Gyr). In particular, GOODSN63-A and EGS14-5, which are the closest to the main sequence in SSFR vs. M^*, have the oldest ages.

The closest analogs to our objects are SMGs selected at 850 μm, which are mostly ULIRG at $z \approx 1$–3. The stellar population studies of SMGs (Borys et al. 2005; Dye et al. 2008; Michałowski et al. 2010; Hainline et al. 2011; Michałowski et al. 2012; Targett et al. 2013) have come to the conclusion that they have very high stellar masses, with the quoted median ranging from $7 \times 10^{10} M_\odot$ to $2 \times 10^{11} M_\odot$. The recent numerical simulation of Hayward et al. (2011) shows that SMGs should have a minimum of $M^* \gtrsim 6 \times 10^{10} M_\odot$ and that typical masses should be higher. Michałowski et al. (2012) and Targett et al. (2013) have found mean values of $< M^* >= (2.8 \pm 0.5) \times 10^{11}$ and $(2.2 \pm 0.2) \times 10^{11} M_\odot$, respectively. The mean of our sample is $< M^* >=$

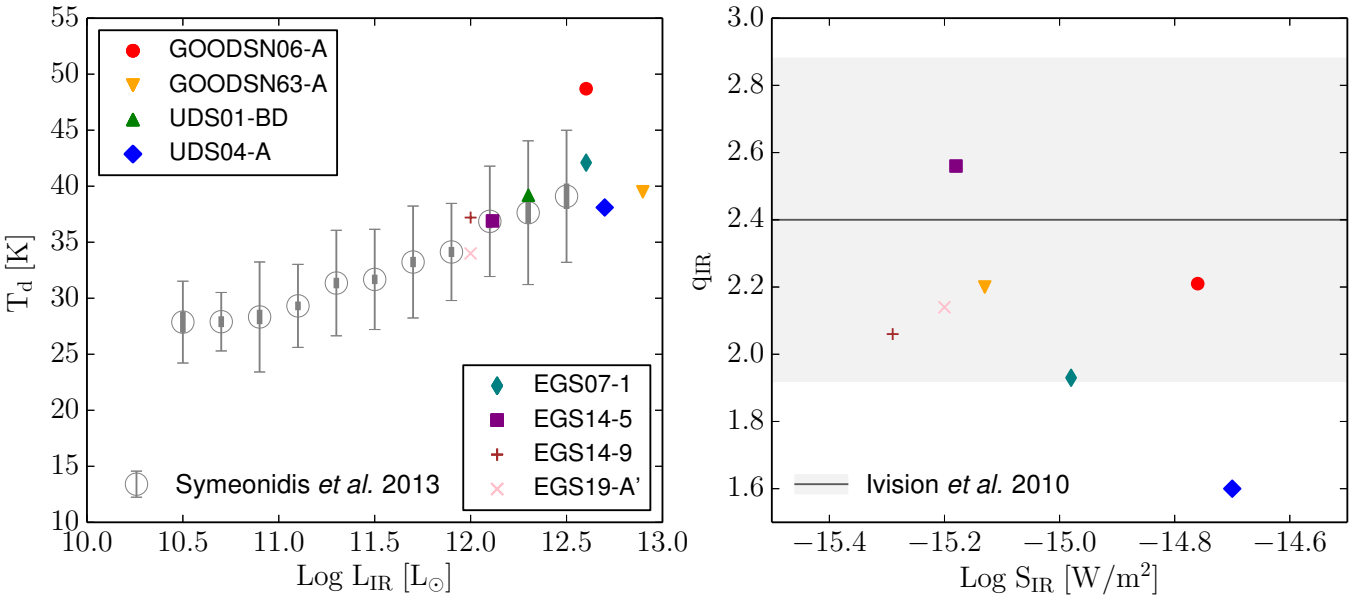

FIG. 38.— (left) Dust temperature of ULIRG as a function of total IR luminosity. The circles with error bars are the mean values from Symeonidis et al. (2013) whose sample is at $0.1 < z < 2$, while the results from our sample (as labeled) are plotted as symbols of various colors. (right) Comparison of q_{IR} from our sample, shown as the open squares, to the result of Ivison et al. (2010). The solid horizontal line indicates their mean value ($q_{IR} = 2.4$) and the gray area represents their $\pm 2\sigma_q = \pm 0.48$.

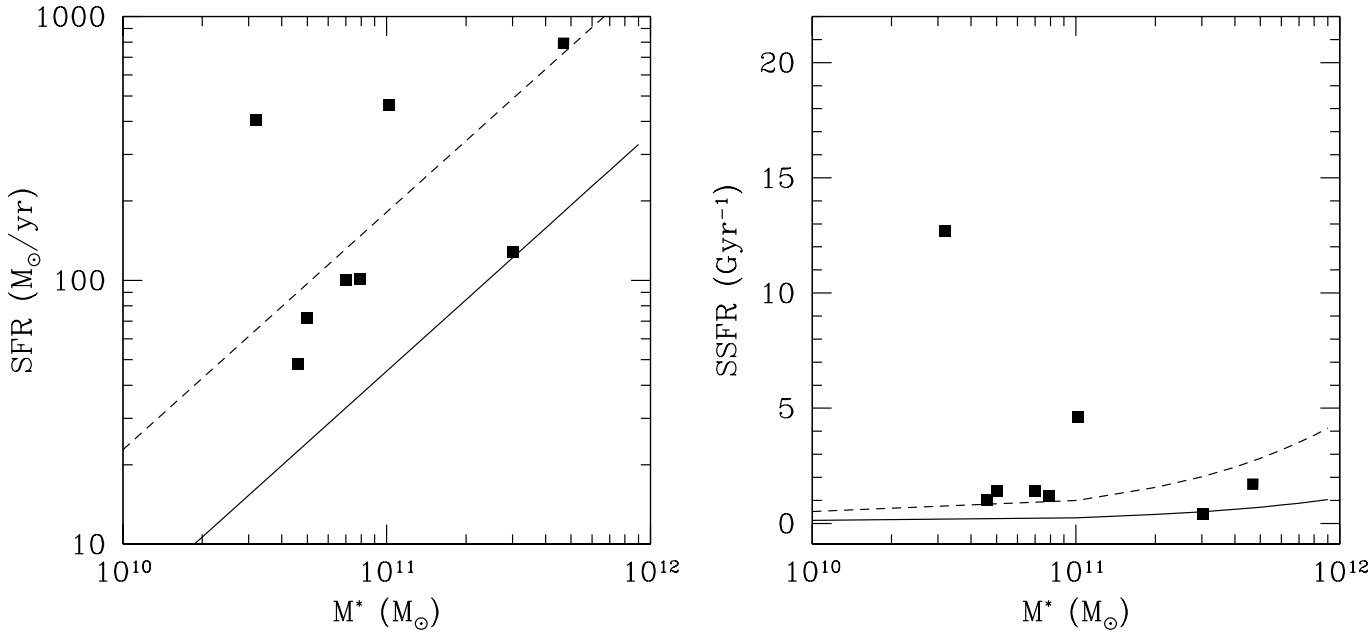

FIG. 39.— The locations of the ULIRGs in our sample with respect to the "star formation main sequence" on the SFR versus M^* (left) and the SSFR versus M^* (right) planes. The data points are based on SFR_{tot}. In the left panel, the solid line is the "main sequence" taken from Elbaz et al. (2007) and has taken into account the conversion from the Salpeter IMF to the Chabrier IMF. The dashed line follows that of Rodighiero et al. (2011) and is 4× above the main sequence. In the right panel, the solid curve is the main sequence power-law fit taken from Leitner (2012; using the data from Karim et al. 2011) and fixed at the median redshift ($z = 1.2$) of our sample. The dashed curve is 4× above the main sequence. The objects above the dashed line/curve can be taken as "starbursts" in this context. Some of our ULIRGs are actually quite close to the main sequence.

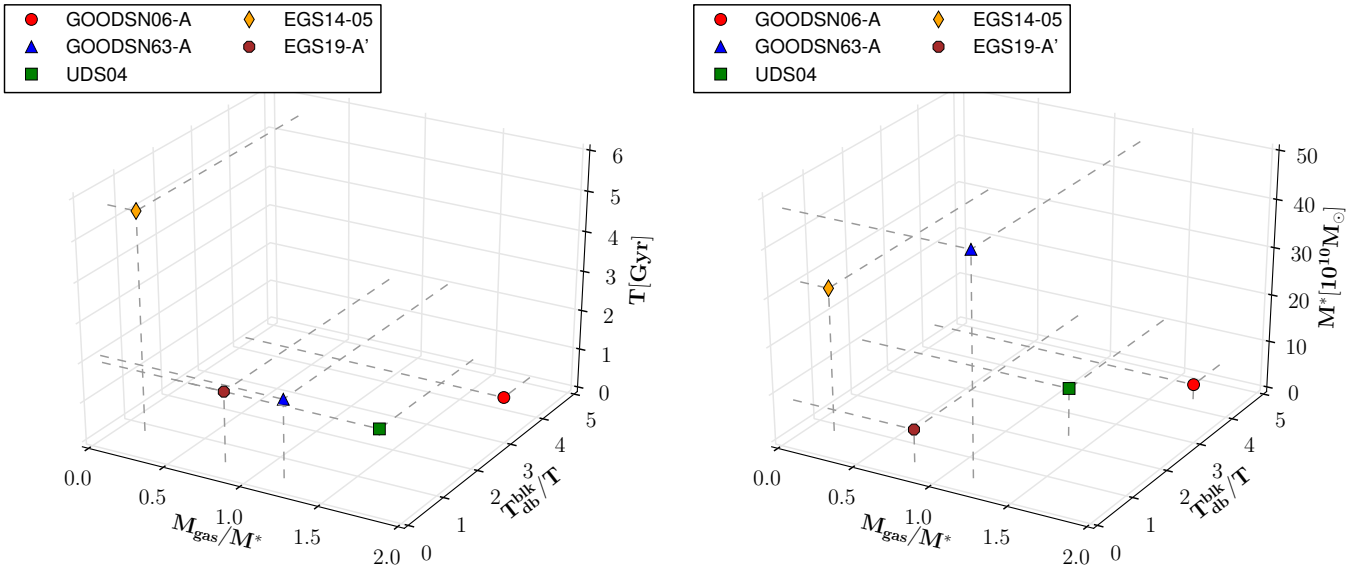

FIG. 40.— ULIRG diagnostics involving the gas mass (M_{gas}) in the ULIRG region, the stellar mass (M^*) and the age (T) of the existing stellar population in the exposed region, and the stellar mass doubling time T_{db} due to ULIRG assuming a constant SFR_{IR} into the future.

$(1.4 \pm 1.5) \times 10^{11} M_{\odot}$, where the large dispersion reflects the fact that our estimates range from as low as $2.5 \times 10^{10} M_{\odot}$ to as high as $4.7 \times 10^{11} M_{\odot}$. In fact, six out of the nine objects are below $10^{11} M_{\odot}$ (see Table 2). While the differences in the assumed SFH could affect the stellar mass estimates systematically (for example, Michałowski et al. (2012) conclude that the estimates using their preferred two-component models are 2–3× higher than those using single-component models), our large dispersion cannot be attributed to this reason. We believe that this is due to the fact that most of our objects are not SMGs. In other words, ULIRGs selected by *Herschel* bands are more heterogeneous in their existing stellar populations than SMGs. This probably is understandable given that starbursting galaxies at high redshifts are found over a wide range of stellar masses (e.g., Rodighiero et al. 2011). However, a starburst (defined as being objects far away from the "main sequence") is not necessarily an ULIRG, and therefore the spread in ULIRG stellar masses should not be taken for granted. It thus will be important to further investigate this question with a much increased, properly deblended sample.

While the stellar mass obtained through SED fitting is robust, it is known that the age inferred from the same process can be more uncertain (see e.g. Wuyts et al. (2011) for a recent reference). Presenting a comprehensive examination to address the age estimate issue is beyond the scope of this paper. Nevertheless, we argue that the age estimate in our case could still be useful. Dust extinction and metallicity are the two most severe sources of uncertainty. In the SED fitting for the existing (exposed) stellar populations, we allowed A_V to vary from 0 to 4 mag, and assumed the solar metallicity. As our objects are rather dusty, there is a chance that we might still underestimate the extinction. On the other hand, these objects could have lower metallicity because they are at $z > 1$. Generally speaking, a higher extinction would tend to result in a younger age in the fit because it would make the templates redder, and a lower metallicity would tend to result in a older age because it would make the templates bluer. Therefore, the two possible biases in our treatment tend to cancel out. For this reason, we believe that the ages that we derived still provide useful hints to understanding the progenitor of these ULIRGs.

The derived ages of our objects have a wide spread, ranging from as young as ~ 20 Myr to as old as almost the age of the universe at the observed redshift, and do not have any obvious trend with respect to the existing stellar mass. This implies that the progenitor of an ULIRG could be formed at any redshift, and that the ULIRG phase can be turned on at any point during its lifetime. Furthermore, it can be turned on at any mass range within $10^{10-11} M_{\odot}$. This is in contrast to the SMG population, where the observed ULIRG phase is believed to only happen at the late stage of their stellar mass assembly and probably will not add much to the existing mass (see e.g., Michałowski et al. 2010).

In light of this, we propose new diagnostics of ULIRGs, which is shown as 3-D plots in Fig. 39 for six ULIRGs from Table 3. The ratio M_{gas}/M^* is a measure of the gas content in the ULIRG region with respect to the existing stellar mass in the exposed region. If $M_{gas}/M^* > 1$, in principle the ULIRG will be capable of doubling the mass. The ratio T_{db}/T is a measure of how quickly the ULIRG can double the mass as compared to the age of the existing stellar population [17]. The age T is a measure of how closely the current ULIRG is related to the past SFH, i.e., it can be understood as at what stage the ULIRG happens since the birth of the galaxy. Finally, M^*, together with T, indicates how mature the existing stellar population is.

It is intriguing to see how these six ULIRGs spread in the $M_{gas}/M^* - T_{db}^{blk}/T - T - M^*$ space. Two of them, namely, GOODSN06-A and UDS04-A, are the most gas rich and the most efficient in their mass assembly. As their hosts are all quite young, these ULIRGs are likely very close to, or even being an extension of the past episode of active star formation in the hosts. The next in line is GOODSN63-A, which is capable of doubling its existing mass in a period even shorter than the age of the host. Considering that it has a very high stellar mass already (the highest among all of the six), this is rather extreme. However, its current ULIRG phase should have little to do with the bulk of the assembly of the existing mass given the old age of the host. The gas reservoirs of EGS14-9 and EGS19-A′ are somewhat insufficient for them to double their existing masses, and hence their current ULIRG phase is less important in terms of stellar mass assembly. In this regard, the current ULIRG phase of EGS14-5 is the least important, as it does not have sufficient amount of gas to get close to double the existing mass. However, it is also very unusual that a very high mass, extremely old galaxy like EGS14-5 still has not yet shut off its star formation processes at $z \approx 1$.

All this suggests that the high-z ULIRGs make a diverse population. The diagnostics such as shown in Fig. 40 have the potential of revealing the role of ULIRG in assembling high-mass galaxies. For this purpose, a much larger sample will be necessary.

8. SUMMARY

We studied a sample of seven very bright *Herschel* sources ($S_{250} > 55$ mJy) from the HerMES program that are not visible in the SDSS. Such sources have a surface density of roughly $10/\mathrm{deg}^2$, and comprise a non-negligible fraction of the brightest FIR sources on the sky. In order to understand their nature, we selected these seven sources in particular because they are in the CANDELS fields where a rich set of multi-wavelength data sets are available for our study.

Due to the large beam sizes of the *Herschel* instruments, the deep optical and near-IR images in these fields readily reveal many possible counterparts within the footprints of these FIR sources. To combat this problem, we took a new approach to decompose the heavily blended, potential counterparts, using their centroids at the high-resolution near-IR or optical images as the position priors. Such an elaborated counterpart identification is superior to the simple treatment of using a mid-IR proxy such as the MIPS 24 μm image and claiming the brightest mid-IR source within the FIR beam as the counterpart. In fact, we show that in at least one case (GOODSN63) the brightest 24 μm source within

[17] Numerically, T_{db}/T is equivalent to $1/b$, where b is the "birthrate" parameter defined as $b = SFR/ < SFR >$ and $< SFR >= M^*/T$ (Scalo 1986)

the 250 μm beam actually does not contribute to the FIR emission, which agrees with the SMA interferometry. Our method is also an improvement to using the mid-IR data for position priors, as such images are often already confused in the first place. In this regard, our approach has the advantage of unambiguously identifying the counterparts and extracting their fluxes at the same time. While in this work we still use the MIPS 24 μm data to narrow down the number of input objects to the fitting procedure, it is possible to eliminate this step when we fully automate the entire process in the near future (see APPENDIX). Once implemented, the automatic routine will have a wide application in the *Herschel* fields where the 24 μm data are not available.

Our result shows that in most cases multiple objects contribute to the ostensibly single FIR source. While some of them are multiples at the same redshifts, others are superposition by chance and are physically unrelated. If left untreated, the contamination to the FIR flux due to the latter case could be as high as 40 %. In either case, the decomposition could possibly reconcile the FIR bright-end source count discrepancy between the observations and the model predictions, and will be necessary in deriving the FIR luminosity functions, particularly in the bright-end. Our approach provides a much less expensive alternative to doing sub-mm interferometry, and has the capability of dealing with a large number of objects upon full automation.

The properly extracted, multi-band FIR fluxes allow us to determine the total IR luminosities with high accuracy, and also enable us to derive other physical parameters in the dusty region, such as the dust temperature, the dust mass and the gas mass. We find that all these seven objects are ULIRG ($L_{IR} \geq 10^{12} L_{\odot}$) at $z \geq 1$. The deep *HST* images show that they all have very disturbed morphologies, indicating either merger or violent instability. Using the radio data in these fields, we investigate the FIR-radio relation, and find that it generally holds but still breaks down in a number of cases. However, a proper interpretation of the break-down will have to wait for a much larger sample.

The *Herschel* FIR bands sample the peak of dust emission over a wide range of temperatures and redshifts, and hence the selection of ULIRG at $z > 1$ using the *Herschel* bands will be more comprehensive and less prone to selection biases. Our limited sample already shows that this is indeed the case. The closest analog to our objects are SMG, which are known to be biased against high dust temperature. Our small sample includes one ULIRG that has a high dust temperature, which was barely selected by the previous SCUBA survey. The majority of our objects actually are of similar dust temperatures as normal SMG, however they all fall below the nominal SMG flux selection limit, presumably due to their lower stellar masses that the SMGs.

The detailed SED analysis of the objects in our sample shows that the host galaxies of these ULIRGs at $z \geq 1$ are heterogeneous. Within our small sample, the hosts span a wide range in their stellar masses and star formation histories. This suggests that an ULIRG phase, if happens, can occur at any stage during the evolution of high-mass galaxies. We provide a new diagnostics of high-z ULIRGs, which utilizes the stellar mass and the age of the host, the ratio of the gas mass to the existing stellar mass, and the ratio of the stellar mass doubling time to the age of the host. This can be used to reveal how efficient and effective the current ULIRG phase is producing stars, and its relation to the existing stellar population. With a much increased sample in the future, it is promising to improve such diagnostics to shed new light on the role of ULIRGs in the global stellar mass assembly.

We thank the anonymous referee for the critical reading and useful comments, which helped improve the quality of the paper. We thank M. Bolzonella for providing the latest update of the Hyperz code, C. Peng for the useful discussion of the GALFIT code, R. Siebenmorgen for explaining a number of details of the SK07 models, R. Ivison for allowing the use of the non-public radio map in the EGS field, and E. Laird and K. Nandra for the AEGIS Chandra X-ray catalog that is not yet public. We also thank M. Dickinson, H. Ferguson, J. Newman, M. Salvato for their useful comments. H.Y., M.S. and Z.M. acknowledge the support of Spitzer RSA 1445905. This work is based on observations made by Herschel, an ESA space observatory with science instruments provided by European-led Principal Investigator consortia and with important participation from NASA. Support for Program number HST-GO-12060 was provided by NASA through a grant from the Space Telescope Science Institute, which is operated by the Association of Universities for Research in Astronomy, Incorporated, under NASA contract NAS5-26555. This work is also based in part on observations made with the Spitzer Space Telescope, which is operated by the Jet Propulsion Laboratory, California Institute of Technology under a contract with NASA. Support for this work was provided by NASA through an award issued by JPL/Caltech. This work also makes use of the SDSS. Funding for the creation and distribution of the SDSS Archive has been provided by the Alfred P. Sloan Foundation, the Participating Institutions, the National Aeronautics and Space Administration, the National Science Foundation, the Department of Energy, the Japanese Monbukagakusho, and the Max Planck Society. The SDSS Web site is http://www.sdss.org. The SDSS is managed by the Astrophysical Research Consortium for the Participating Institutions. The Participating Institutions are the University of Chicago, Fermilab, the Institute for Advanced Study, the Japan Participation Group, The Johns Hopkins University, Los Alamos National Laboratory, the Max Planck Institute for Astronomy, the Max Planck Institute for Astrophysics, New Mexico State University, the University of Pittsburgh, Princeton University, the US Naval Observatory, and the University of Washington. This paper has used data obtained by the SHARDS project, funded by the Spanish MINECO grant AYA2012-31277, and based on observations made with the Gran Telescopio Canarias (GTC).

REFERENCES

Alexander, D. M., Bauer, F. E., Schneider, D. P., et al. 2003, AJ, 126, 539

Ashby, M. L. N., Willner, S. P., Fazio, G. G., et al. 2013, ApJ, 769, 80

Assef, R. J., Kochanek, C. S., Brodwin, M., et al. 2010, ApJ, 713, 970
Barger, A. J., Cowie, L. L. & Wang, W.-H. 2008, ApJ, 689, 687
Barger, A. J., Wang, W.-H., Cowie, L. L., et al. 2012, ApJ, 761, 89
Barmby, P., Huang, J.-S., Ashby, M. L. N., et al. 2008, ApJS, 177, 431
Bertin, E. & Arnouts, S 1996, A&A, 117, 393
Bolzonella, M., Miralles, J.-M. & Pelló, R. 2000, A&A, 363, 476
Borys, C., Smail, I., Blain, A. W., et al. 2005, ApJ, 635, 853
Bradshaw, E. J., Almaini, O., Hartley, W. G., et al. 2013, MNRAS, 433, 194
Bruzual, G. & Charlot, S. 2003, MNRAS, 344, 1000 (BC03)
Calzetti, D. 2001, PASP, 113, 1449
Capak, P., Carilli, C. L.; Lee, N., et al. 2008, ApJ, 681, L53
Casey, C. M.; Chapman, S. C.; Beswick, R. J., et al. 2009, MNRAS, 399, 121
Casey, C.-M. 2012, MNRAS, 425, 3094
Casey, C.-M., Berta, S., Béthermin, M., Bock, J., et al. 2012, ApJ, 761, 139
Chabrier, G. 2003, PASP, 115, 763
Chapman, S. C., Blain, A. W., Smail, I., Ivison, R. J. 2005, ApJ, 622, 772
Chapman, S. C., Ivison, R. J., Roseboom, I. G., et al. 2010, MNRAS, 409, L13
Clements, D. L., Rigby, E., Maddox, S., et al. 2010, A&A, 518, L8
Condon, J. J., Anderson, M. L., Helou, G. 1991, ApJ, 376, 95
Coppin, K. E. K., Smail, I., Alexander, D., M., et al. 2009, MNRAS, 395, 1905
Cowie, L. L., Barger, A. J., W.-H. Wang, & Williams, J. P., 2009, ApJ, 697, L122
Daddi, E., Dannerbauer, H., Stern, D., et al. 2009, ApJ, 694, 1517
Davis, M., Guhathakurta, P., Konidaris, N. P., et al. 2007, ApJ, 660, L1
Dekel, A., Sari, R. & Ceverino, D. 2009, ApJ, 703, 785
Draine, B. T., Dale, D. A., Bendo, G.,et al. 2007, ApJ, 663, 866
Dye, S., Eales, S. A., Aretxaga, I., et al. MNRAS, 386, 1107
Eales, S., Dunne, L., Clements, D., et al. 2010, PASP, 122, 499
Elbaz, D., Hwang, H. S., Magnelli, B., et al. 2010, A&A, 518, L29
Elvis, M., Wilkes, B. J., McDowell, J. C., et al. 1994, ApJS, 95, 1
Galametz, M., Madden, S. C., Galliano, F., et al. 2011, A&A, 532, 56
Georgakakis, A., Rowan-Robinson, M., Babbedge, T. S. R., Georgantopoulos, I. 2007, MNRAS, 377, 203
Giavalisco, M., Ferguson, H. C., Koekemoer, A. M., et al. ApJ, 600, L93
Griffin, M. J., Abergel, A., Abreu, A., et al. 2010, A&A, 518, L3
Grogin, N. A., Kocevski, D. D.; Faber, S. M., et al. 2011, ApJS, 197, 35
Hainline, L. J., Blain, A. W., Smail, Ian, et al. 2011, ApJ, 740, 96
Hayward, C. C., Kereš, D., Jonsson, P., et al. 2011, ApJ, 743, 159
Hayward, C. C., Behroozi, P., Somerville, R. S., et al. 2013, MNRAS, 434, 2572
Helou, G.; Soifer, B. T.; Rowan-Robinson, M. 1985, ApJ, 298, L7
Ho, P. T. P., Moran, J. M., Lo, K. Y. 2004, ApJ, 616, L1
Hodge, J. A., Karim, A.; Smail, I., et al. 2013, ApJ, 768, 91
Hughes, D. H., Serjeant, S., Dunlop, J., et al. 1998, Nautre, 394, 241
Ivison, R. J., Chapman, S. C., Faber, S. M., et al. 2007, ApJ, 660, L77
Ivison, R. J., Magnelli, B., Ibar, E., et al. 2010, A&A, 518, L31
Karim, A.; Swinbank, A. M.; Hodge, J. A., et al. 2013, MNRAS, 432, 2
Kartaltepe, J. S., Dickinson, M., Alexander, D. M., et al. 2012, ApJ, 757, 23
Kennicutt, R. C., Jr. 1998, ApJ, 498, 541
Khan, Sophia A., Chanial, Pierre F., Willner, S. P, et al. 2009, ApJ, 706, 319
Koekemoer, A. M., Faber, S. M., Ferguson, H. C. et al. 2011, ApJS, 197, 36
Laidler, V. G., Grogin, N., Clubb, K., et al. 2006, Astronomical Society of the Pacific Conference Series, ed. Gabriel, C., et al., 351, 228
Laird, E. S., Nandra, K., Georgakakis, A., et al. 2009, ApJS, 180, 102
Leitner, S. N. 2012, ApJ, 745, 149
Leroy, A. K; Bolatto, A.; Gordon, K., et al. 2011, ApJ, 737, 12
Lonsdale, Farrah & Smith 2006, Astrophysics Update 2 (Praxis Publishing Ltd, Chichester, UK)
Lutz, D., Poglitsch, A., Altieri, B., et al. 2011, A&A, 532, 90
Madau, P., Pozzetti, L., & Dickinson, M. 1998, ApJ, 498, 106
Magnelli, B., Lutz, D., Berta, S., et al. 2010, A&A, 518, L28
Magnelli, B., Lutz, D., Santini, P., et al. 2012, A&A, 539, 155
Magnelli, B., Popesso, P., Berta, S., et al. 2013, A&A, 554, 132
Magnelli, B., Lutz, D., Saintonge, A., et al. 2014, A&A, 561, 86
McLure, R. J., Pearce, H. J., Dunlop, J. S., 2013, MNRAS, 428, 1088
Michałowski, M. J., Watson, D. & Hjorth, J. 2010, ApJ, 712, 942
Michałowski, M. J., Kamble, A., Hjorth, J., et al. 2012, ApJ, 755, 85
Morrison, G. E., Owen, F. N., Dickinson, M., et al. 2010, ApJS, 188, 178
Niemi, S.-M., Somerville, R. S., Ferguson, H. C., et al. 2012, MNRAS, 421, 1539
Newman, J. A., Cooper, M. C., Davis, M., et al. 2013, ApJS, 208, 5
Nguyen, H. T., Schulz, B., Levenson, L., et al. 2010, A&A, 518, L5
Oliver, S. J., Bock, J., Altieri, B., et al. 2012, MNRAS, 424, 1614
Peng, C. Y., Ho, L. C., Impey, C. D., Rix, H.-W. 2002, AJ, 124, 266
Pilbratt, G. L., Riedinger, J. R., Passvogel, T., et al. 2010, A&A, 518, L1
Poglitsch, A., Waelkens, C., Geis, N., et al. 2010, A&A, 518, L2
Pope, A., Scott, D., Dickinson, M., et al. 2006, MNRAS, 370, 1185
Papovich, C.; Finkelstein, S. L.; Ferguson, H. C., et al. 2011, MNRAS, 412, 1123
Rawle, T. D., Rex, M., Egami, E., et al. 2012, ApJ, 756, 106
Richards, G. T.; Lacy, M.; Storrie-Lombardi, L. J., et al. 2006, ApJS, 166, 470
Riechers, D. A., Bradford, C. M., Clements, D. L., et al. 2013, Nature, 496, 329
Roseboom, I. G., Oliver, S. J., Kunz, M., et al. 2010, MNRAS, 409, 48
Scalo, J. M. 1986, FCPh, 11, 1
Schinnerer, E., Carilli, C. L., Capak, P., et al. ApJ, 2008, 689, L5
Siebenmorgen, R. & Krügel, E. 2007, A&A, 462, 445 (SK07)
Simpson, C., Martínez-Sansigre, A., Rawlings, S., et al. 2006, MNRAS, 372, 741
Smith, D. J. B., Dunne, L., Maddox, S. J., et al. 2011, MNRAS, 416
Steston, P. B. 1987, PASP, 99, 191
Sutherland, W. & Saunders, W. 1992, MNRAS, 259, 413
Swinbank, A. M., Simpson, J. M., Smail, I., et al. 2013 (submitted to MNRAS; arXiv:1310.6362)
Symeonidis, M., Vaccari, M., Berta, S., et al. 2013, MNRAS, 431, 2317
Targett, T. A., Dunlop, J. S., Cirasuolo, M., et al. 2013, MNRAS, 432, 2012
Ueda, Y., Watson, M. G., Stewart, I. M., et al. 2008, ApJS, 179, 124
Walter, F., Decarli, R., Carilli, C., et al. 2012, Nature, 486, 233
Wang, W.-H., Cowie, L. L., Barger, A. J. 2004, ApJ, 613, 655
Wang, W.-H., Cowie, L. L., van Saders, J., et al. 2007, ApJ, 670, L89
Wang, W.-H., Cowie, L. L., Barger, A. J., Williams, J. P. 2011, ApJ, 726, L18
Willner, S. P., Ashby, M. L. N.; Barmby, P., et al. 2012, ApJ, 756, 72
Wuyts, S., Förster Schreiber, N. M., Lutz, D., et al. 2011, ApJ, 738, 106
York, D. G.; Adelman, J.; Anderson, J. E., Jr., et al. 2000, AJ, 120, 1579
Younger, J. D., Fazio, G. G., Huang, J.-S., et al. 2009, ApJ, 704, 803

TABLE 1
Sample Summary

HerMES ID	Short ID	RA & DEC (J2000.0)	S_{250}	S_{350}	S_{500}
1HERMES S250 SF J123634.3+621241	GOODSN06	12:36:34.3 +62:12:41	72.1 ± 5.4	44.4 ± 3.2	17.3 ± 3.7
1HERMES S250 SF J123730.9+621259	GOODSN63	12:37:30.9 +62:12:59	55.7 ± 5.4	59.9 ± 3.1	46.3 ± 3.5
1HERMES S250 SF J021806.0-051247	UDS01	02:18:06.0 -05:12:47	55.2 ± 9.7	40.0 ± 7.6	15.3 ± 6.1
1HERMES S250 SF J021731.1-050711	UDS04	02:17:31.1 -05:07:11	67.6 ± 9.7	49.0 ± 7.7	12.2 ± 6.3
1HERMES S250 SF J141900.3+524948	EGS07	14:19:00.3 +52:49:48	81.2 ± 6.0	71.7 ± 4.9	42.9 ± 5.2
1HERMES S250 SF J142025.9+525935	EGS14	14:20:25.9 +52:59:35	57.4 ± 6.0	45.6 ± 4.9	22.3 ± 6.0
1HERMES S250 SF J141943.4+525857	EGS19	14:19:43.4 +52:58:57	57.4 ± 6.0	24.4 ± 5.4	9.2 ± 7.1

Note. — The listed flux densities in 250 (S_{250}), 350 (S_{350}) and 500 μm (S_{500}) are in mJy. These values are taken from the HerMES DR1 catalogs, which are based on the "xID" catalogs (Wang et al., in prep.). The errors include the confusion noise. "Short ID" is a nickname assigned here for simplicity.

TABLE 2
Decomposed Mid-to-Far-IR Fluxes of the Major Components

ID	RA & DEC (J2000.0)	S_{24}	S_{70}	S_{100}	S_{160}	S_{250}	S_{350}	S_{500}
GOODSN06-A	12:36:34.519 +62:12:40.99	0.473 ± 0.023	10.40 ± 0.70	32.4 ± 1.4	65.6 ± 3.6	59.0 ± 6.5	—	—
GOODSN63-A	12:37:30.767 +62:12:58.74	0.170 ± 0.009	—	5.0 ± 0.5	22.4 ± 1.1	55.7 ± 5.4	59.9 ± 3.1	46.3 ± 3.5
UDS01-B	02:18:06.114 -05:12:50.11	0.319 ± 0.020	—	—	—	32.6 ± 9.5	—	—
UDS01-D	02:18:06.159 -05:12:44.93	0.465 ± 0.020	—	—	—	22.6 ± 9.5	—	—
(UDS01-BD)	—	0.784 ± 0.025	—	—	—	55.2 ± 9.7	40.0 ± 7.6	15.3 ± 6.1
UDS04-A	02:17:31.159 -05:07:09.15	0.670 ± 0.020	—	—	—	67.7 ± 9.7	49.0 ± 7.7	12.2 ± 6.3
EGS07-1	14:19:00.202 +52:49:47.74	0.620 ± 0.015	1.96 ± 0.50	13.9 ± 1.0	36.8 ± 2.4	64.3 ± 6.5	—	—
EGS14-5	14:20:25.704 +52:59:31.75	0.273 ± 0.015	—	8.0 ± 1.3	28.2 ± 3.2	29.2 ± 6.2	—	—
EGS14-9	14:20:26.424 +52:59:39.33	0.243 ± 0.017	—	7.8 ± 1.6	14.7 ± 3.1	28.2 ± 6.1	—	—
EGS19-A-1	14:19:43.436 +52:58:58.19	0.170 ± 0.010	—	7.7 ± 1.5	25.8 ± 2.1	29.3 ± 6.1	—	—
EGS19-A-2	14:19:43.583 +52:58:59.02							
EGS19-A-4	14:19:43.470 +52:58:52.20							

Note. — The mid-to-far-IR flux densities (in mJy) of the major components of the *Herschel* sources in Table 1, based on our decomposition results. For completeness, we also include the case of UDS01-BD where the two components UDS01-B and D are added together. For EGS19, the listed fluxes are for the major component EGS19-A′, which is a "composite source" made of EGS19-A-1, A-2 and A-4. For GOODSN06, GOODSN63, UDS01, the positions reported here are based on the H_{160} images. For UDS04, EGS07, EGS14, and EGS19, the reported positions are based on the CFHTLS images.

TABLE 3
Physical Properties of Revealed ULIRGs

ID	z	L_{IR} ($10^{12} L_\odot$)	L_{IR}^{blk} ($10^{12} L_\odot$)	S_{850} (mJy)	SFR_{IR}^{blk} ($M_\odot$/yr)	T_d^{fit} (K)	M_d ($10^8 M_\odot$)	M_{gas} ($10^{10} M_\odot$)	M^* ($10^{10} M_\odot$)	SFR_{fit} ($M_\odot$/yr)	τ (Gyr)	T (Gyr)	$SSFR$ (Gyr$^-$
GOODSN06-A	**1.225**	4.0	1.7	2.9	170	48.7	4.0	5.6	3.2	236	0.02	0.045	12.7
GOODSN63-A[a]	2.28	7.9	7.8	9.8	781	39.5	39.8	55.7	46.8	11	0	2.0	1.7
UDS01-B	**1.042**	1.0	0.48	1.5	48	—	—	—	4.6	0	0	0.13	1.0
UDS01-D	**1.042**	1.0	0.62	1.5	62	—	—	—	7.9	39	1.0	1.4	1.2
(UDS01-BD)[b]	**1.042**	2.0	—	—	—	39.2	5.0	7.0	12.5	—	—	—	—
UDS04-A	**1.267**	5.0	2.5	3.7	255	38.1	10.0	14.0	10.2	208	0.08	0.18	4.6
EGS07-1[c]	**1.497**	4.0	—	5.4	—	42.1	12.6	17.6	6.9	137	7.0	0.72	—
EGS14-5	1.15	1.3	0.83	2.1	83	36.9	4.0	5.6	30.2	45	4.0	5.5	0.4
EGS14-9	1.15	1.0	0	2.1	0	37.2	3.2	4.4	5.0	72	0.04	0.1	1.4
EGS19-A′	1.06	1.0	0.92	2.1	92	34.0	4.0	5.6	7.0	8	0.55	1.8	1.4

Note. — Properties of the major contributors to the seven *Herschel* sources. Under the column for redshift (z), the values in bold-face are z_{spec}, otherwise the total IR (8 to 1000 μm in restframe) luminosity based on the best-fit SK07 model. L_{IR}^{blk} is the total IR luminosity in the completely dust-blocked region, obtaine contribution of the dust-reprocessed light in the exposed region from L_{IR}. S_{850} is the SCUBA-2 850 μm flux density predicted from the best-fit SK07 model. S the completely dust-blocked region. T_d and M_d are the dust temperature and the dust mass, respectively. The gas mass is derived as $M_{gas} = 140 \times M_d$. M^*, τ mass, the exponentially declining SFH time scale and the age of the stellar population in the exposed region, derived from the best-fit BC03 model. SFR_{fit} pertaining to the best-fit BC03 model. The total SFR of a given system can be calculated as $SFR_{tot} = SFR_{fit} + SFR_{IR}^{blk}$. The total SSFR is defined as SSF Finally, two stellar mass doubling time scales are defined as $T_{db}^{tot} = M^*/SFR_{IR}^{tot}$ and $T_{db}^{blk} = M^*/SFR_{IR}^{blk}$.

a. For the stellar population of this object, the listed age (T) and the characteristic SFH time scale (τ) are for the "red" component in its SED. See Fig. 9.

b. This is not an independent object but for the case where the two components (UDS01-B and D) are combined.

c. This object very likely has an AGN, which could be responsible for the IR emission.

APPENDIX

A. PROSPECTIVE AUTOMATION OF THE DECOMPOSITION PROCESS

The decomposition scheme that we developed in this work has the potential of being automated and being applied to large samples in the future. Specifically, the "automatic iterative" and the "trial-and-error" steps can be integrated, and in principle we do not need a mid-IR "ladder" such as an image in MIPS 24 μm. There are multiple choices of possible approaches that involve different algorithms and criteria, and it will require extensive tests on a large sample before the implement can be finalized. There will be a lot of degenerated cases, and additional information that we can obtain from optical/NIR, such as morphology and z_{ph}, can be used to further narrow the possible solutions. While the automation is beyond the scope of this paper, we show here that it is feasible. We describe one possible approach below for the decomposition in SPIRE 250 μm.

Basically, this approach is a generalization of the "trial-and-error" method. It is reasonable to assume that, generally speaking, the objects that are closer to the source centroid are more likely the real contributors. Therefore, we define a core radius from the source centroid, r_c, and start the decomposition from the objects within this radius. The most optimal choice of this radius will have to wait for extensive tests, and for the illustration purpose here we choose $r_c = 6''$. We first consider the case that there is only one real contributor to all the flux, and the decomposition routine cycles through all the objects within r_c one by one. We then consider the case where there are two contributors, and run through all the possible pairs within r_c. If the secondary contributor in a given solution only accounts for $\leq 5\%$ of the total flux, it is deemed insignificant and the solution falls back to the one-contributor case. The same process repeats for the three-contributor case. While we can add more objects and consider the four-contributor case, in reality this might not be desirable because most of the time the added object within r_c will have a separation $\lesssim 2''$ to one of the existing object in the group and hence is not going to add an unique solution. For illustration purpose, here we stop at the three-contributor case within r_c. We then add an object beyond r_c, cycling through all objects at $r > r_c$ one by one, to the one-, two- and three-contributor combinations within r_c. If a specific addition improves the fit (for example, in terms of χ^2 as reported by GALFIT), we add a new object to this combination and repeat the process. Otherwise we terminate the sequence. Finally, we examine the χ^2 values of all the combinations that have been run through. The combinations where an object has its flux error larger than the extracted flux (both as reported by GALFIT) are deemed as "overstretching" and are rejected. We then apply a threshold on χ^2 to define a pool of candidate solutions. As our goal is to extract the *major* component of a given 250 μm source, we order these candidate solutions by the major contributor in the solution. One possible way to reach the final answer is to deem the object that has the highest occurrence among all candidate solutions as the major component. In this stage, the additional information from the high resolution images can be used to help decide on the final choice. It is possible that there will still be degeneracy, and we can offer different interpretations for each should this happen.

Here we use UDS01 as an example to illustrate this approach, where no prior knowledge in 24 μm is used. Within $18''$ to the 250 μm centroid, there are 33 objects in H_{160} with $S/N \geq 5$ (see §5.1.1). Ten of them are within $r_c = 6''$, which are shown in Fig. 41 (left). For the sake of simplicity, we concentrate on the cases within r_c and do not go beyond in this illustration. The decomposition was run through the one-, two- and three-contributor cases as described above. Fig. 41 (right) also shows the histograms of the fitting χ^2 (as reported by GALFIT) for these three cases. It is immediately clear that the two- and three-contributor cases produced better solutions than the one-contributor case, which was confirmed by the visual inspection of the residual maps. The inspection also showed that the residual maps with $\chi^2 > 1.75$ were all significantly worse than those that have smaller χ^2 values, and therefore we deemed that the best solutions were those with $\chi^2 \leq 1.75$.

The fitting χ^2 alone would suggest that the 3-component case produced many more better solutions than the 2-component case does. In particular, there is a high peak at $\chi^2 = 1.72$ in the 3-contributor case. However, further examination showed that only two of them were unique solutions and the rest were all "overstretching". Therefore, the best solutions to choose from were the nine 2-contributor solutions plus the two surviving 3-contributor solutions, all with $\chi^2 \leq 1.75$. Fig. 42 shows their residual maps in two panels in order of their fitting χ^2. The ID (three digit numbers) of the fitted objects are labeled in descending order of their extracted fluxes. To compare to the results in §5.1 where the potential contributors were pre-selected using the MIPS 24 μm information, we list the correspondence of the relevant ID's here and those in §5.1 as follows: `163 = A`, `166 = B`, `155 = C`, `149 = D`, `151 = E`, `159 = F`, and `145 = G`. The label on top of each panel in Fig. 42 reflects the correspondence. Two conclusions are immediately clear. First, these automated solutions have captured the 24 μm pre-selected candidates, and only two objects, `157` and `161`, are not among the 24 μm pre-selected ones. Second, nine out of the eleven solutions involve `B` (`166`; labeled on top in either red or blue in Fig. 42), and seven of these nine have it as the major contributor (labeled on top in red in Fig. 42). Therefore, our method chose `B` (`166`) as the major component of UDS01. The relevant solutions showed that on average `B` (`166`) accounted for $61 \pm 6\%$ of the total flux, agreeing with the value quoted in Table 2 to 2%.

While more difficult, extracting the secondary component is still possible if its contribution is significant. For the case of UDS01, $\sim 40\%$ of the total flux should be accounted for by other objects beyond the major component `B` (`166`). To be self-consistent, the secondary contributor should be sought among the solutions that result in the primary contributor, i.e., the seven solutions shown in Fig. 42 with red labels on top. As discussed in §5.1.2, `C/E` (`155/151`) and `D/G` (`149/145`) should be treated as single objects. Therefore, these seven solutions reduce to five, namely, `B+C/E`, `B+157`, `B+D/G`, `B+161`, and `B+157+G`. Note that `B+C/E` and `B+D/G` are also the solutions when using 24 μm pre-selected candidates as discussed in §5.1.3, where we point out that the formal fitting preferred `C/E` but we chose `D/G` as the final secondary component because of its stronger 24 μm flux. Our inspection of UDS01 in 250 μm (see Fig. 12) indeed

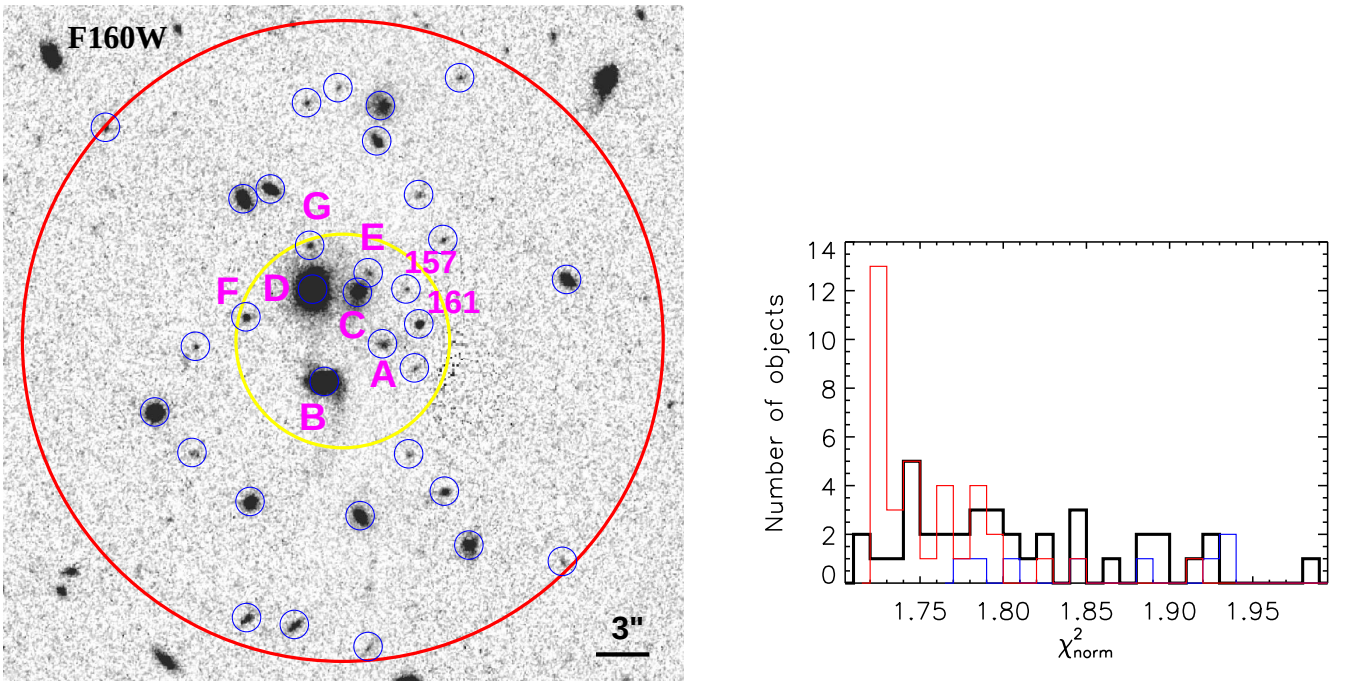

FIG. 41.— (left) Zoomed-in view of UDS01 in H_{160}. The red and yellow circles center on the 250 μm centroid and are 18″ and 6″ in radius, respectively. The latter indicates the "core region". The objects detected in H_{160} (with $S/N > 5$) are marked by blue circles. The candidate contributors found by the automatic decomposition routine are labeled in magenta, among which those the same as in §5.1.1 are labeled the same alphabetically as in Fig. 12 and the two additional ones are labeled by numbers. (right) Histograms of the fitting χ^2 by the automatic routine as described in the text. The one-, two- and three-contributor cases are coded in blue, black and red, respectively.

showed that the light distribution coincides with `C/E` better than `D/G`, and in fact this is the reason why objects `157` and `161` were among the solutions because they are closer to side of `C/E` than to that of `D/G` (see Fig. 41). We could not reject `157` or `161` being the secondary based on the decomposition solutions alone, and a proper treatment would need to taking into account other information from optical/NIR images, such as their z_{ph}. This will be deferred to our future paper on the automation. On the other hand, `C/E` and `D/G` present an interesting case of degeneracy (given that their z_{ph} are almost the same), and we could provide different interpretation for each possibility.

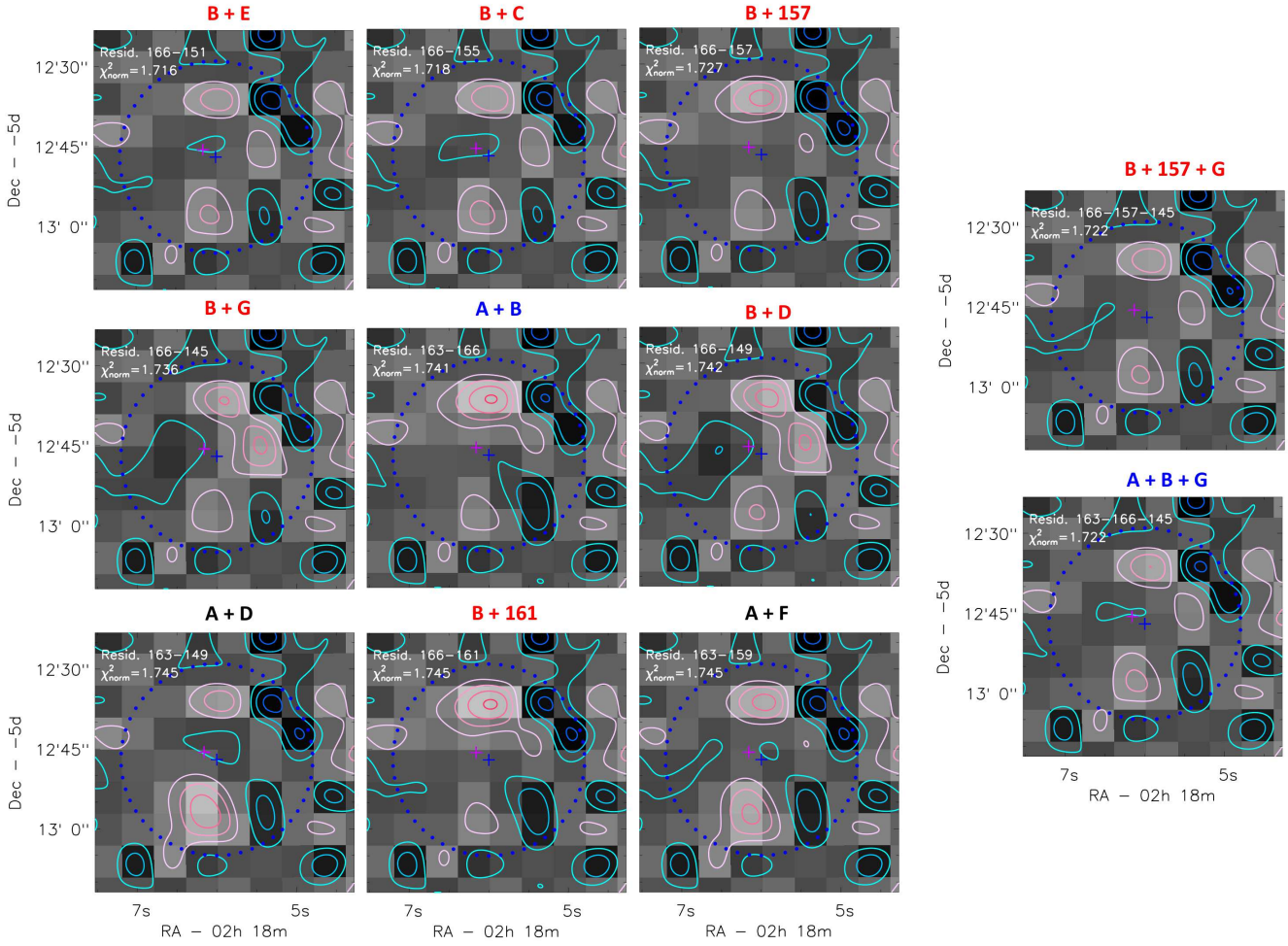

FIG. 42.— Residual maps of the automatic solutions among which the best solutions are to be decided. Each panel is for one solution as described in the text. The ID's of the objects involved in each solution are labeled, together with the fitting χ^2. The labels on top of each panel indicate the correspondence to the objects in §5.1. Other legends are the same as in Fig. 15.